AN ABSTRACT OF THE THESIS OF

Christopher S. Dandeneau for the degree of Master of Science in Materials Science presented on August 27, 2008.

Title: The Optimization of Thin Film *p*-CuO/*n*-ZnO Heterostructures for Use in Selective Gas Detection

Abstract approved: _____

Brady J. Gibbons

Since bulk *p*-CuO/*n*-ZnO heterocontacts were first proposed for gas detection, rapid development has taken place in improving the overall functionality of these structures. While bulk heterocontacts have been shown to exhibit desirable sensitivity and selectivity characteristics, these devices suffer from innate diffusion and ZnO/CuO connectivity drawbacks that limit their effective use. To address these issues, thin film *p*-CuO/*n*-ZnO heterostructures have been fabricated via wet chemical (sol-gel) processes so as to examine their potential use in reducing environments.

Individual ZnO and CuO sol-gel processes have been developed with the goal of optimizing thin film porosity, crystallinity, and preferred orientation for enhanced gas sensing capability. Particular attention was given to the effects of solution chemistry and pyrolysis temperature on desired thin film properties. For ZnO, control over film microstructure was attained through fabrication modes based on the solvents 2-methoxyethanol (MOE) and dimethylformamide (DMF). Monoethanolamine (MEA)

was employed as a chelating ligand in specific solutions. Optimum preferred orientation for DMF-based ZnO films was seen to exist at a solution chemistry of 5% water and a 1:1 molar ratio of Zn to MEA. An increase in the drying temperature yielded a monotonic decrease in the electrical resistivity of these films. For the MOE-based process, a lowering of the pyrolysis temperature led to an increase in ZnO film porosity. CuO thin films were deposited through a solution route based on isopropanol. Scanning electron microscopy (SEM) revealed the CuO films to possess a level of porosity much higher than that seen in the ZnO films.

Thin film *p*-CuO/*n*-ZnO heterostructures were fabricated in two configurations; ZnO on CuO (ZnO/CuO) and CuO on ZnO (CuO/ZnO). The results of current-voltage (*I*-*V*) tests showed the CuO/ZnO structures to display enhanced sensing characteristics to 4000 ppm hydrogen when compared to the ZnO/CuO structures. This finding was attributed to the inherently high porosity of the top CuO layer which in turn allowed for improved gas diffusion to the heterostructure interface.

The phase equilibrium between CuO and ZnO exhibits limited solubility. As such, a novel microstructure formed by combining CuO and ZnO precursors has been explored with the expectation that the films will phase separate. For the deposited films, a variance in both the annealing temperature and time was found to yield a microstructure comprised of individual ZnO and CuO grains. The co-existence of these two structures was confirmed through Energy Dispersive Spectroscopy (EDS). It is expected that the high level of connectivity between the ZnO and CuO along with negligible barriers to gas diffusion will lead to superior sensing characteristics.

The Optimization of Thin Film *p*-CuO/*n*-ZnO Heterostructures for Use in Selective Gas Detection

by

Christopher S. Dandeneau

A THESIS

submitted to

Oregon State University

in partial fulfillment of
the requirements for the
degree of

Master of Science

Presented August 27, 2008

Commencement June 2009

Master of Science thesis of Christopher S. Dandeneau presented on August 27, 2008.

APPROVED:

_____

Major Professor, representing Materials Science

_____

Director of the Materials Science Program

_____

Dean of the Graduate School

I understand that my thesis will become part of the permanent collection of Oregon State University libraries. My signature below authorizes release of my thesis to any reader upon request.

_____

Christopher S. Dandeneau, Author

ACKNOWLEDGEMENTS

To Dr. Brady Gibbons: You have been a great mentor in enabling me to reach my fullest potential. Any future success I achieve in my chosen field will be due in large part to the tools and guidance you have given me during my time here. I am honored to be you first student and can only hope that my departure will not be our last collaboration.

To Dr. David Cann: One aspect of the materials science department I always held dear was the sense of community and oneness among the graduate students. This cohesiveness was largely a result of your insistence on getting all of us to interact socially. Thanks for the BBQs, bowling nights, and scholarly advice.

To Dr. Bill Warnes: Being both a TA and student in your classes, I had the fortunate pleasure of watching a master at his profession. Your unique ability to convey material in the simplest of terms (and do it with humor) has shown me the type of lecturer I hope to one day be.

To Dr. Mike Lerner: Thank you for having the patience to explain the complexities of sol-gel to someone with no chemistry background. I hope to one day possess your ability to explain difficult concepts with proficiency and ease.

To Eric Patterson: Our friendship made for a much easier transition into this department. The fact that you put up with me as a roommate, officemate, and drinking mate speaks volumes about your patience and stamina. Thank you for introducing me to Battlestar Gallactica, Heroes, MST3K, and Arrested Development. You will make a fine professor someday.

To Yu Hong: Although we had our differences, I have always respected you as a scientist and colleague. I will never forget our cooking sessions and hours of late night studying. Best of luck in all your future endeavors.

To Sunny, Piyachon, and Anurak: Someday, I hope to enjoy Thailand in the pleasure of your company. Your kindness and generosity will be sorely missed. I will remember Thai New Year at Wat Buddha Oregon, snooker, and incredible dinners.

To Sergio Arias: You have been my closest friend during my stay here. Your good nature and zest for living has made me realize that the most important aspects of life are the bonds you forge over time. I will never forget Euro 2008, wine tastings, movie nights with the crew, Misery, and Manos, the Hands of Fate.

To my parents: Thank you for your unconditional love and support. Dad, you are my supreme role model and the embodiment of integrity, courage, and honor. If I am lucky, I will someday be half the extraordinary person you have become. Mom, thanks for your undying kindness and caring. You are the anchor that has kept our family from drifting apart.

TABLE OF CONTENTS

Page

LIST OF FIGURES

Chapter 1. Introduction and Project Objectives

1.1. Introduction

The electrical properties of certain metal oxide semiconductors change in the presence of a reducing gas. It is this phenomenon that has spurred the use of these materials in the detection of a gaseous ambient. The theoretical basis for semiconductor gas sensors arose in 1950, when Carl Wagner proposed a concept to explain the decomposition of nitrous oxide (N_2O) on zinc oxide (ZnO) [1]. He made the novel assumption that an exchange of electrons was taking place between the gaseous N_2O and the solid ZnO, which possessed a layer of adsorbed oxygen. A few years later, Brattain *et al*. found that ambient gas produced changes in potential between an electrode and a germanium surface [2]. These findings were explained in a theory outlining the existence of donor and acceptor traps that lead to the generation of a space charge layer on the surface of the germanium. A working gas sensor was realized in 1962, when Seiyama *et al*. detailed the use of ZnO thin films in the detection of such gases as ethanol (C_2H_6O) and carbon dioxide (CO_2) [3]. It was in this same year that Naoyoshi Taguchi was issued a patent for a gas sensor based on tin oxide (SnO_2) [4]. As such, gas sensors based on SnO_2 are typically referred to as Taguchi sensors and are commercially available through Figaro Engineering Inc. [5].

Two of the most widely studied gas sensor materials are ZnO and copper oxide (CuO). ZnO is an intrinsic *n*-type semiconductor possessing both a wide band gap (~3.3 eV) [6] and a large exciton binding energy (60 meV) [7]. The scenario of

electrons as the majority charge carriers in ZnO arises from an inherent oxygen deficiency traced to either zinc interstitials or oxygen vacancies [8]. CuO, possessing an oxygen-rich stoichiometry, is a *p*-type semiconductor with a band gap of approximately 1.4 eV [9]. Previous research on CuO and ZnO powders has shown limited solubility (less than 4%) of CuO in ZnO when a 1:1 atomic ratio of Cu:Zn was used [10, 11]. The difference in majority charge carrier along with the relative immiscibility of these oxides has motivated their incorporation into novel gas sensing designs. One such device, the *p*-CuO/*n*-ZnO heterocontact, was first proposed for gas detection in 1986 by Nakamura *et al*. and employed bulk CuO and ZnO disks placed into mechanical contact [12]. This structure was shown to exhibit inherent selectivity, a reference to the ability of a sensor to detect and quantify a gas of interest (the analyte) in the presence of common interferents.

The electrical properties of a bulk CuO/ZnO heterocontact interface are highly sensitive to the presence of adsorbed gas [13-15]. For example, the governing reactions for a CuO/ZnO heterocontact in the detection of hydrogen (H_2) may be written as:

$$[n\text{-ZnO}]: O_2 + 2e^- \rightarrow 2O^- \quad (1.1)$$

$$[p\text{-CuO}]: 2H_2 + 4h^+ \rightarrow 4H^+ \quad (1.2)$$

$$[\text{interface}]: 4H^+ + 2O^- \rightarrow 2H_2O \quad (1.3)$$

The reaction between adsorbed oxygen on the *n*-ZnO (1.1) and hydrogen on the *p*-CuO (1.2) lead to the evolution of water (1.3) and a reduction in the potential barrier

to charge movement across the *pn* interface. This may be quantified through appropriate current-voltage (*I*-*V*) testing of the heterocontact.

While bulk *p*-CuO/*n*-ZnO heterocontacts have demonstrated desirable sensitivity and selectivity characteristics, these structures possess a few innate drawbacks. First, the analyte must traverse a rather circuitous diffusion path to reach the *pn* interface. This serves to reduce both sensitivity and response time. Second, the device interface is typically formed by mechanically pressing bulk CuO and ZnO disks into contact. Consequently, the contact area, or connectivity between the CuO and ZnO is low, which minimizes the effective interfacial area of the device.

1.2. Project Objectives

The work presented here serves to address the aforementioned diffusion and connectivity issues through the fabrication of thin film *p*-CuO/*n*-ZnO heterostructures. Specifically, the objectives of this project are as follows:

1) Optimize the individual CuO and ZnO fabrication processes with regards to the attainment of desirable levels of crystallinity, preferred orientation, and porosity

The existence of a high degree of long range order (crystallinity) was sought in order to maximize charge carrier mobility, and thus reduce device response time. Optimized preferred orientation was specifically sought for ZnO, as thin film CuO is not known to orient in any preferred crystallographic direction. It has been stated that

high levels of preferred orientation serve to lower ZnO resistivity due to reduction in scattering events at grain boundaries and shorter charge carrier path lengths encountered by electrons travelling in the *c*-plane [16, 17]. The ability to produce films of high porosity levels was deemed essential in ensuring fast diffusion of the analyte to the heterostructure interface.

2) Incorporate the optimized thin films into planar thin film *pn* heterostructures and monitor the electrical response in reducing environments

With the optimization of each individual CuO and ZnO fabrication process, steps were taken to incorporate them into a planar thin film heterostructure. Thin film processing via sol-gel presents a unique opportunity for increasing the degree of connectivity between the CuO and ZnO. The liquid precursors used in sol-gel fabrication allows for a uniform coating of complex geometries [18]. As such, a coherent interface with a large degree of contact area may be established between the ZnO and CuO layers. In addition, the reduced dimensions of thin film geometries serves to further increase the rate of analyte diffusion to the heterocontact interface.

3) Develop novel *p*-CuO/*n*-ZnO heterostructures that may further increase the device interfacial area and response time

As stated above, the immiscibility of ZnO and CuO allows for the creation of novel sensor designs. As such, a mixed solution method has been employed in the

fabrication of a unique CuO/ZnO heterostructure. This device is comprised of ZnO grains amidst a matrix of CuO grains. Consequently, the area of the heterostructure interface is greatly increased and diffusion paths are essentially negligible.

The initial content of this work will consist of a thorough review regarding relevant concepts and literature pertaining to semiconductor gas sensors. This will be followed by an outline of the experimental procedures used in attaining the project objectives. Subsequent sections will address each of the objectives listed above. Lastly, the conclusions evident from the experimental results will be summarized and avenues for future research endeavors will be given.

Chapter 2. Literature Review

In the following review, theories regarding the operation of a metal oxide semiconductor gas sensor will be analyzed. The discussion will begin with the topic of non-stoichiometry and how it relates to the observed *n* and *p*-type conductivity in materials used for sensor devices. This will be followed by a critical examination of theories pertaining to catalysis and adsorption. The sensor parameters of sensitivity and selectivity will also be introduced. Concepts related to *pn* junction operation and the use of *pn* heterostructures for gas detection will be outlined. Lastly, a brief overview of the sol-gel process will be given.

2.1 Non-stoichiometry

Non-stoichiometry represents a defect scenario where there is a variance in the inherent composition within a given structure [19]. It is this variance from ideality that leads to the observed *n* and *p*-type conductivity in many metal oxides. While non-stoichiometry can result from extrinsic impurities incorporated into the crystal lattice, it may also exist in "pure" compounds, as is the case with many metal oxide semiconductors. To begin the discussion on the role of non-stoichiometry, one must first look at why defects play a part in the equilibrium state of a pure crystal.

2.1.1. Thermodynamics

From a thermodynamic standpoint, equilibrium (at constant pressure) coincides with a system attaining a minimum value of Gibbs free energy, which is defined by [20]:

$$G = H - TS \tag{2.1}$$

where G is the Gibbs free energy, H is the enthalpy, T represents temperature, and S is the entropy. The entropy is comprised of both a vibrational, S_V, and a configurational, S_C,entropy term. The configurational entropy is defined by:

$$S_C = k \ln \Omega \tag{2.2}$$

where k is Boltzmann's constant and Ω is the number of possible ways the system can be arranged. From (2.2), it is clear that the more defects present in the system, the greater the Ω term and thus, a greater value of S_C is attained. However, there is an energy cost that accompanies the creation of defects. The free energy change resulting from the formation of n crystal defects is:

$$\Delta G = nh - nTS_V - kT \ln \Omega \tag{2.3}$$

where ΔG represents the change in free energy and h is the enthalpic cost, or energy of formation per defect. As seen in (2.3), a minimization of Gibbs free energy involves a delicate balance between enthalpy and entropy. An alternative expression for Gibbs free energy can be written to include the effects of pressure (P) and volume changes (ΔV) associated the introduction of a defect:

$$\Delta G = \Delta H - T\Delta S + P\Delta V \tag{2.4}$$

In (2.4), ΔH and ΔS represent the total formation enthalpy (formation energy) and formation entropy change, respectively, in forming the defect [21]. An important point to note here is that many researchers [21, 22] will neglect both ΔS and $P\Delta V$ in their calculations. Their reasoning is as follows. The ΔS term is seen mainly as the change in vibrational entropy. This change is seen to be on the same order when comparing defects and is thus disregarded. As for the $P\Delta V$ term, since it is related to the volume change associated with the introduction of a defect, it is negligible when considering a relatively dilute defect concentration and only becomes significant under high pressure. Regardless, through differentiation of (2.3) and some subsequent rearrangement, one can derive the mass action or equilibrium constant, $K(T)$:

$$K(T) = e^{\frac{S_V}{k}} e^{\frac{-h}{kT}} \tag{2.5}$$

$K(T)$ represents the concentration of a specific crystalline defect at equilibrium. Through inspection of (2.5), one can see that defects with a high energy of formation (enthalpic cost) will occur in low equilibrium concentrations.

2.1.2. Non-Stoichiometry in Semiconductors

The relevance of non-stoichiometry to the transport properties of metal oxide semiconductors will now be explored using ZnO and CuO as examples. As stated in Chapter 1, ZnO is stoichiometrically deficient in oxygen while CuO is inherently oxygen-rich. To begin, the notation of Kröger and Vink [23] must first be introduced.

A defect is characterized by the charge it carries relative to the surrounding crystal lattice [24]. A defect's superscript denotes this relative charge, with a dot ($^{\cdot}$) being a single positive charge and a prime ($'$) denoting a negative charge. Neutrals are written with either an *x* (^{X}) or no superscript. A subscript is used to denote the lattice site of the defect, with *i* ($_{i}$) being used to signify an interstitial atom. Vacancies are represented with the letter *V*, as in $V_{\mathrm{O}}^{\cdot\cdot}$, which denotes a doubly charged vacancy occupying an oxygen lattice site. Electrons and holes may be signified by e and h, respectively.

The equilibrium constant, *K*(*T*), for the general chemical reaction [19]:

$$aA + bB \rightarrow cC + dD \tag{2.6}$$

can be written as:

$$K(T) = \frac{[C]^c[D]^d}{[A]^a[B]^b} = e^{\frac{-\Delta G^\circ}{kT}} \tag{2.7}$$

where ΔG represents the standard change in free energy for the reaction. An oxygen vacancy, known as a type of Schottky defect, can be generated in ZnO through the following reaction:

$$\mathrm{Zn}_{\mathrm{Zn}} + \mathrm{O}_{\mathrm{O}} \rightarrow \mathrm{Zn}_{\mathrm{Zn}} + V_{\mathrm{O}}^{\cdot\cdot} + 2\mathrm{e}' + \frac{1}{2}\mathrm{O}_2(g) \tag{2.8}$$

It is conventional practice to denote the left side of (2.8) as "nil". As seen in (2.8), a positively charged oxygen vacancy is compensated by the generation of electrons, thus leading to *n*-type conductivity of ZnO. The mass action constant for (2.8) can be written as:

$$K_R = [V_{\mathrm{O}}^{\cdot\cdot}](p\mathrm{O}_2)^{\frac{1}{2}} n^2 \tag{2.9}$$

where pO_2 denotes the partial pressure of oxygen and $[V_O^{\cdot\cdot}]$, n represent the oxygen vacancy and electron concentrations, respectively. To solve for $[V_O^{\cdot\cdot}]$ or n, one must evoke the electroneutrality condition (ENC), which states that the concentration of positive defects present in the material must equal the concentration of negative defects. The ENC for (2.8) is:

$$2[V_O^{\cdot\cdot}] = n \tag{2.10}$$

Using (2.10) and solving for $[V_O^{\cdot\cdot}]$ or n in (2.9) yields:

$$[V_O^{\cdot\cdot}] = (\frac{K_R}{4})^{\frac{1}{3}}(pO_2)^{-\frac{1}{6}} \tag{2.11}$$

and

$$n = (2)^{\frac{1}{3}}(K_R)^{\frac{1}{3}}(pO_2)^{-\frac{1}{6}} \tag{2.12}$$

Thus, the logarithmic concentration of oxygen vacancies and electrons in ZnO, plotted against $\log(pO_2)$, is shown to have what is termed a -1/6 pO_2 dependence. The electronic conductivity, σ, is given by:

$$\sigma = q(2)^{\frac{1}{3}}(K_R)^{\frac{1}{3}}(pO_2)^{-\frac{1}{6}}\mu_e \tag{2.13}$$

where q is the electronic charge and μ_e is the electronic mobility.

An oxygen deficiency in ZnO may also be realized through the formation of a Zn interstitial, known as a type of Frenkel defect. This can be formed through the following reaction:

$$\text{nil} \rightarrow Zn_i^{\cdot\cdot} + 2e' + \frac{1}{2}O_2(g) \tag{2.14}$$

Using the ENC for this reaction and substituting it into the proper equation for the equilibrium constant will also yield a -1/6 pO_2 dependence.

In the case of CuO, an oxygen rich stoichiometry may arise from either Cu vacancies or oxygen interstitials. The generation of a Cu vacancy may occur through the following reaction:

$$\frac{1}{2}O_2 \rightarrow O_O + V_{Cu}^{''} + 2h^{\cdot} \tag{2.15}$$

The generation of holes in (2.15) leads to *p*-type conductivity in CuO. A reaction that forms oxygen interstitials can be represented by:

$$\frac{1}{2}O_2 \rightarrow O_i^{''} + 2h^{\cdot} \tag{2.16}$$

The derivation of equilibrium constants and pressure dependent conductivity may be found in a manner similar to that for ZnO.

2.2. Gas Sensor Operation: Catalysis and Adsorption

The electrical conductivity of a semiconductor is dictated in large part by the concentration of electrons or holes present in the material. In certain metal oxide semiconductors, the majority charge carrier concentration changes as a result of an interaction with a gaseous species. The resulting change in conductance may be quite large and provides the basis for semiconductor gas sensor operation. This behavior is unlike metals, where the adsorption of a gas may cause small conductance changes due to a modification of charge carrier mobility [6]. As an example, recall the

experiments of Wagner on the decomposition of N_2O on ZnO. If the generation of two electrons proceeds as in (2.8), the decomposition reaction was proposed as follows [1]:

$$2e^- + N_2O \rightarrow N_2 + O^{2-}(\text{ads.}) \tag{2.17}$$

$$O^{2-}(\text{ads.}) + N_2O \rightarrow N_2 + O_2 + 2e^- \tag{2.18}$$

The adsorption of oxygen in (2.17) would result in an increase in ZnO resistivity due to the capture of majority charge carriers. The subsequent reaction between the adsorbed oxygen and N_2O in (2.18) acts to restore the supply of conduction electrons and thus, an increase in conductivity may be observed. It is this simple and reversible change in charge concentration that drives the use of metal oxide gas sensors.

For a visual perspective, a schematic of an *n*-type semiconductor powder with an accompanying band structure model is shown in Figure 2.1 [25]. For conduction to occur, an electron must pass from one grain to the next. While there exists an ample concentration of electrons in the bulk of the material, adsorbed oxygen has captured electrons near the surface of the powder. The electrons that bind to the adsorbed oxygen leave behind positively charged donor ions. An electric field develops between these positive donor ions and the negatively charged adsorbed oxygen ions which serves to impede the flow of electrons between neighboring grains. The barrier generated by the electric field has a magnitude of eV_s, where e is the electronic charge and V_s is the potential barrier. The magnitude of V_s increases as more oxygen adsorbs on the powder surface. Utilizing the Boltzmann equation, the concentration of electrons, n_s, that possess ample energy to cross the barrier and reach a neighboring

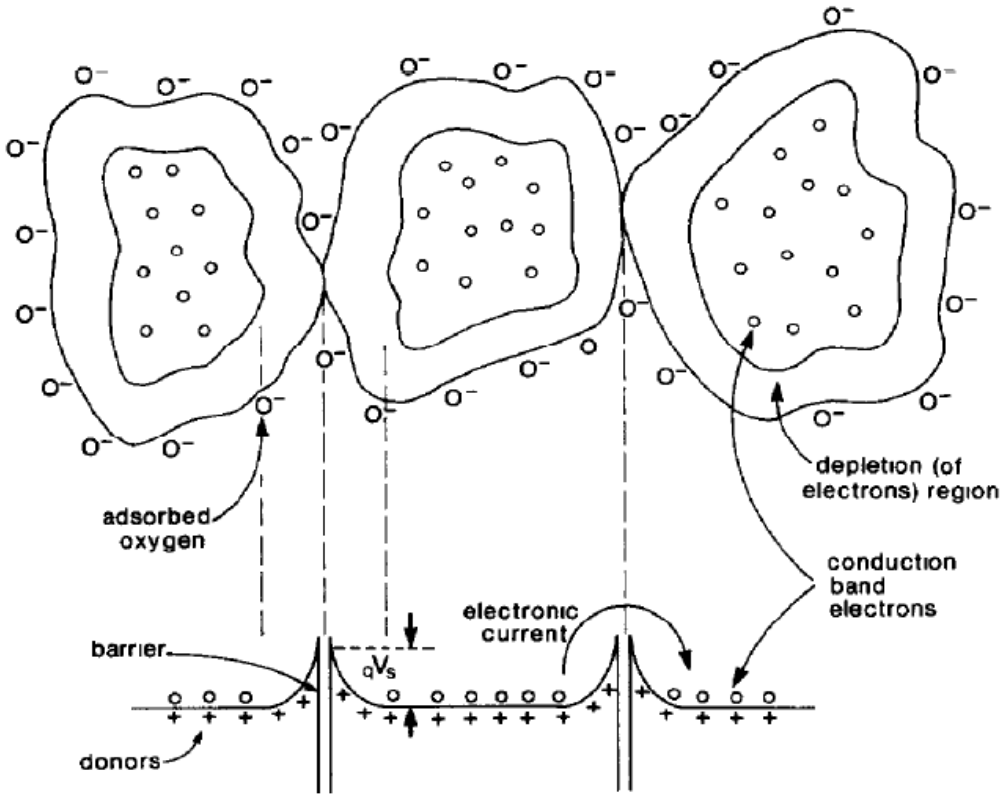

Figure 2.1. A schematic of an *n*-type semiconductor powder. Adsorbed oxygen leads to generation of a region depleted of majority charge carriers. The accompanying band structure model shows the potential barrier to charge movement across neighboring grains [25].

grain is given by [25]:

$$n_s = N_d \exp\left(-\frac{eV_s}{kT}\right) \tag{2.19}$$

where N_d is the concentration of donors, k is Boltzmann's constant, and T is the temperature. Since conductance (or resistivity) is proportional to n_s, an increase in the

adsorbed oxygen content will raise eV_s and thus, fewer electrons will cross the potential barrier. This may be empirically monitored as an increase in resistivity. The introduction of a reducing gas will reverse this effect, lowering the potential barrier and decreasing resistivity. It is this reducing gas, often termed the analyte, whose presence is of interest. Using an example of ZnO in the detection of hydrogen, the following reactions may occur:

$$2e^- + O_2 \rightarrow 2O^-(\text{ads.}) \tag{2.20}$$

$$2O^-(\text{ads.}) + 2H_2 \rightarrow 2H_2O + 2e^- \tag{2.21}$$

The reaction of H_2 with adsorbed oxygen on the surface of ZnO (2.21) will result in a measurable reduction in the resistivity. It should be noted that adsorbed oxygen may exist in multiple forms. Takata *et al*. proposed that oxygen adsorbed on ZnO is transformed with increasing temperature in the following manner [26]:

$$O_2 \rightarrow O_2^- \rightarrow 2O^- \rightarrow 2O^{2-} \tag{2.22}$$

Of these forms, O_2 is considered fairly inactive due to its non-dissociative state [25]. With regards to O_2^- and O^-, electron spin resonance (ESR) studies have shown that O^- is far more reactive than O_2^- [27]. The nature of adsorbed oxygen on ZnO as reported by several researchers is shown in Figure 2.2 [26].

A catalyst acts to increase the rate at which a chemical reaction approaches equilibrium, without permanently being altered in the process [28]. In the reactions detailed in (2.17) – (2.18) and (2.20) – (2.21), ZnO acts as a heterogeneous catalyst, as it is a phase distinct from the reactants and products. To illustrate the phenomenon of

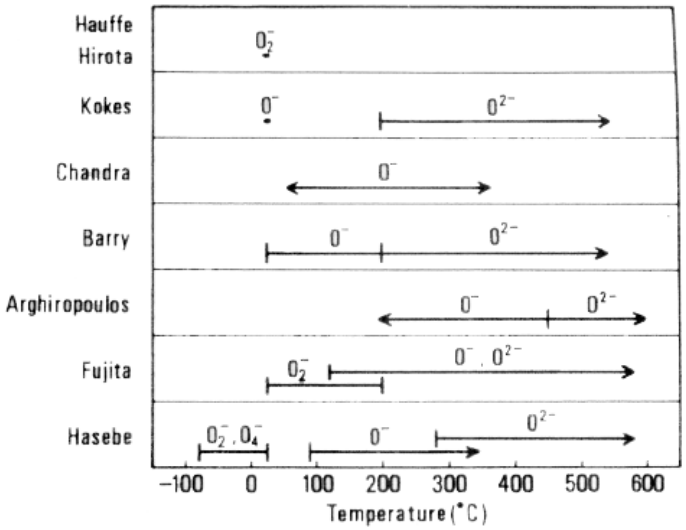

Figure 2.2. The nature of oxygen species adsorbed on ZnO as reported by several researchers [26].

catalysis, consider the following reaction:

$$A + B \rightarrow C + D \tag{2.23}$$

Two possible paths in which this reaction may proceed are shown in Figure 2.3 [28]. In the absence of a catalyst, the reaction of (2.23) is characterized by a large activation energy, E_g. When a catalyst such as ZnO or SnO_2 is used, the gaseous products adsorb onto the metal oxide surface with an exothermic heat of adsorption ΔH (State I). The reaction to form adsorbed products then proceeds with a lower activation energy E_c (State II). It is evident from Figure 2.3 that if ΔH is too large, the gaseous reactants are strongly adsorbed and E_c may become too large for the reaction to proceed. An undesirably low activation energy will cause the reaction to be energetically easier, but will result in fewer products available for the reaction.

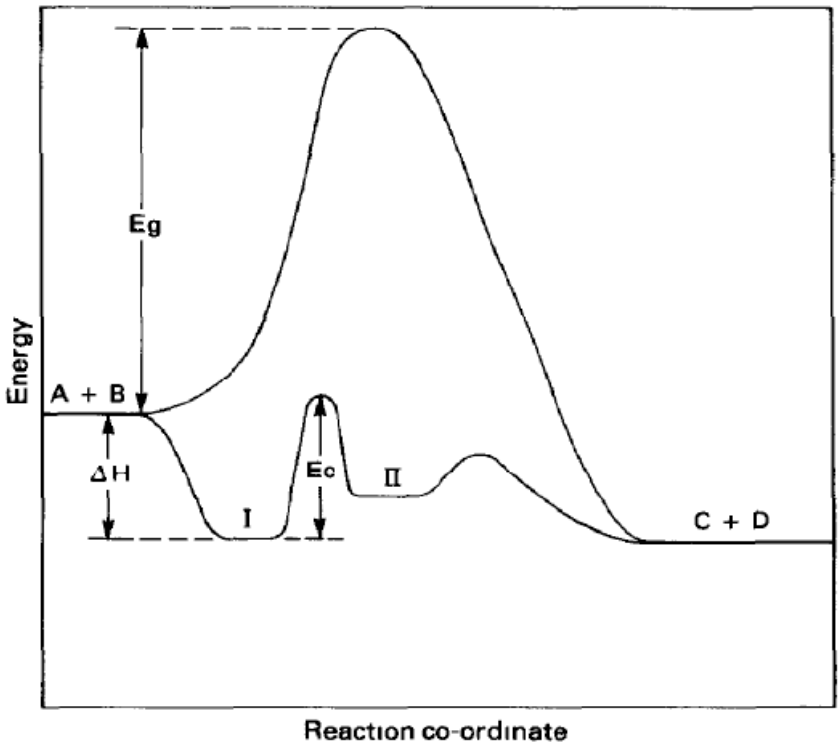

Figure 2.3. The energy barriers in the transformation from reactants (A + B) to products (C + D). The uncatalyzed reaction is characterized by a large activation energy (E_g), while the barrier to product formation is lowered (E_c) when a catalyst is used [28].

A gas molecule approaching the surface of a solid will be subject to an attractive potential [29]. This potential is the origin of adsorption and arises from the multitude of unsatisfied bonds that exist at the surface of the solid. The adsorbed species is often called the adsorbent and the solid surface is termed the adsorbate [30]. Physical adsorption, or physisorption, occurs as a result of electrostatic and van der Waals forces that exist between the adsorbent and adsorbate. Heats of adsorption for

physisorption tend to be low, with ΔH values typically in the range of 2 – 15 kcal/mole [31]. In the case of chemical adsorption, termed chemisorption, the adsorbent forms a chemical bond with the solid surface. Values for ΔH tend to be higher for chemisorption and are often in the range of 15 – 200 kcal/mole [31]. As chemisorption tends to provide the necessary catalysis conditions, it is often the adsorption mode of interest when discussing semiconductor gas sensors.

If the electrical conductivity of a semiconductor is to be used for gas detection, then changes in conductivity must be proportional to the concentration of the gaseous analyte. To understand this relationship, adsorption kinetics must be discussed. The residence time, τ_r, of an adsorbed atom is given by [29]:

$$\tau_r = \tau_o \exp\left(\frac{\Delta H}{RT}\right) \tag{2.24}$$

where τ_o is related to surface vibration times and R is the universal gas constant. The surface coverage, S, of a gaseous species is dependent on both τ_r and the flux, F, of gas molecules per unit area per second through:

$$S = \tau_r F \tag{2.25}$$

Typical units for S are molecules per cm^2. Relating the gas flux to the pressure through the kinetic theory of gases will yield:

$$S = \left(\frac{N_A P}{\sqrt{2\pi MRT}}\right)\tau_o \exp\left(\frac{\Delta H}{RT}\right) \tag{2.26}$$

where N_A is Avogrado's number, P is the partial pressure of the gas, and M is the average molar weight of the gaseous species. Experimental curves of S plotted as a function of P at a given temperature are known as adsorption isotherms [29]. One

particular isotherm derived by Irving Langmuir is of key interest in the field of semiconductor gas sensors [32]. It is based on two assumptions [28]:

1) Adsorption terminates upon the completion of one monolayer.
2) There exists neither surface heterogeneity nor interaction among adsorbed species.

While these assumptions are to some degree impractical for real surfaces, modified isotherms have been developed [31]. Regardless, the derivations of Langmuir provide a sound qualitative relationship between surface coverage and gas concentration. Using assumption 1), any gaseous molecule will reflect off a surface when striking an adsorbed species. Thus, if S_o denotes a completely covered surface, then a concentration of S adsorbed molecules will result in $S_o - S$ available sites [29]. The fluxes for both reflected molecules, F_R, and adsorbed molecules, F_A, are given by:

$$F_R = \left(\frac{S}{S_o}\right)F \qquad F_A = \left(1 - \frac{S}{S_o}\right)F \tag{2.27}$$

Substitution of F_A into (2.25) and subsequent rearrangement will yield:

$$S = \frac{S_o F \tau_r}{S_o + F\tau_r} = \frac{S_o aP}{S_o + aP} \tag{2.28}$$

The constant a is comprised of the grouping of terms, with the exception of P, from (2.26). If $\theta = (S/S_o)$, where θ is defined as the degree of coverage, then (2.28) takes the following form:

$$\theta = \frac{bP}{1 + bP} \tag{2.29}$$

where $b = (a/S_o)$.

When the degree of surface coverage is proportional to the partial pressure, changes in the electrical conductivity may be related to gas concentration. Inspection of (2.29) shows that if bP is small, θ is proportional to P. However, if $bP >> 1$, then θ approaches unity and the lack of proportionality makes the gas sensor insensitive to coverage. If a competition ensues for surface sites between two gas species, A and B, then (2.29) becomes [28]:

$$\theta_A = \frac{b_A P_A}{1 + b_A P_A + b_B P_B} \qquad \theta_B = \frac{b_B P_B}{1 + b_A P_A + b_B P_B} \tag{2.30}$$

If $b_B P_B >> b_A P_A$, then the equations of (2.30) become:

$$\theta_A = \frac{b_A P_A}{1 + b_B P_B} \qquad \theta_B = \frac{b_B P_B}{1 + b_B P_B} \tag{2.31}$$

In the case that $b_B P_B$ is >> 1, the equations of (31) reduce to:

$$\theta_A \approx \frac{b_A P_A}{1 + b_B P_B} \qquad \theta_B \approx 1 \tag{2.32}$$

Thus, if the conductivity of the gas sensor is strongly dependent on species A, then the concentration of either A or B may be measured. However, if the conductivity possesses a strong dependence on species B, it will become independent of the gas concentration as θ_B approaches 1.

The rate of a reaction between A and B may be given by [28]:

$$\text{rate} = k\theta_A\theta_B \tag{2.33}$$

If the rate in (2.33) is much higher than the rate of adsorption of say, A, then θ_A will fall to zero and θ_B will increase. As an example, note that the coverage of oxygen, represented by θ_A in (32) on an *n*-type semiconductor is quite low. The coverage of a

reducing gas, θ_B in (32) is quite high. As the reaction rate between the oxygen and the reducing species increases, θ_A falls to zero, enabling the reducing gas to be detected with a high degree of sensitivity.

2.3. Gas Sensor Parameters

2.3.1. Sensitivity

The sensitivity of a semiconductor gas sensor typically refers to the lowest level of analyte concentration that can be detected in a sensing environment [33]. It is often quantified as the ratio of sensor resistance in air over the sensor resistance in ambient analyte. A common technique employed in the enhancement of sensitivity is the enlargement of sensor surface area. This allows for an increase in the concentration of adsorbed species and thus, greater conductivity changes occur upon introduction of a reducing gas. For metal oxide powders, this may be accomplished through strict temperature control during the calcination and sintering steps. In studies of sol-derived ZnO powders, Ryu *et al*. observed that higher calcination temperatures led to an increase in the average grain diameter, from 80 nm at 500 °C to 800 nm at 900 °C [34]. Subsequent electrical measurements in 250 ppm carbon monoxide (CO) showed the decreased grain size to yield a 1.5 times increase in sensitivity. In research on the effects of ZnO sintering, the relative density of solid-state pellets was seen to increase from 59.6 % at a 1000 °C sintering temperature, to 82.9 % at 1300 °C [26]. Resistivity measurements in the presence of a reducing gas yielded an expected trend

of enhanced sensitivity. An almost two-fold increase in sensitivity to 0.2 % H_2 was found for ~20 nm-sized ZnO powder when compared to powders with a 3.7 μm average grain size [35].

In the realm of thin films, various techniques for grain size control have been employed. In one study, the relationship between morphology and gas sensitivity was compared for ZnO films fabricated via dc magnetron sputtering of both metallic Zn and ceramic ZnO targets [36]. Films grown from metallic targets displayed a larger surface to volume ratio compared to films from ceramic targets due to an inhibition of grain agglomeration. Subsequent conductivity measurements showed these films to possess a higher sensitivity to ambient ozone (O_3) when compared to films grown from ceramic targets. In studies of indium-doped SnO_2, an increase in porosity (and thus surface area) for thermally evaporated films was found to yield enhanced sensitivity to 1000 ppm wood smoke when compared to films prepared by sputtering [37]. Along with surface area, film thickness also influences gas sensor sensitivity. In a study of SnO_2 films grown via chemical vapor deposition (CVD), films with a thickness of 100 nm showed enhanced sensitivity to propane (C_3H_8) gas when compared to 1 μm thick films [6].

Temperature is another factor to consider in gas sensor sensitivity. Consider the reaction of the CO with adsorbed oxygen in the formation of CO_2. If the temperature is too low, CO_2 will not be desorbed and thus, sites on the surface of the semiconductor will become poisoned [6]. A temperature that is too high will deter the adsorption of CO and the necessary recombination reactions will not occur. High temperatures also reduce sensitivity by increasing semiconductor carrier concentration

and decreasing the Debye length [9]. For ZnO gas sensors, optimal working temperatures are in the range of 400 °C – 500 °C [38, 39]. This range however is not definite; the increased activity of nanometer scale ZnO powder has been shown to lower this temperature to around 300 °C [35].

2.3.2. Selectivity

Selectivity is often defined as the ratio of a sensor's ability to detect gases of interest over the sensor's ability to detect gases that are not of interest (interferents) [33]. One method employed in the enhancement of sensor selectivity is the use of filters which allow only certain gases of interest to pass through to the surface of a semiconductor. In a previous study, a 200 μm layer of SnO_2 was coated with silicon dioxide (SiO_2) via CVD [40]. This device displayed higher values of conductivity in ambient hydrogen compared to other reducing gases such as CO and methane (CH_4). The authors attributed this selectivity to a type of molecular sieve created by the SiO_2. Sputtered films of titanium dioxide (TiO_2) with a coating of Pt have also been used in previous research for the selective detection of hydrogen [41]. The Pt films served to dissociate H_2 molecules into H atoms which then migrated to the underlying TiO_2 film.

The peak sensitivity of certain gases may vary as a function of temperature. As such, temperature may be used as a means of attaining desirable levels of selectivity. For SnO_2 based sensors, CH_4 has been shown to possess a sensitivity peak at rather high temperatures when compared to CO and hydrogen [25, 42]. Temperature cycling

of SnO_2-based sensors has yielded peaks in electrical conductivity at 100 °C for hydrogen sulfide (H_2S) and 400 °C for H_2 and CO [43].

2.4. *pn* Junction Theory

Up to now, this review has focused on gas sensing through the use of a single semiconductor type. In the sections to follow, the discussion will evolve into the use of a *pn* interface in the detection of a gaseous ambient. The basic theory and operation of a *pn* junction will first be addressed. It is assumed that this junction is fabricated from one elemental semiconductor, where an *n*-doped region exists in direct physical contact with a *p*-doped region. The concepts detailed here will provide a basis for an understanding of *pn* heterostructure gas sensors, where an interface exists between two different semiconductor materials.

2.4.1. Historical Perspective

In 1940, Bell Labs scientist Russell Ohl was researching crystal detectors for their use in high frequency radio communication when he noticed a voltage reading upon illuminating a silicon specimen with a flashlight [44]. Subsequent research by Ohl and his colleagues would reveal this phenomenon, now known as the photovoltaic effect, to arise from the segregation of impurities during the solidification process [45]. Ohl's discovery marked the birth of the *pn* junction device and, through of series of patents in 1946 (one of which was for an alternating current rectifier), the terms *n* and

p-type were introduced into the public lexicon [46, 47]. William Shockley, John Bardeen, and Walter Brattain would eventually build on this research and create the first junction transistor [48].

2.4.2. Zero Applied Bias

In the following discussion, consider a single crystal silicon specimen comprised of uniformly doped *n* and *p*-type regions, as depicted in Figure 2.4 [49]. These regions lie in direct contact at an abrupt interface, *M*, known as a metallurgical junction [50]. Initially, the existence of a charge carrier concentration gradient exists across the junction, where the concentration of holes varies from $p = p_o$ on the *p*-side to $p = p_{no}$ in the *n*-type region. Likewise, the electron concentration varies from $n = n_o$ in the *n*-region to $n = n_{po}$ on *p*-type side. The hole concentration gradient leads to the generation of a diffusion force which drives the movement of holes on the *p*-side into the *n*-type region, where they recombine with electrons near the interface. A corresponding force in the *n*-region leads to electron migration across *M* and into the *p*-type zone where again, charge carrier recombination ensues in the vicinity of the junction. Under the scenario of zero applied bias, this phenomenon of charge carrier movement does not proceed indefinitely. The net movement of holes from left to right in Figure 2.4(a) results in the exposure of negatively charged ion cores, of concentration N_a, on the *p*-type side near the junction. Similarly, as electrons diffuse across *M* from right to left, they leave behind positively charged donor ions, with a

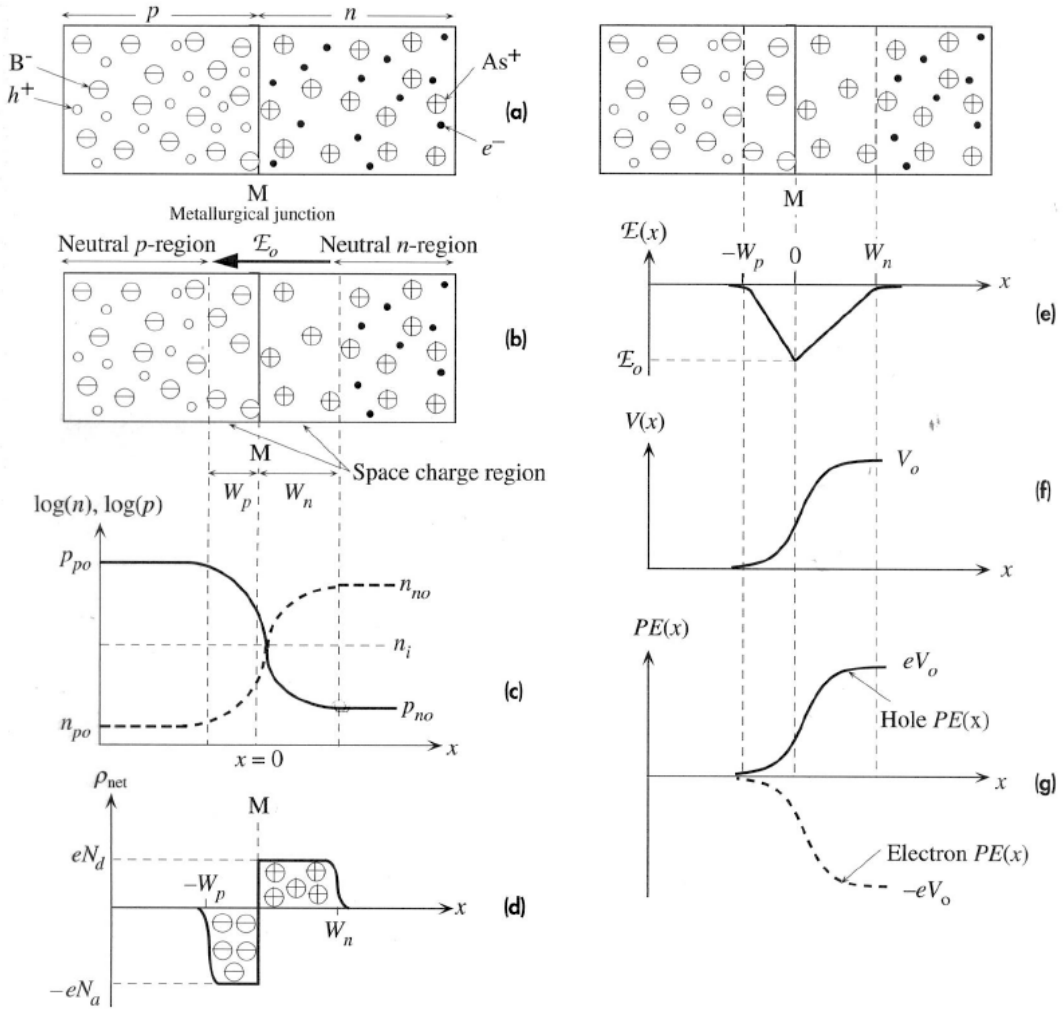

Figure 2.4. The behavior of a *pn* junction. Represented are: (a) the junction prior to charge diffusion, (b) the space charge region after charge migration, (c) the hole and electron concentration profiles, (d) the net space charge density profile, (e) the electric field across the junction, (f) the potential across the junction, and (g) the potential energy profile [49].

concentration N_d, on the *n*-side in the near the interface. The end result is the formation of region near *M* that has become depleted of majority charge carriers. This area, shown in Figure 2.4(b), is known as a space charge region, or depletion region. It must be noted that in the absence of an applied bias, the equilibrium condition $pn = n_i^2$, where n_i is the intrinsic carrier concentration, applies everywhere. The charge carrier concentration profile resulting from the respective diffusion forces is detailed in Figure 2.4(c) The net positive and negative ion cores in the vicinity of *M* induce an internal electric field, E_o, in the negative *x*-direction (from positive donor ions to negative acceptor ions). This electric field serves to drift holes back to the *p*-type side and electrons back toward the *n*-type side. As the diffusion of majority charge carriers continues across the junction, the width of the space charge region increases and thus, the magnitude of the electric field grows. A state of equilibrium is achieved when this internal electric field opposes the forces of diffusion in an equal and opposite manner.

Assuming a uniform *n* and *p*-type doping scenario, the net space charge density, $\rho_{net}(x)$, across the space charge region is shown in Figure 2.4(d). The edges of the space charge layer are denoted as $x = -W_p$ on the *p*-side and $x = W_n$ on the *n*-type side. The metallurgical junction, *M*, is taken as $x = 0$. As such, the values for the net space charge density are given as:

$$\rho_{net}(x) = -eN_a \qquad -W_p < x < 0 \tag{2.34}$$

$$\rho_{net}(x) = eN_d \qquad 0 < x < W_n \tag{2.35}$$

The preservation of charge neutrality then leads to:

$$N_a W_p = N_d W_n \tag{2.36}$$

In Figure 2.4, the assumption was made that $N_a > N_d$. As evident in (2.36), this leads to a reduced space charge region width on the *p*-type side.

To adequately characterize the properties of a *pn* junction, a few key parameters must be ascertained. The first, shown graphically in Figure 2.4(e), is the electric field that arises in the depletion region due to the separation of positive and negative space charge densities. At any point across the junction, the electric field, $E(x)$, is related to the space charge density by the differential of Gauss' Law [51]:

$$\frac{dE(x)}{dx} = \frac{\rho_{net}(x)}{\varepsilon_s} \tag{2.37}$$

where ε_s is the permittivity of the semiconductor. Through substitution of (2.34) into (2.37), the electric field in the *p*-region may found as:

$$E(x) = -\int \frac{eN_a}{\varepsilon_s} dx = \frac{-eN_a}{\varepsilon_s} x + A \tag{2.38}$$

The constant of integration, A, can be found through setting $E(x) = 0$ at $x = -W_p$. This yields:

$$E(x) = \frac{-eN_a}{\varepsilon_s}(x + W_p) \qquad -W_p \le x \le 0 \tag{2.39}$$

A similar treatment in the *n*-region yields:

$$E(x) = \frac{-eN_d}{\varepsilon_s}(W_n - x) \qquad 0 \le x \le -W_n \tag{2.40}$$

An analysis of (2.39) and (2.49) shows the magnitude of the electric field to be greatest at $x = 0$, i.e. at the junction. From a conceptual standpoint, one may look to the definition of an electric field in conjunction with Figure 2.4(e). The electric field at any one point represents the magnitude and direction of a force experienced by a

positive unit test charge placed in the field at the point in question [51]. A hole traveling from left to right in Figure 2.4(b) will be subject to an increasing force opposite to its direction of diffusion due to the positive ion cores present in the space charge region in the *n*-type side. This force will reach a peak in magnitude at the metallurgical junction. A hole that were to travel this far would then be subject to a gradually decreasing force due to the presence of electrons in the neutral *n*-region. A similar scenario may be theorized for an electron moving from right to left.

A second parameter of interest when analyzing a *pn* junction is that of the built-in potential. At any point along the junction, the potential, $V(x)$, may be found through the relationship:

$$E(x) = -\frac{dV(x)}{dx} \tag{2.41}$$

Through an integration of (2.39), the potential in the *p*-type region is given by:

$$V(x) = \int \frac{eN_a}{\varepsilon_s}(x + W_p) = \frac{eN_a}{\varepsilon_s}\left(\frac{x^2}{2} + W_p x\right) + B \tag{2.42}$$

where B is a constant of integration. Setting the potential equal to zero at $x = -W_p$ gives:

$$V(x) = \frac{eN_a}{2\varepsilon_s}(x + W_p)^2 \qquad -W_p \le x \le 0 \tag{2.43}$$

Through (2.41), it is clear that the electric field, $E(x)$, represents the negative in the rate of change in potential across the junction. Inspection of Figure 2.4(e) shows that a plot of potential will possess a positive slope with an inflection point at *M* and a maximum at W_n. It is this maximum at W_n that represents the magnitude of the potential barrier that charge carriers must surmount when successfully crossing the

space charge region. If $V(x)$ is found for the *p*-type side in the manner described above, setting $x = W_n$ will yield:

$$V_o = \frac{e}{2\varepsilon_s}(N_d W_n^2 + N_a W_p^2) = \frac{eN_a N_d W_o^2}{2\varepsilon(N_a + N_d)} \tag{2.44}$$

where V_o represents the built-in potential barrier and $W_o = (W_n + W_p)$ is the width of the space charge region. A plot of $V(x)$ versus position along the junction is shown in Figure 2.4(f). The graph of Figure 2.4(g) is a consequence of the equal and opposite elementary charges that electrons and holes possess. A relationship between the concentration of dopants and the built-in potential barrier can be made through the use particle statistics. The Maxwell-Boltzmann distribution function is an exponential factor with the following form [52]:

$$P(E_p) = A^{-1} \exp\left(\frac{-E_p}{kT}\right) \tag{2.45}$$

where $P(E_p)$ is the fraction of particles with energy E_p, A is a normalization constant, k is Boltzmann's constant, and T is the temperature. Since $E_p = -eV_o$ for electrons, substitution yields:

$$\frac{n_{po}}{n_{no}} = \exp\left(-\frac{eV_o}{kT}\right) \tag{2.46}$$

It should be noted that, due to the Pauli exclusion principle, statistical distributions of electrons are typically studied using Fermi-Dirac statistics. However, the assumption will be made that the concentration of electrons residing in the conduction band is too low for the Pauli exclusion principle to become applicable.

2.4.3. Forward Applied Bias

The scenario of a *pn* junction under a forward applied bias can be realized by the application of voltage source, V, where the positive lead is in electrical contact with the *p*-type side and the negative lead is connected to the *n*-type side. The neutral *p* and *n*-type regions of the junction possess a greater number of mobile charge carriers than the space charge region. As such, the bulk of any applied voltage is dropped across W_o, the width of the space charge region. This acts to reduce the forces against charge carrier diffusion, i.e., it counteracts the internal electric field and lowers the built-in potential barrier. Figure 2.5 details the carrier concentration profile of a *pn* junction under a forward bias [49]. A lowering of the built-in potential barrier, from V_o to ($V_o - V$), results in the diffusion of minority charge carriers. Excess holes migrate

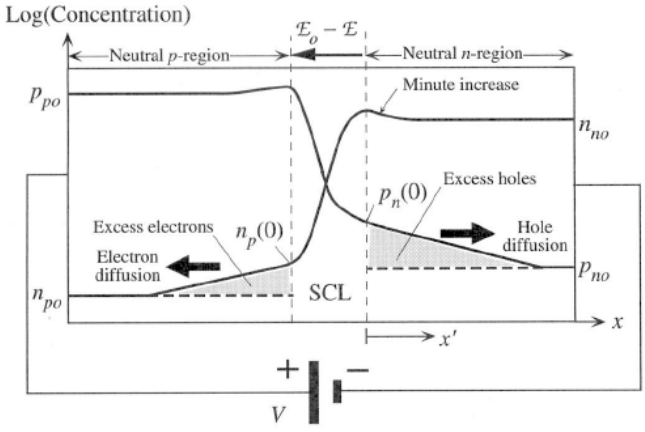

Figure 2.5. The charge concentration profile of *pn* junction under forward bias [49].

into the *n*-type region, with a corresponding influx of electrons into the *p*-region. Using Boltzmann statistics, the probability of a hole surmounting the lowered potential barrier is given by:

$$p_n(0) = p_{po} \exp\left[-\frac{e(V_o - V)}{kT} \right] \tag{2.47}$$

where $p_n(0)$ is the concentration of holes just outside the *n*-region depletion layer (x' in Figure 2.5). Using the same techniques in the derivation of (2.46), the relationship between applied voltage and excess minority carrier concentration can be found:

$$p_n(0) = p_{no} \exp\left(\frac{eV}{kT} \right) \qquad n_p(0) = n_{po} \exp\left(\frac{eV}{kT} \right) \tag{2.48}$$

where $n_p(0)$ is the electron concentration just outside the space region on the *p*-type side. The equations in (2.48) are known as the law of the junction.

When holes enter the neutral *n*-type region, recombination begins to occur between these excess minority charge carriers and the majority electrons. The electrons lost due to recombination are replenished by the negative lead of the voltage source. The electrical current arising from the diffusion of holes is sustained through the positive voltage lead, which acts to replenish the supply of holes in the *p*-side. This scenario plays out in a similar manner regarding minority electrons entering the *p*-side. The electrons lost due to recombination with holes in the *p*-side can be replaced by the negative voltage terminal on the *n*-side. The current that results from the injection of minority charge carriers into neutral zones is known as the diffusion current.

As minority charge carriers cross the junction, some recombination will occur in the space charge region. As such, the total current through a *pn* junction in forward

bias is a sum of both the diffusion current and this recombination current. The diffusion current, I_d, is given by the ideal diode, or Shockley equation:

$$I_d = I_{do}\left[\exp\left(\frac{eV}{kT}\right)-1\right] \tag{2.49}$$

where I_{do} is a constant related to the doping concentration and material. The recombination current is given by:

$$I_r = I_{ro}\left[\exp\left(\frac{eV}{2kT}\right)-1\right] \tag{2.50}$$

where I_{ro} is also a material-related constant. Thus the total current, I, is given by:

$$I = I_o\left[\exp\left(\frac{eV}{\eta kT}\right)-1\right] \tag{2.51}$$

where I_o is a constant and η takes on a value of 1 for diffusion current and 2 for recombination current.

2.4.4. Reverse Bias

Shown in Figure 2.6 is the minority concentration profile of a *pn* junction under a reverse bias [49]. As in the forward bias scenario, the majority of an applied voltage is dropped across the space charge region. The configuration of the source leads results in an increase in the built-in potential barrier and a widening of the space charge region. The majority charge carriers in the respective neutral regions are attracted towards the voltage leads and away from the space charge region. The

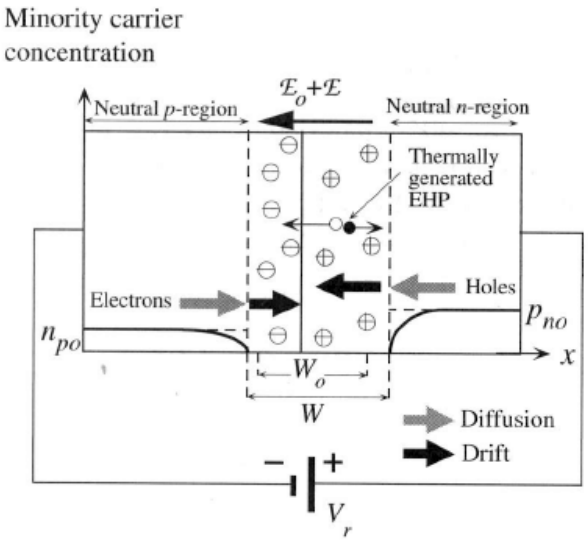

Figure 2.6. The minority charge concentration profile of *pn* junction in reverse bias [49].

current resulting from electron flow to the positive voltage lead is not sustained simply due to the lack of an electron supply to that side of the junction. Electrons are not adequately supplied by the *p*-type side due to the relative absence of that charge carrier in that region. The lack of current flow under a reverse bias is the basis of the rectification behavior found in *pn* junctions.

While the current in a *pn* junction under reverse bias may be limited, it is still present and has its origin from two possible scenarios. The first, as shown in Figure 2.6, is due to the existence of a small minority charge carrier concentration gradient. In the bulk region of the *n*-type side, the concentration of holes, p_{no}, is higher than in the vicinity of the space charge region. This leads to a small diffusion current of holes that, upon entering the space charge region, are drifted across the junction due to the

electric field. The second cause for current flow is due to thermally generated electron-hole pairs in the space charge region. Upon pair formation, the internal electric field serves to drift the charge carriers toward the neutral regions.

2.4.5. *pn* Junction Capacitance

A *pn* junction in forward or reverse bias will possess a space charge capacitance, C_{dl}, resulting from the separation of positively and negatively charged ion cores in the depletion region. This capacitance is related to the applied bias voltage by [53]:

$$C_{dl} = \frac{\varepsilon_s A}{W_o} = \frac{A}{(V_o \pm V)^{1/2}} \left[\frac{e\varepsilon_s N_a N_d}{2(N_a + N_d)} \right]^{1/2} \tag{2.52}$$

where A is the cross-sectional area at the edges of the space charge region. The basic form of (2.52) is the same as that for a parallel plate capacitor, the only difference being the voltage dependence of W_o. The sign in the expression $(V_o \pm V)^{1/2}$ will be minus for forward bias and plus for reverse bias. For a DC bias with a small AC voltage, C_{dl} is almost independent of frequency below 10^9 Hz [53]. This is due to the free charge carrier movement responsible for the ionization/deionization processes in the space charge region.

Under a forward bias, an additional contribution to capacitance is made by the rearrangement of minority charge carriers injected into the neutral *n* and *p*-type regions. This diffusion capacitance, C_{diff}, may be defined by:

$$C_{diff} = \frac{eI\tau}{2kT} \tag{2.53}$$

where τ is the average lifetime of the minority charge carrier. Above the characteristic frequency for recombination, excess minority charge carriers are unable to follow the applied AC voltage. At this point, the contribution of the diffusion capacitance relaxes. The total capacitance, C_j, of a *pn* junction under forward bias may be expressed as:

$$C_j = C_{diff} + C_{dl} \tag{2.54}$$

where $C_j \approx C_{dl}$ at very high frequencies. As shown in Figure 2.7, both C_{diff} and C_{dl} may be found individually through a plot of junction capacitance versus frequency [53].

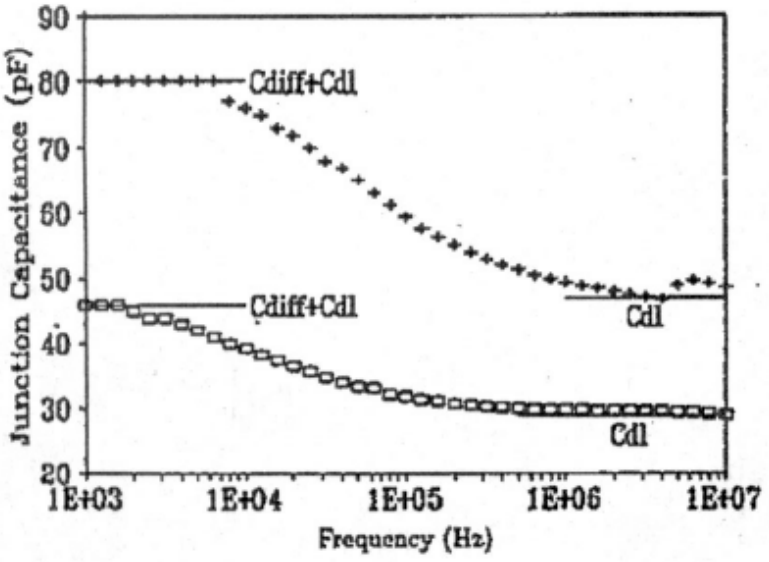

Figure 2.7. The capacitance profile of a *pn* junction at forward biases of 0.2 V (□) and 0.3 V (+) [53].

2.5. *pn* Heterojunctions

When two chemically different semiconductor materials, one *p*-type and one *n*-type, are used to form a junction, the resulting structure is known as a *pn* heterojunction [54]. The band structure of a *pn*-heterojunction is shown in Figure 2.8. Upon bringing the two semiconductors into contact, Fermi levels (E_F) align in the establishment of equilibrium [49]. The work function (Φ) and electron affinities (χ) may be defined, respectively, as the energy required in removing an electron from the Fermi level and from the bottom of the conduction band (E_c) [55]. As charges move in the attainment of equilibrium,band bending is observed. The differing boundary conditions at the junction lead to band discontinuities, denoted as ΔE_c and ΔE_v for the conduction and

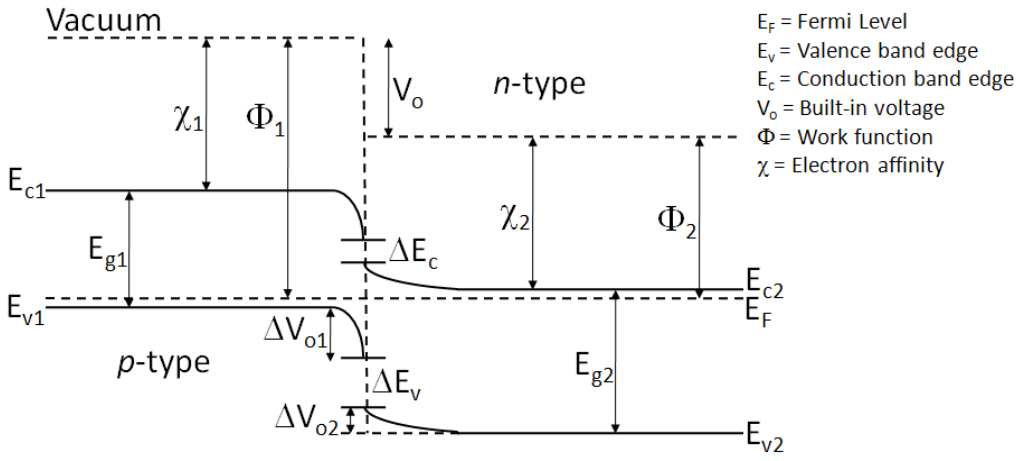

Figure 2.8. The band structure of pn heterojunction. As charges move in the attainment of electroneutrality, band bending is observed.

valence bands, respectively. These may be expressed as follows:

$$\Delta E_c = E_{c1} - E_{c2} - eV_o \tag{2.55}$$

$$\Delta E_v = E_{g1} - E_{g2} - \Delta E_c \tag{2.56}$$

where E_{c1} and E_{c2} are the conduction band edges, E_{g1} and E_{g2} are the band gaps, and V_o is the built-in voltage. The band discontinuities at the interface result in different barrier magnitudes for the two charge carrier types. As such, the current through the heterojunction will be dominated by either holes or electrons. The current dependence with applied voltage may be given as [55]:

$$I = A\exp\left(-\frac{eV_{B2}}{kT}\right) - B\exp\left(-\frac{eV_{B1}}{kT}\right) \tag{2.57}$$

where V_{B1} represents the barrier that carriers in the *p*-type semiconductor of Figure 2.8 must overcome and V_{B2} is the barrier for carriers travelling in the opposite direction. The coefficients A and B depend on such parameters as carrier effective mass and doping levels. For the heterojunction of Figure 2.8, the barrier V_{B2} for electrons is smaller than that for holes and consequently, electrons will dominate the heterojunction current for this particular case.

2.6. *pn* Heterostructure Gas Sensors

2.6.1. Bulk Heterocontacts

The use of the term heterojunction implies the existence of a continuous interface down to the atomistic level. When a high degree of non-contact area exists,

the resulting configuration is typically referred to as a heterostructure or heterocontact. The use of heterocontacts in gas detection was introduced by Nakamura *et al.* in 1986 and employed bulk *p*-CuO and *n*-ZnO disks mechanically pressed into contact [12]. Experimental results from this device showed CO sensitivities that were 2 to 3 times higher than that for propane or H_2. These sensitivity values were obtained at a relatively low operating temperature of 260 °C. Subsequent studies for individual ZnO and CuO disks yielded negligible sensitivities for CO and thus, an interaction between the ZnO and CuO was proposed as follows [56]:

$$[n\text{-ZnO}]: O_2 + 2e^- \rightarrow 2O^- \tag{2.58}$$

$$[p\text{-CuO}]: 2CO + 2h^+ \rightarrow 2CO^+ \tag{2.59}$$

$$[\text{interface}]: 2CO^+ + 2O^- \rightarrow 2CO_2 \tag{2.60}$$

The reaction in (2.60) serves to free up both electrons and holes, thus allowing for the sensitive detection of CO through a decrease in interfacial resistance.

As hydrogen gas is highly combustible, most semiconductor gas sensors are more sensitive to hydrogen than CO. As such, the findings of enhanced sensitivity to CO by Nakamura *et al*. were investigated further. Subsequent findings revealed that the scenario of CO selectivity depended heavily upon the starting CuO material. In studies by Jung *et al*. using highly purified CuO powder, the phenomenon of CO selectivity was not observed and the heterocontacts showed a high sensitivity to H_2 over CO [57]. The authors then doped the CuO with 2 mole % Na and left the ZnO material undoped. This action led to the previously observed sensitivity to CO over H_2. An analysis of the CuO lattice parameter via XRD data showed the solubility limit of

Na in the CuO to be around 1 mole %. Upon exceeding this molar percentage, the Na was assumed to precipitate at the grain boundaries or surface of the CuO. It was concluded that the excess electropositive Na stabilized molecular chemisorption and promoted the dissociation of such molecules as CO and O_2, thus leading to the observed CO sensitivity. In a later study, CuO/ZnO heterocontacts were fabricated using 1 mole % Na additions to the CuO [58]. As seen previously, the heterocontacts made with doped CuO showed enhanced selectivity to CO over H_2 while the structures with undoped CuO showed high sensitivities to H_2 over CO. The researchers then analyzed the microstructure of both the doped and undoped CuO. Their findings showed the average grain size to be around 7 – 8 μm for the doped CuO and 1 – 2 μm for the undoped CuO. It was thus concluded that CO sensitivity and selectivity is independent of the CuO surface area. X-ray photoelectron spectroscopy (XPS) showed the doped CuO to possess a 2.5 times greater Cu:O ratio over the undoped CuO, indicating a more reduced surface. This finding led the authors to assume that Na doping of CuO leads to more stable CO adsorbates. Research on improving the stability of CO on undoped CuO has also been performed. In studies by Nakamura *et al*., key emphasis was put on ensuring a reaction between stable CO on the undoped CuO surface and adsorbed oxygen on the *n*-ZnO [59]. This involved an inhibition of the oxidation reactions for CO on CuO. It was found that quenching CuO after the sintering step induced stability in both the lattice and adsorbed oxygen. This in turn slowed reactions between CO and oxygen on the CuO surface.

The doping of CuO/ZnO heterocontacts in the improvement of H_2 sensitivity has also been studied. Research by Aygun *et al*. demonstrated improved hydrogen

sensitivity when CuO was doped with monovalent and divalent metals [14]. This effect was attributed to a possible increase in hole density and the potential for second phase hydrogen adsorption sites. The doping of CuO with Li yielded enhanced rectification characteristics due to the possible compensation of minority charge carriers. Further studies on the effects of dopants have shown increased hydrogen sensitivity for Ni-doped CuO/Ga-doped ZnO heterocontacts [13]. The capacitance behavior of Ni-doped CuO/ZnO has also been studied [15]. It was found that the heterocontact capacitance displayed a strong frequency dependence in ambient hydrogen at low (~100 Hz) frequencies. This lead to the assumption that Ni-doping plays has an effect on minority charge carrier concentration and lifetime. It should be noted that while CuO/ZnO heterocontacts tend to be the most widely studied heterostructure gas sensor, other material combinations such as $Ni_{1-x}Li_xO$/ZnO [60], *n*-ZnO/*n*-SnO_2 [61], and La_2CuO_4/ZnO [62] have also been researched.

The use of CuO/ZnO or La_2CuO_4/ZnO in humidity sensing capacities has been explored. The mechanism of these sensors is based on the electrolysis of water at the heterocontact interface [63]. The reaction begins with the injection of holes into the adsorbed water by the p-type semiconductor. This gives rise to protons in the water phase which are then liberated by the *n*-type semiconductor, resulting in electrolysis of the adsorbed water. In forward bias, an increase in humidity results in an increase in current across the heterocontact.

The electrical properties of a *pn* interface dominate device functionality. As such, response time and sensitivity may be increased if the analyte is provided with a less circuitous path to the heterocontact junction. It is for this reason that the parameter

of porosity is a critical factor to consider in heterocontact gas sensor design. Shown in Figure 2.9 are two current-voltage (*I*-*V*) curves detailing the response of dense (Figure 2.9(a)) and porous (Figure 2.9(b)) CuO/ZnO heterocontacts in air and 1.1 % H_2 [64]. The response of the heterocontact to H_2 is seen to be significantly larger in the more porous heterocontact.

Porosity however is not the only factor to consider in effective heterocontact fabrication. A large interfacial area between two semiconductors ensures adequate magnitudes of response in the detection of a gaseous species. This consideration has driven the need to find adequate geometries that can accommodate such a scenario. One possible avenue lies in the realm of planar thin films.

2.6.2. Thin Film Heterostructures

To date, few published works exist on the use of thin film *pn* heterocontacts for gas detection. One study performed by Baek and Tuller utilized sputtered CuO on bulk polycrystalline ZnO substrates [65]. The resulting *I*-*V* curves showed the heterocontacts to exhibit strong rectification characteristics. A subsequent study of these structures by the same authors showed the current transport in the heterocontacts to be consistent with a thermal process model as opposed to tunneling [66]. Experiments revealed this thermally-activated forward bias current to increase as the partial pressure of oxygen was decreased [66]. This finding led to the assumption of a relationship between barrier height and the adsorption of oxygen at the heterocontact interface.

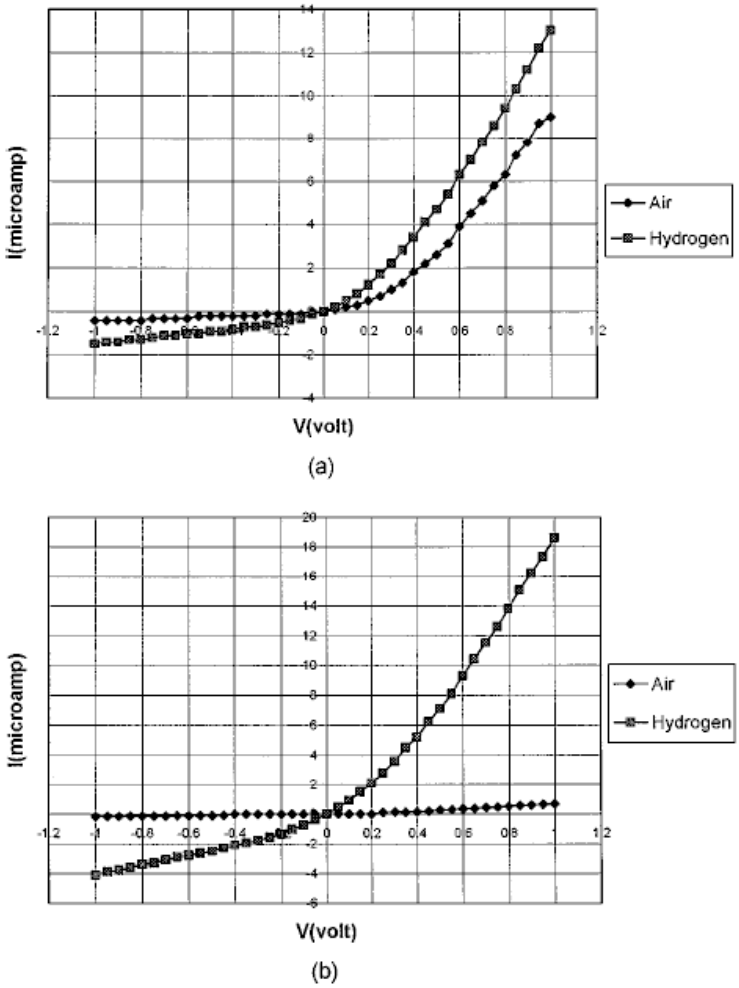

Figure 2.9. The current-voltage (*I*-*V*) response of dense (a) and porous (b) CuO/ZnO heterocontacts. The more porous heterocontact displays enhanced H_2 sensitivity [64].

The fabrication of a heterostructure comprised of planar CuO and ZnO thin films has in fact been successful. In a published work by Mridha and Basak, chemical solution (sol-gel) methods were employed in the deposition of thin film CuO on a base ZnO thin film [67]. These heterocontacts exhibited strong rectification characteristics

in air; forward bias/reverse bias current ratios as high as 485 were recorded at 300 °C. This ratio decreased to 8.4 in the presence of H_2 at 300 °C, a possible consequence of enhanced minority charge concentrations under reducing conditions. The *I-V* curves at 300 °C also revealed the current of the heterocontacts at 16 V to be six times higher in ambient H_2 than in air. The authors also explored the effects of CuO film thickness on device sensitivity. An increase in film thickness, from 0.43 μm to 1.2 μm, corresponded to a 40-fold increase in H_2 sensitivity. This trend was attributed to an increase in adsorbed oxygen content associated with the thicker films.

The final section of this review will focus on the sol-gel fabrication process. The synthesis of thin films via sol-gel deposition is appealing due to the reduced cost of necessary equipment, the low temperatures at which crystallization may take place, and the potential for large area coverage [18]. Sol-gel routes also allow for an optimal degree of process control, since desired film characteristics may be realized through the introduction of specific additives to the precursor solutions.

2.7. Sol-Gel Fabrication

A diagram of the sol-gel process, also known as wet-chemical processing, is shown in Figure 2.10 [68]. For solid-state powder processing, a suspension of colloidal particles (a sol) is made and the desired powders are precipitated out. Precipitation is usually accomplished through a modification of the sol pH levels. The powders are then dried to drive out organics and solid-state processing techniques may be employed in the formation of disks or pellets. The method of processing thin films

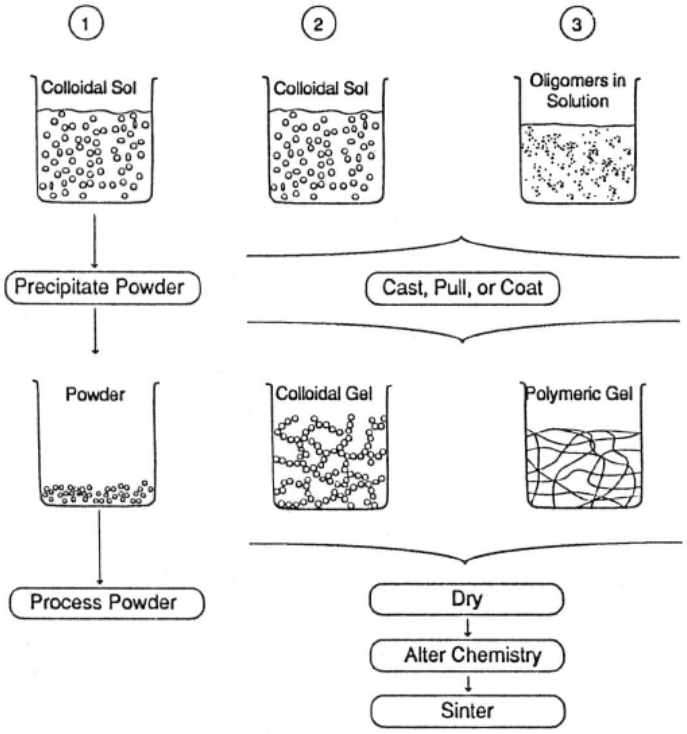

Figure 2.10. A basic diagram of the sol-gel process used to generate powders (1) and films (2 and 3) [68].

also involves the initial step of forming a colloidal sol. However, the goal in this approach is not to precipitate out a powder, but rather to link the particles in the formation of gel. The gel consists of a porous networked solid phase filled with a liquid phase [18]. This gel can then be processed in one of two manners. In a single-stage process, the gel is rapidly heated to a crystallization temperature, whereby both organic burnout and crystallization may take place simultaneously [69]. The appeal to the single-stage process tends to be in the realm of producing highly dense materials.

According to previous research, when a material undergoes crystallization prior to densification, material transport by diffusion is slower through impinging crystals than by a viscous flow mechanism through the material matrix [70]. However, if a material is heated rapidly, densification will occur prior to crystallization. The end result will be a more dense material. Referring to earlier discussions on porosity, the single-stage heating process may not be suitable for specific heterocontact fabrication processes. If the gel is processed in a two-stage manner, the initial heat treatment is known as pyrolysis and generally involves the use of a hot plate held in a 200 °C to 400 °C temperature range. In the range of room temperature to 150 °C, the gel may shrink due to capillary contraction and lose weight due to adsorbed water and solvent evaporation [18]. From about 150 °C to 400 °C, organic residues are burned out and tiny pores may remain. The ultimate formation of a highly crystalline thin film depends on a dried gel consisting of atoms arranged in a manner very close to that of the final crystalline phase. As such, the evolution from short to medium-range order is essential during pyrolysis [69]. The second heating stage, annealing, is typically above 400 °C and is often termed the crystallization step. It is in this step that energetic barriers to nucleation may be surmounted in the attainment of a crystalline microstructure. Shown in Figure 2.11 is a schematic depicting the driving force for crystallization; a reduction in the free energy of the system.

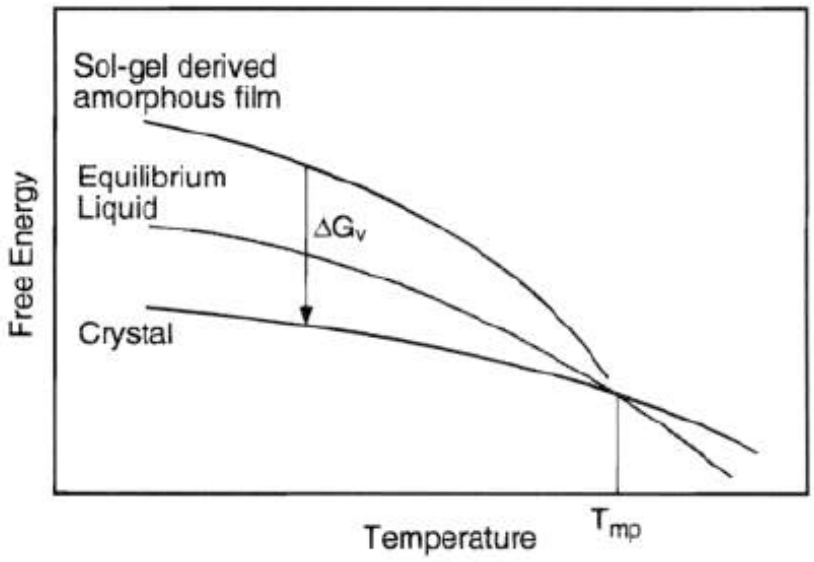

Figure 2.11. A diagram showing the free energy difference between an amorphous film and a crystalline ceramic phase. A minimization of Gibbs free energy drives the crystallization process [69].

Chapter 3. Experimental

This chapter is designed so as to give a brief overview of the methods and materials used in this work. A more detailed account of the experimental procedures is given in the subsequent results chapters.

3.1. ZnO and CuO Precursors

All thin films in this study were fabricated via wet chemical (sol-gel) methods. Zinc acetate dihydrate ($Zn(CH_3COO)_2 \cdot 2H_2O$: Alfa Aesar, 98.0 – 101.0%) and copper acetate monohydrate ($Cu(CH_3COO)_2 \cdot 2H_2O$: Alfa Aesar, 98.0 – 102.0%) were employed as solutes for the ZnO and CuO precursors, respectively. For the ZnO solutions, dissolution of the zinc acetate was performed using either dimethylformamide (DMF: Alfa Aesar, 99.8+%) or 2-methoxyethanol (MOE: Alfa Aesar, 99%) as the solvent. Isopropanol (Mallinckrodt, 99.5%) was employed as the solvent for all CuO precursors. Monoethanolamine (MEA: Alfa Aesar, 99+%) was introduced into specific solutions as a stabilizing agent, while the use of de-ionized (DI) water served to facilitate hydrolysis of the solute. The addition of polyethylene glycol (PEG-400: Alfa Aesar) to CuO precursors was necessary for optimal solution viscosity. Molarity was held constant at 0.6 M for the ZnO precursors and 0.25 M for the CuO solutions. The mixed solutions were synthesized by combining CuO and MOE-based ZnO precursors so as to keep a 1:1 molar ratio of Cu:Zn atoms.

3.2. Film Deposition and Heat Treatment

The solutions were loaded into 3 mL syringes equipped with 0.2 μm filters (Fisherbrand). They were then deposited on the substrates in a drop-by-drop fashion. Depositions were performed via spin-coating (Laurel Technologies Corporation) at 3000 rpm for 30 s. Heterostructure and mixed solution layers were deposited on <100> silicon (Sumco Corp., USA), while microscope glass (VWR International) was used as substrates for the DMF-based ZnO thin films. All substrates were cleaned with isopropanol prior to deposition. For the heterostructure study, two sample types were employed; ZnO on CuO (ZnO/CuO) and CuO on ZnO (CuO/ZnO). Patterning of the top oxide film was performed through lithography and etching procedures. The top ZnO film in the ZnO/CuO structures was found to etch readily in a 100:1 ratio of hydrochloric acid (HCl: EMD Chemicals Inc., 36.5 – 38.0%) to DI water. For the CuO/ZnO heterostructures, suitable masking of the base ZnO film was achieved prior to depositing the top CuO layer.

A two-stage heating process was employed for all thin films in this research. The initial pyrolysis (organic burnout) treatment was performed on a hot plate in the temperature range of 200 °C – 400 °C. Annealing took place in a furnace open to air, after which the films were allowed to cool to room temperature. For the heterostructures and DMF-based ZnO films, the annealing temperature was held constant at 550°C and the films were allowed to crystallize for 1 hour. In the mixed solution study, annealing temperature was varied between 700 °C – 900 °C and crystallization times of 1, 5, and 10 hours were used.

3.3. Film Characterization

Crystal structure and preferred orientation were characterized through θ-2θ and rocking curve (ω) scans using a Bruker D8 Discover X-ray diffractometer (XRD) with Cu K_α radiation. Film morphology and grain size analysis was performed through scanning electron microscopy (SEM) and contact mode atomic force microscopy (AFM). Electron microscopy was performed on a FEI Quanta 200 Environmental SEM operated in a voltage range of 5 kV – 15 kV. AFM images were attained on a Digital Instruments Nanoscope IIIa using silicon nitride tips (Veeco). Energy Dispersive Spectroscopy (EDS) was done using a Noran System SIX setup at 15 kV. A Tencor AlphaStep 500 profilometer was used for film thickness measurements.

The gas sensing characteristics of the heterostructures were examined through current-voltage (*I*-*V*) measurements in a NorECs Probostat high temperature conductivity cell. A schematic of the test setup is shown in Figure 3.1. The heterostructures were first affixed to alumina plates using conductive silver epoxy (Duralco 124). The films were then connected via platinum wire electrodes. Sensor tests were performed in a tube furnace at a temperature of 200 °C. Dry air (N_2:O_2 = 4:1) and hydrogen (4000 ppm) ambients were employed to test sensor response. The flow rate and gas concentration were controlled by mass flow controllers (Omega, FMA 5506/5512) with a fixed total flow rate of 200 sccm. Heterostructures were heated to 200 °C and allowed to equilibrate for 30 min. A high voltage source measurement unit (Keithley 237) was used to obtain *I*-*V* data. The applied bias ranged

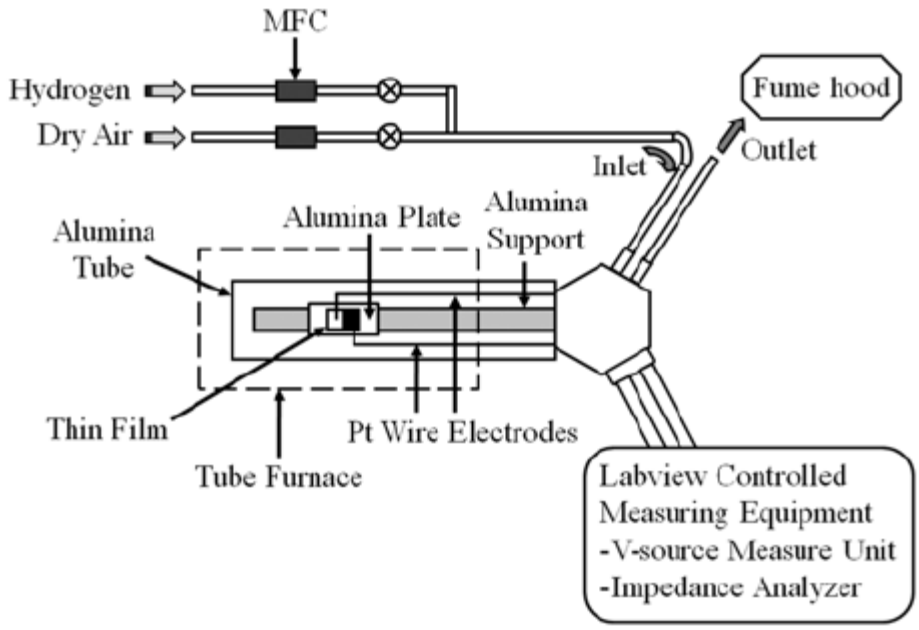

Figure 3.1. A schematic of the test setup used to attain *I-V* data.

from -6 V to +6 V at a step size of 1 V.A delay time of 1 second was employed after applying voltages, upon which the current was measured.

The optical properties of the DMF-based ZnO films were investigated using a custom-built spectrometer. This unit was comprised of a double-grating monochromator equipped with a 250 W xenon lamp source (Oriel) and silicon diode detector. Transmission and reflection spectra were measured at a 5° beam incidence angle in the UV-visible spectral range. The absorption coefficient, α, was calculated using the measured transmission and reflection coefficients, as well as film thickness. The effective refractive index (not accounting for surface roughness), *n*, of the films was measured at 633 nm using a Filmetrix spectrometer. The electrical resistivity of

the DMF-based ZnO films was measured via the van der Pauw technique (Lakeshore 7504) under constant UV light supplied by a low pressure mercury (Hg) lamp.

References

[1] C. Wagner, J. Chem. Phys. 18/1 (1950) 69.
[2] W.H. Brattain, J. Bardeen, The Bell System Technical Journal 32/1 (1953) 1.
[3] T. Seiyama, A. Kato, K. Fujiishi, M. Nagatani, Anal. Chem. 34/11 (1962) 1502.
[4] N. Taguchi, Japan Patent No. 45-38200 (1962).
[5] K. Kalyanasundaram, P.I. Gouma, in: D.K. Aswal, S.K. Gupta (Eds.), Science and Technology of Chemiresistor Gas Sensors, Nova Publishers, New York, 2007.
[6] H.L. Hartnagel, A.L. Dawar, A.K. Jain, C. Jagadish, Semiconducting Transparent Thin Films, Institute of Physics, New York, 1995.
[7] M. Kawasaki, A. Ohtomo, I. Ohkubo, H. Koinuma, Z.K. Tang, Y. P., G.K.L. Wong, B.P. Zhang, Y. Segawa, Mater. Sci. Eng., B 56 (1998) 239.
[8] U. Ozgur, Y.I. Alivov, C. Liu, A. Teke, M.A. Reshchikov, S. Dogan, V. Avrutin, S.-J. Cho, H. Morkoc, J. Appl. Phys. 98 (2005) 041301.
[9] G. Eranna, B.C. Joshi, D.P. Runthala, R.P. Gupta, Crit. Rev. Solid State Mater. Sci. 29 (2004) 111.
[10] R.G. German, K. Klier, G.W. Simmons, F.B. P., J.B. Bulko, T.P. Kobylinski, J. Catal. 56/3 (1979) 407.
[11] J.R. Jensen, T. Johannessen, S. Wedel, H. Livbjerg, J. Catal. 218 (2003) 67.
[12] Y. Nakamura, A. Ando, T. Tsurutani, O. Okada, M. Miyayama, K. Koumoto, H. Yanagida, Chem. Lett. (1986) 413.
[13] S. Aygun, D. Cann, J. Phys. Chem. B 109 (2005) 7878.
[14] S. Aygun, D. Cann, Sensors and Actuators B 106 (2005) 837.
[15] S. Kwon, S. Aygun, D.P. Cann, Sensor Letters 3/3 (2005) 1.
[16] V. Musat, B. Teixeira, E. Fortunato, R.C.C. Monteiro, P. Vilarinho, Surf. Coat. Technol. 180-181 (2004) 659.
[17] Z.Q. Xu, H. Deng, Y. Li, Q.H. Guo, Y.R. Li, Mater. Res. Bull. 41 (2006) 354.
[18] G. Yi, M. Sayer, Ceramic Bulletin 70 (1991) 1173.
[19] D.M. Smyth, The Defect Chemistry of Metal Oxides, Oxford University Press, New York, 2000.
[20] D.R. Gaskell, Introduction to the Thermodynamics of Materials, Taylor and Francis, New York, 2003.
[21] A.F. Kohan, G. Ceder, D. Morgan, C.G. Van de Walle, Physical Review B 61/22 (2000).
[22] A. Janotti, C.G. Van de Walle, Physical Review B 76 (2007).
[23] F.A. Kroger, The Chemistry of Imperfect Crystals, American Elsevier Publishing Company, Inc., New York, 1974.

[24] A.J. Moulson, J.M. Herbert, Electroceramics: Materials, Properties, and applications, John Wiley & Sons Ltd., West Sussex, 2003.
[25] S.R. Morrison, Sensors and Actuators 12 (1987) 425.
[26] M. Takata, D. Tsubone, H. Yanagida, J. Am. Ceram. Soc. 59/1-2 (1976) 4.
[27] J.H. Lunsford, Catalysis Reviews 8 (1973) 135.
[28] S.J. Gentry, T.A. Jones, Sensors and Actuators 10 (1986) 141.
[29] G.A. Somorjai, Introduction to Surface Chemistry and Catalysis, John Wiley and Sons, Inc., New York, 1994.
[30] K. Tadanaga, T. Minami, in: R.M. Almeida (Ed.), Characterization of Sol-Gel Materials and Products, vol. 2, Springer, New York, 2005.
[31] G.A. Somorjai, Principles of Surface Chemistry, Prentice-Hall, Inc, Englewood Cliffs, 1972.
[32] I. Langmuir, J. Am. Chem. Soc. 40 (1918) 1361.
[33] D.M. Wilson, S. Hoyt, J. Janata, K. Booksh, L. Obando, IEEE Sens. J. 1/4 (2001) 256.
[34] H.-W. Ryu, B.-S. Park, S.A. Akbar, W.-S. Lee, K.-J. Hong, Y.-J. Seo, D.-C. Shin, J.-S. Park, G.-P. Choi, Sensors and Actuators B 96 (2003) 717.
[35] J. Xu, Q. Pan, Y.a. Shun, Z. Tian, Sensors and Actuators B 66 (2000) 277.
[36] M. Suchea, S. Christoulakis, K. Moschovis, N. Katsarakis, G. Kiriakidis, Thin Solid Films 515 (2006) 551.
[37] A. Salehi, Thin Solid Films 416 (2002) 260.
[38] X.L. Cheng, H. Zhao, L.H. Huo, S. Gao, J.G. Zhao, Sensors and Actuators B 102 (2004) 248.
[39] Y. Xu, X. Zhou, O.T. Sorensen, Sensors and Actuators B 65 (2000) 2.
[40] K. Fukui, K. Komatsu, in: T. Seiyama, K. Fueki, J. Shiokawa, S. Suzuki (Eds.), Proceedings of the International Meeting on Chemical Sensors, Elsevier, Japan, 1983, p. 52.
[41] L.A. Harris, J. Electrochem. Soc. 127/12 (1980) 2657.
[42] N. Komori, S. Sakai, K. Komatsu, in: T. Seiyama, K. Fueki, J. Shiokawa, S. Suzuki (Eds.), Proceedings of the International Meeting on Chemical Sensors, Elsevier, Japan, 1983, p. 57.
[43] R. Lalauze, N.D. Bui, C. Pijolat, in: T. Seiyama, K. Fueki, J. Shiokawa, S. Suzuki (Eds.), Proceedings of the International Meeting on Chemical Sensors, Elsevier, Japan, 1983, p. 47.
[44] M. Riordan, L. Hoddeson, IEEE Spectrum 34/6 (1997) 46.
[45] J.H. Scaff, Metallurgical Transactions 1 (1970) 561.
[46] R.S. Ohl, US Patent No. 2,402,662 (1946).
[47] R.S. Ohl, US Patent No. 2,402,661 (1946).
[48] W.F. Brinkman, D.E. Haggan, W.W. Troutman, IEEE Journal of Solid-State Circuits 32/12 (1997) 1858.
[49] S.O. Kasap, Principles of Electronic Materials and Devices, McGraw-Hill, New York, 2002.
[50] D.A. Neamen, Semiconductor Physics and Devices: Basic Principles, McGraw-Hill, New York, 2003.

[51] R.M. Besancon (Ed.), The Encyclopedia of Physics, Von Nostrand Reinhold Company, New York, 1985.
[52] K. Krane, Modern Physics, John Wiley and Sons, Inc. , New York, 1996.
[53] M.L. Lucia, J.L. Hernandez-Rojas, C. Leon, I. Martil, European Journal of Physics 14 (1993) 86.
[54] Z.I. Alferov (Ed.), Semiconductor Heterostructures: Physical Processes and Applications, MIR Publishers, Moscow, 1989.
[55] R.L. Anderson, Solid-State Electron. 5 (1962) 341.
[56] Y. Nakamura, H. Yoshioka, M. Miyayama, H. Yanagida, T. Tsurutani, Y. Nakamura, J. Electrochem. Soc. 137/3 (1990) 940.
[57] S.-J. Jung, H. Ohsawa, Y. Nakamura, H. Yanagida, K. Hasumi, O. Okada, Electrochemical Society Letters 141/5 (1994) L53.
[58] S.-J. Jung, H. Yanagida, Sensors and Actuators B 37 (1996) 55.
[59] Y. Nakamura, H. Zhuang, A. Kishimoto, O. Okada, H. Yanagida, J. Electrochem. Soc. 145/2 (1998) 632.
[60] R.A. Marra, Y. Nakamura, S. Fujitsu, H. Yanagida, J. Am. Ceram. Soc. 69/7 (1986) C143.
[61] J.H. Yu, G.M. Choi, Sensors and Actuators B 61 (1999) 59.
[62] E. Traversa, J. Am. Ceram. Soc. 78/10 (1995) 2625.
[63] E. Traversa, Sensors and Actuators B 23 (1995) 135.
[64] R. Tongpool, C. Leach, R. Freer, J. Mater. Sci. Lett. 19 (2000) 119.
[65] K.-K. Baek, H.L. Tuller, Sensors and Actuators B 13-14 (1993) 238.
[66] K.-K. Baek, H.L. Tuller, Solid State Ionics 75 (1995) 179.
[67] S. Mridha, D. Basak, Semicond. Sci. Technol. 21 (2006) 928.
[68] J.B. Wachtman, R.A. Haber (Eds.), Ceramic Films and Coatings, Noyes Publications, Park Ridge, 1993.
[69] R.W. Schwartz, Chem. Mater. 9 (1997) 2325.
[70] J.L. Keddie, E.P. Giannelis, J. Am. Ceram. Soc. 74/10 (1991) 2669.

Chapter 4. A Novel Solution Route for the Fabrication of ZnO Thin Films with *c*-axis Orientation

Christopher S. Dandeneau, David P. Cann, and Brady J. Gibbons

Materials Science Program, School of Mechanical, Industrial, and Manufacturing Engineering, Oregon State University, Corvallis, OR 97331,USA

Ram Ravichandran and Thomas K. Plant

School of Electrical Engineering and Computer Science, Oregon State University, Corvallis, OR, 97331, USA

Andriy Zakutayev and Janet Tate

Department of Physics, Oregon State University, Corvallis, OR, 97331, USA

Paper submitted to the *Journal of the American Ceramic Society*

Abstract

Highly *c*-axis oriented ZnO thin films have been fabricated via sol-gel deposition using dimethylformamide-based solutions. Employing zinc acetate as the solute, precursor chemistry was varied with respect to monoethanolamine (MEA) and water content so as to maximize (00*l*) orientation. A solution composition of 5% water and a 1:1 Zn to MEA molar ratio yielded optimum preferred orientation. Through atomic force microscopy this solution was found to produce a uniform microstructure

with an average grain size of 59.2 ± 5.3 nm. A variance of pyrolysis temperature in the range of 200 °C – 400 °C showed maximum (00*l*) preferred orientation to exist at 350 °C. A strong excitonic peak was seen in the absorption spectra, indicating high structural quality. As pyrolysis temperature was raised, film thickness decreased while refractive index increased. These opposing trends were assumed to arise from a density increase, the consequence of a more efficient burnout of solution organics. While the ZnO film pyrolyzed at 350 °C showed highest preferred orientation, electrical resistivity was seen to monotonically decrease with drying temperature, reaching a minimum of 3 Ω-cm at 400 °C. These data indicate that density has a more profound impact on ZnO thin film electrical properties than preferred orientation.

4.1. Introduction

Zinc oxide (ZnO) is a II-VI intrinsic *n*-type semiconductor possessing both a large band gap (~3.3 eV) [1] and a high exciton binding energy (60 meV) [2]. The crystallization of ZnO into the hexagonal wurtzite (P4) structure has led to its exploration as an ideal material for surface acoustic wave (SAW) devices [3], where a maximized piezoelectric constant depends on both a high degree of crystallinity and preferred *c*-axis orientation. The unique nature of the material properties inherent in ZnO has also spurred numerous application-driven studies in such areas as gas detection [4-10], transparent thin film transistors [11, 12] and UV light emitters [13, 14]. As such, the development of optimized, repeatable methods to the fabrication of oriented ZnO thin films is of great benefit to the aforementioned areas of research.

The synthesis of ZnO via chemical solution (sol-gel) deposition is particularly appealing due to the minimal cost of necessary equipment, the low temperatures at which crystallization may take place, and the potential for large area coverage [15]. Sol-gel routes allow for an optimal degree of process control, since desired structural characteristics of the resulting ZnO films may be realized through the introduction of specific additives to the precursor solutions. For ZnO depositions, metal salts are often preferred over metal alkoxides due to their relatively low cost and ease of handling [16, 17]. In addition, precipitation in the solutions can be reduced using metal salt solutes via chelation of the metal ion by organic ligands. In light of these aspects, the research presented here serves to outline a process for the deposition of highly (00*l*) oriented ZnO thin films through an optimized sol-gel route.

The fabrication of ZnO films using the solute zinc acetate dihydrate ($Zn(CH_3COO)_2 \cdot 2H_2O$) has been detailed extensively in the literature [18-21]. Previous studies have employed a wide array of solvents, such as 2-methoxyethanol (MOE) [20, 21], isopropanol [13], and dimethylformamide (DMF) [19] for the dissolution. The choice of an appropriate solvent for this study was dependent on two key factors. First, the solvent must possess a high degree of polarity. This allows for a more efficient dissolution of the polar zinc acetate molecules and thus, yields a more homogeneous precursor solution. Secondly, the boiling point of the solvent must be relatively high. This is crucial during the drying step, where abrupt evaporation of the solvent may initiate cracking or cause the film to exhibit an undesirable degree of random orientation. Of the aforementioned solvents, DMF was chosen due to its highly polar

nature and a boiling point of 152 °C [22] higher than both MOE (125 °C) and isopropanol (82 °C).

While previous studies have employed DMF in the fabrication of ZnO thin films [19], this work is unique in that an optimization of both solution chemistry and pyrolysis temperature has been performed. It will be shown that repeatable, ideal solution chemistries can be obtained through a variance in the content of water and monoethanolamine (MEA), a stabilizer. With the attainment of an optimal solution, the effect of pyrolysis temperature on the preferred orientation of the ZnO was explored. Thin film structure and morphology have been examined through X-ray diffraction (XRD) and atomic force microscopy (AFM), respectively. Optical and electrical characterization data will also be presented. Theories behind the observed results will be discussed.

4.2. Experimental Procedure

Glass slides (VWR International) were used as substrates in this work. A diagram of the sol-gel process is shown in Figure 4.1. Zinc acetate dihydrate (Alfa Aesar, 98.0 - 101.0%) and DMF (Alfa Aesar, 99.8+%) were used as the precursor and solvent, respectively, for all solutions. MEA (Alfa Aesar, 99+%) was added to specific solutions as a stabilizing agent, while DI water was employed for hydrolysis. All solutions were 20 mL with the molarity held constant at 0.6 M. Depositions were performed via spin-coating at 3000 rpm for 30 s using 3 mL syringes fitted with 0.2 μm filters (Fisherbrand). Substrates were cleaned with isopropanol (Mallinckrodt

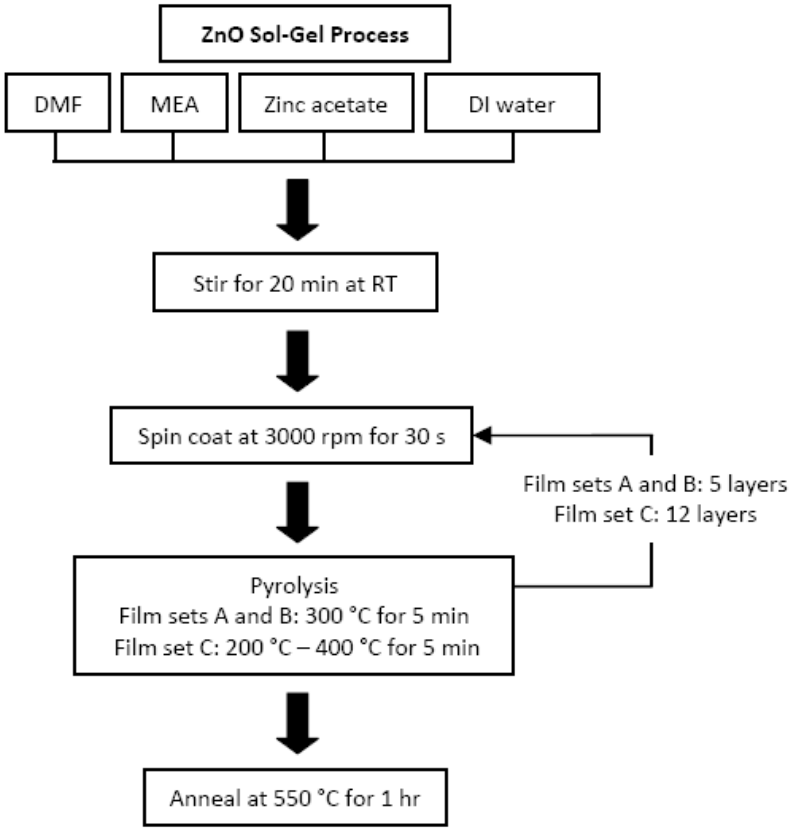

Figure 4.1. Diagram of the sol-gel process used to fabricate the ZnO films

Chemicals, 99.5%) prior to deposition. The films used to explore solution chemistry were comprised of 5 layers. Upon optimization of the precursor solutions, 12 layer films were made to explore the effects of pyrolysis temperature. Pyrolysis was performed on a hot plate while annealing took place in a furnace open to air. Upon completion of the annealing treatment, the films were allowed to cool to room temperature.

To ascertain parameters for maximum preferred orientation, three film sets (Table 4.1) were employed. For set A, the molar ratio of MEA to Zn was held constant

Table 4.1. Film Set Parameters

Film Set A	DMF (mL)	MEA (mL)	Water (mL)	Film Set B	DMF (mL)	MEA (mL)	Water (mL)	Film Set C	Pyrolysis Temp. (°C)
A1	19.28	0.72	0	B1	19	0	1	C1	200
A2	18.28	0.72	1	B2	18	1	1	C2	250
A3	17.28	0.72	2	B3	17	2	1	C3	300
A4	16.28	0.72	3	B4	16	3	1	C4	350
A5	15.28	0.72	4					C5	400

at 1.0 while the concentration of water was varied between 0 – 4 mL in 1 mL increments. Once the ideal water concentration was found, a second film set, B, was made whereby the water content was held constant and the MEA concentration was varied between 0 – 3 mL in 1 mL increments. To examine the effects of pyrolysis temperature, a final film set, C, was made. For these samples, the optimized solution found from film sets A and B was used and the pyrolysis temperature was varied through the range of 200 °C – 400 °C in 50 °C increments.

The structure and overall crystallinity in the films were characterized through θ-2θ and rocking curve (ω) scans using a X-ray diffractometer (Bruker D8 Discover) with Cu K_α radiation. Surface morphology was examined using contact mode atomic force microscopy (AFM: Digital Instruments Nanoscope IIIa). Grain size measurements were calculated using a planimetric procedure outlined by the ASTM [23]. From this, the average grain diameter, *G*, is given by:

$$G = \left[0.0002 \left(N_{ins} + \frac{N_{int}}{2} \right) M^2 \right]^{-\frac{1}{2}} \tag{4.1}$$

where N_{ins} and N_{int} are the number of grains inside and intercepted, respectively, by a circle of known dimensions and M is the magnification used for an attained image. Profilometry measurements (Tencor AlphaStep 500) were used for thin film thickness data.

Optical properties were investigated using a custom-built spectrometer comprised of a double-grating monochromator equipped with a 250 W xenon lamp source (Oriel) and silicon diode detector. Transmission and reflection spectra were measured in the UV-visible spectral range at a 5° beam incidence angle. The absorption coefficient, α, was calculated from:

$$\alpha = 2.303 \frac{\log[(1-R)/T]}{d} \tag{4.2}$$

where T and R are the measured transmission and reflection coefficients, respectively, and d is the film thickness [24]. The effective refractive index (not accounting for surface roughness), n, of the films was measured in the visible region using a Filmetrix spectrometer. All values quoted here are at 633 nm. Electrical resistivity of the films was measured via the van der Pauw technique (Lakeshore 7504). Since resistivity is proportional to thin film thickness, the additional film layers of set C serve to maximize electrical response. Previous research has shown that ambient oxygen can be adsorbed on the ZnO surface, significantly degrading electrical properties [25]. Subsequent desorption of the oxygen was found to occur under the influence of UV radiation. As such, all electrical measurements were performed under constant UV light supplied by a low pressure mercury (Hg) lamp.

4.3. Results and Discussion

4.3.1. Water optimization

As stated above, ZnO crystallizes into the hexagonal wurtzite structure. When this structure is highly oriented with the *c*-axis perpendicular to the substrate plane, a strong (002) peak intensity is seen in the XRD pattern at a 2θ value of 34.4°. This is typically accompanied by a less intense (004) diffraction peak at $2\theta = 72.6$. As an especially high degree of preferred orientation is reached, these (00*l*) peaks dominate the diffraction pattern. All other peaks, including the (101) reflection known to be of highest intensity in polycrystalline ZnO, effectively vanish. The preferred orientation inherent in ZnO thin films, even if grown on amorphous substrates, is the result of a minimization of surface free energy and is known as self-texturing [26, 27]. During thin film growth the high surface to volume ratio drives the system to expose planes of low surface energy density. In the case of ZnO the (002) plane possesses a minimum of this property [17] and as such, preferred (00*l*) orientation ensues provided that enough thermal energy for atomic mobility is present.

Shown in Figure 4.2 are the θ-2θ and rocking curve scans for film set A. These films were made with a fixed 1:1 molar ratio of MEA to Zn while the water concentration was varied. An analysis of Figure 4.2(a) shows the presence of strong (00*l*) preferred orientation that persists up to a water concentration of 3 mL. It is at this 3 mL water concentration that the precursor solutions began to exhibit turbidity indicative of uncontrolled hydrolysis and precipitation. Film A5, made with a 4 mL

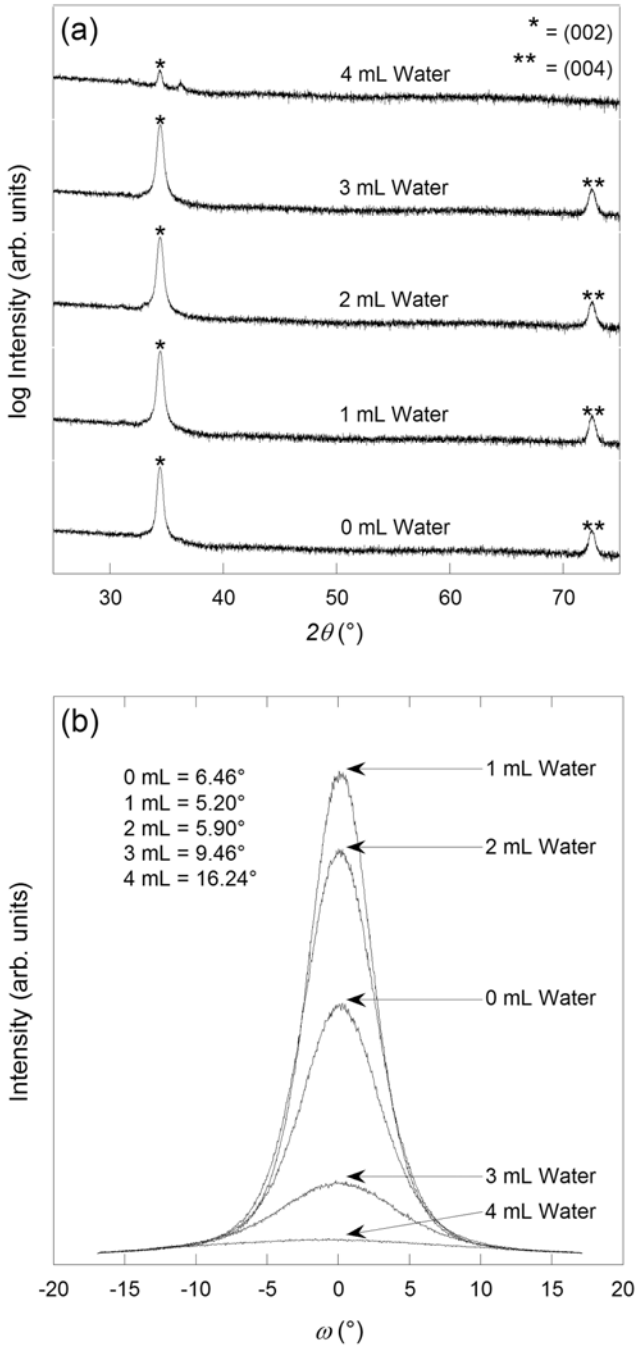

Figure 4.2. XRD data taken on film set A. The θ-2θ scans in (a) show strong (00*l*) orientation up to a 3 mL water concentration. Rocking curve scans of the (002) peak (b) show that film A2 (1 mL water) possesses a minimum in the FWHM value.

water solution, showed very minimal preferred orientation. While the A4 and A5 solutions showed evidence of precipitation, these precursors were still able to pass through the 0.2 μm filters used for film deposition. Of the films comprising set A, film A2, with 1 mL water concentration was found to yield the greatest (002) peak intensity. Rocking curve full-width at half-maximum (FWHM) data of film set A, shown in Figure 4.2(b), confirm film A2 possesses the highest degree of (00*l*) preferred orientation.

The drawing of definitive conclusions from the XRD patterns is difficult due to complex nature of the sol-gel process. However, previous research allows for the development of possible scenarios to explain the observed trends. The use of MEA in the sol-gel fabrication of ZnO thin films is driven by its actions as a both a chelating and bridging agent [28]. These two possible coordination modes allow for the prevention of uncontrolled solute hydrolysis and lead to a more homogeneous precursor solution. In solutions involving water, MEA, and zinc acetate, a competition to bind with the Zn^{2+} cation ensues between the OH^{-}, MEA, and CH_3COO^{-} ligands [29]. In an ideal solution, the zinc cation is effectively chelated by either the MEA or acetate ions and hydrolysis is inhibited until the film is deposited. The existence of an optimal concentration of water (and thus OH^{-} ions) ensures that full hydrolysis and condensation will be achieved upon spin coating. Since the solute used in this study is a dihydrate, hydrolysis reactions proceed in solutions where no excess water is added. However, the zinc acetate is not as efficiently and fully hydrolyzed than in solutions where additional water is introduced. As such, for a given pyrolysis and annealing scenario, films made by solutions with added water concentrations attain a higher level

of crystallinity and subsequent preferred orientation. When the optimal concentration of water in a solution is exceeded, uncontrolled hydrolysis and precipitation occurs which results in a loss of solution homogeneity. This yields a more inhomogeneous gel and thus a thin film which possesses a greatly diminished degree of crystallinity. As film A2 showed both the highest (002) peak intensity and lowest (002) FWHM, this water concentration was used in the precursor solutions for set B.

AFM scans of films A2 and A5 are shown in Figure 4.3. The average grain size of A2 from multiple scans was determined to be 59.2 ± 5.3 nm. It appears that the water concentration did not significantly affect mean grain size, as the average grain diameter of film A5 was found to be 58.9 ± 1.1 nm. However, visual inspection of the AFM images shows film A5 to possess a more bimodal microstructure. It appears that in films with an optimal concentration of water, there exists a high degree of grain size uniformity throughout the microstructure. However, at undesirably high water contents, the scenario of uncontrolled hydrolysis leads to a more inhomogenous microstructure consisting of both larger and smaller grains. That is, nucleation may be occurring at precipitates within the gel in addition to the gel/substrate interface. This could lead to the development of a more inhomogeneous microstructure such as observed here.

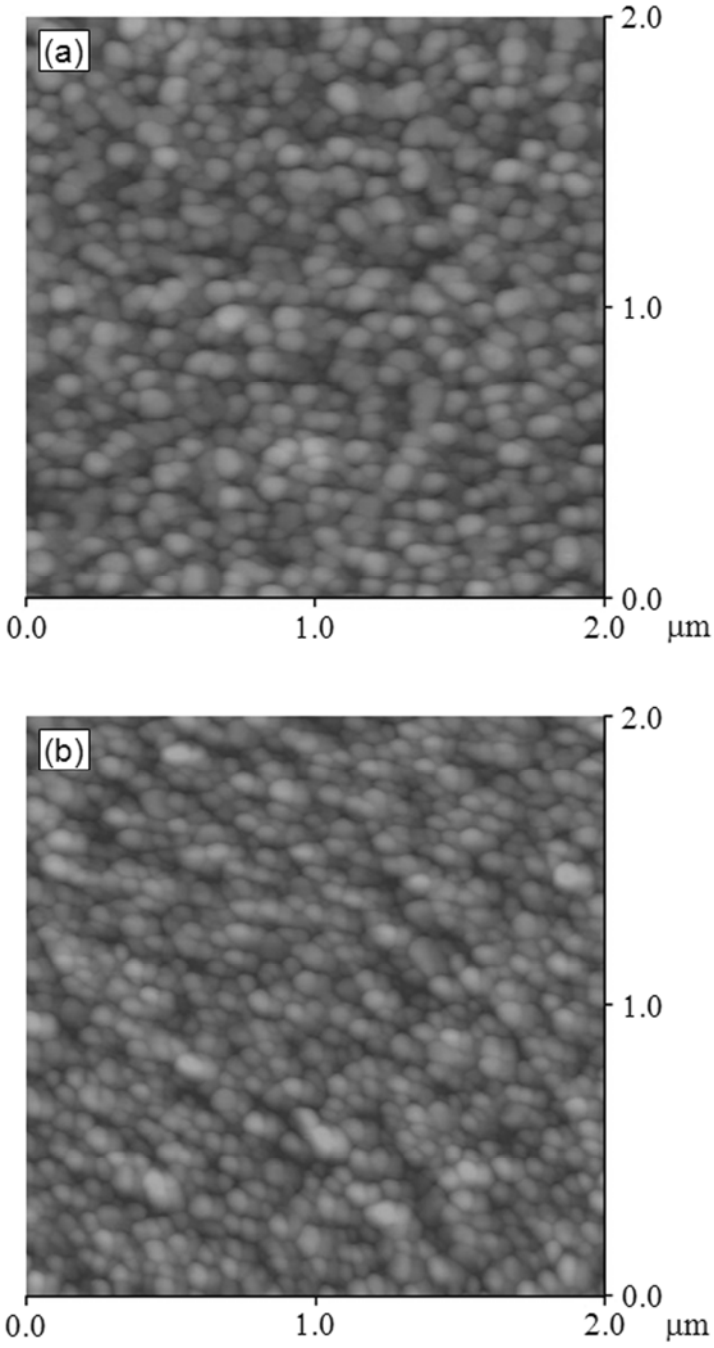

Figure 4.3. AFM images of films A2 (a) and A5 (b) from solutions with 1 mL and 4 mL of water content, respectively. While the mean grain size does not vary significantly, film A2 appears to possess a more uniform homogeneous microstructure.

4.3.2. MEA optimization

With an optimal water concentration of 1 mL found from film set A, this parameter was held constant and the MEA content was varied so as to monitor the effect on preferred orientation. The results of the XRD scans are shown in Figure 4.4. It appears that the content of MEA in the precursor solutions has a more profound impact on preferred orientation than that of water addition. Maximum (002) peak intensity for film set B is seen to occur in sample B2, with a 1 mL concentration of MEA. The rocking curve scans for film set B were then compared with film A2. Recall that this film also had a 1 mL water concentration. As seen in Figure 4.4(b), film A2, with both 1 mL of additional water and a 1:1 molar ratio of MEA to Zn exhibited the lowest FWHM value in ω of all the films used to explore solution optimization. This film also possessed the greatest (002) peak intensity in the θ-2θ scans. As such, optimal solution chemistry was concluded to exist at 0.72 mL of MEA and 1 mL of water. The trends seen in the XRD data may be explained by the ability of MEA to coordinate the Zn^{2+} cations. When an ideal amount of MEA is present, the zinc atoms are effectively chelated by both the MEA and the acetate ions so as to prevent uncontrolled hydrolysis as discussed above. Condensation reactions between an OH^{-} group and a hydrolyzed Zn-MEA or Zn-CH_3COO complex lead to the formation of small ZnO colloids [29]. With adequate heat treatment, the confluence of these ZnO particles ultimately results in a homogeneous ZnO thin film. The presence of an optimal amount of MEA ensures this scenario proceeds in a controlled manner.

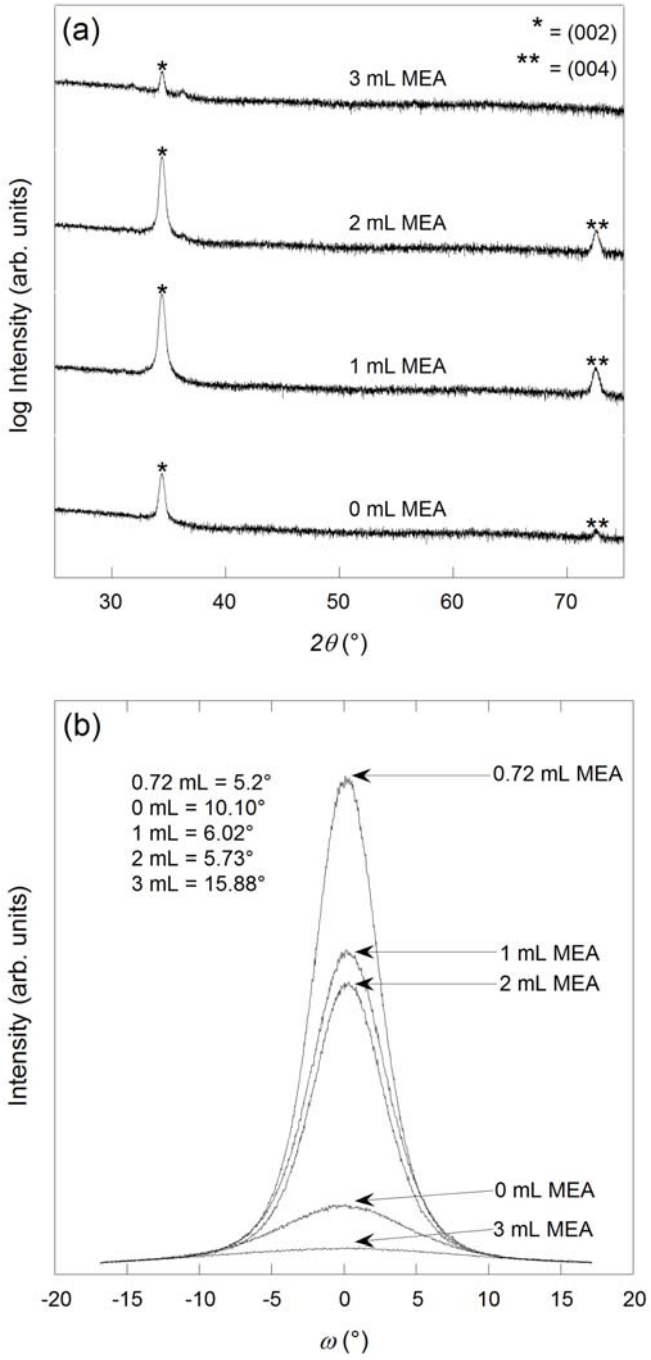

Figure 4.4. XRD scans showing the effect of MEA addition on preferred orientation. The rocking curve scans in (b) include film A2 (0.72 mL MEA). Optimum *c*-axis orientation is attained at a 1:1 molar ratio of MEA to Zn.

In studies done by Sagar *et al*. [30], a 1:1 ratio of MEA to zinc acetate was found to yield optimal preferred orientation in 0.6 M solutions involving methanol, MEA, and zinc acetate. The researchers attributed this improvement to the increased pH of the sols due to addition of MEA.

AFM images of films B2 and B4 are shown in Figure 4.5. The average grain size of film B2 was found to be 63.4 ± 9.5 nm, whereas this same parameter in B4 was found to be 55.5 ± 1.8 nm. While the mean grain size does not vary significantly, there is an apparent difference in grain size distribution. Film B2 appears to possess a much more uniform grain size whereas the grain size distribution of film B4 is more bimodal in character. This may be attributed to an undesirably high viscosity level that exists in solution B4 due to the increased MEA content. As stated above, the purpose of MEA addition is to effectively complex the zinc cations in solution. Any excess MEA content serves to increase solution viscosity, resulting in poor substrate wetting during the spin-coating step. This is turn leads to an inhomogeneous precursor film and, upon pyrolysis, results in the bimodal microstructure seen in Figure 4.5(b).

4.3.3. Pyrolysis optimization

With the solution chemistry optimized at 1 mL of water and a 1:1 molar ratio of MEA to zinc, the impact of pyrolysis temperature was explored for film set C. For these samples, 12 film layers were employed with the pyrolysis temperature varying from 200 °C to 400 °C in 50 °C increments. The XRD data for these samples is shown in Figure 4.6. Shown in Figure 4.6(b) are the respective ratios of (002) to (101) peak

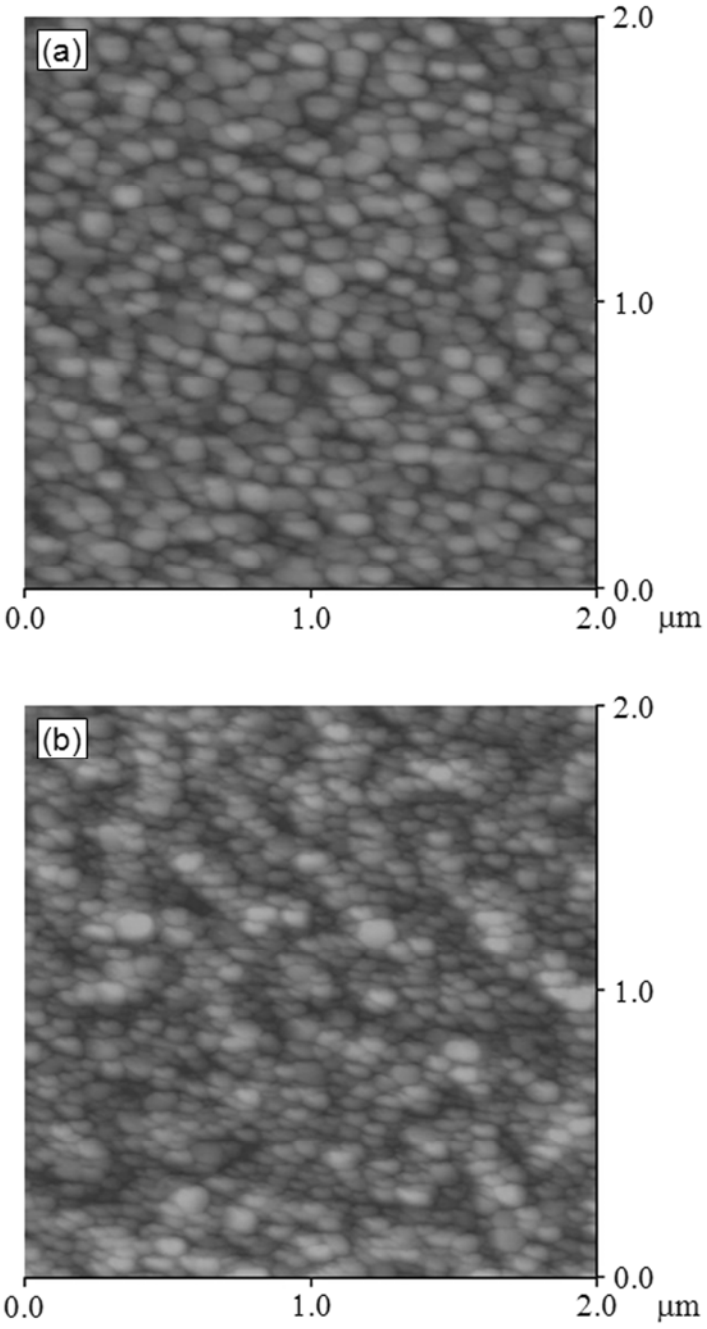

Figure 4.5. AFM images of films B2 (a) and B4 (b) from solutions with 1 mL and 3 mL of MEA, respectively. The increased MEA content of solution B4 results in more bimodal microstructure when compared to the morphology of film B2.

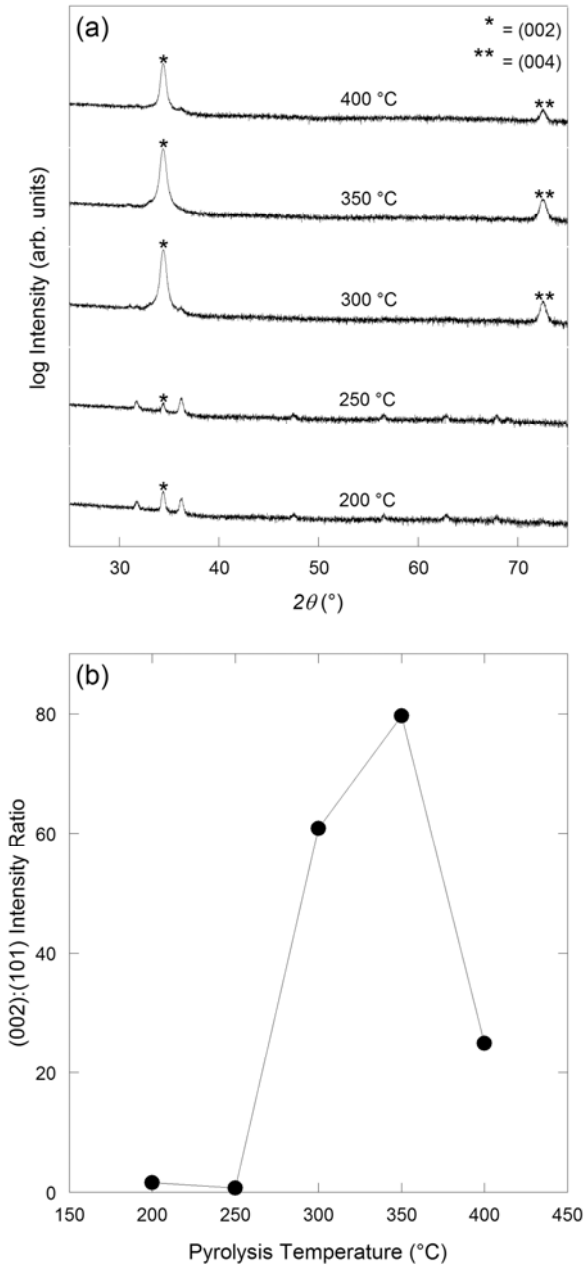

Figure 4.6. The XRD data from film set C. Optimal (00*l*) preferred orientation is seen in film C4 at a pyrolysis temperature of 350 °C. A maximum in the (002):(101) peak intensity ratio (b) is also seen at this temperature. A line has been added to guide the eye.

intensity for each film of set C. Maximum preferred orientation is exhibited in film C4 at a pyrolysis temperature of 350 °C. At undesirably low pyrolysis temperatures, insufficient thermal energy is imparted into the system. This scenario prevents the atomic motion necessary in the formation of a highly *c*-axis oriented structure. One of the advantages of a high boiling point solvent such as DMF is its continued presence at higher pyrolysis temperatures. This allows for a more complete rearrangement of the initial gel phase prior to a final annealing treatment [31]. In combination with MEA, the end result is a more fully crystallized and oriented thin film. If the pyrolysis temperature is undesirably high, abrupt solvent and organic evaporation may occur. This prevents the initial rearrangement and structural relaxation of the gel phase to take place in a controlled manner [28]. Once again, the outcome is a thin film possessing a more randomly oriented structure.

Shown in Figure 4.7 are AFM scans of film C1 and C4. The average grain size of film C1 was found to be 79.1 ± 3.4 nm whereas in C4 the average grain diameter was 83.0 ± 2.4 nm. The morphology of film C4 in Figure 4.7(b) is comprised of grains that are more faceted in nature than that of film C1 in Figure 4.7(a). This is indicative of well-oriented hexagonal grains with the *c*-axis perpendicular to the substrate plane.

The optical transmission spectrum of film C4 is shown in Figure 4.8. This film was found to be highly transparent (78-91%) in the visible regime with a sharp fundamental absorption edge close to 370 nm. The inset of Figure 4.8 is a plot of the absorption coefficient, α, versus the photon energy. The sharp peak present at 3.38 eV

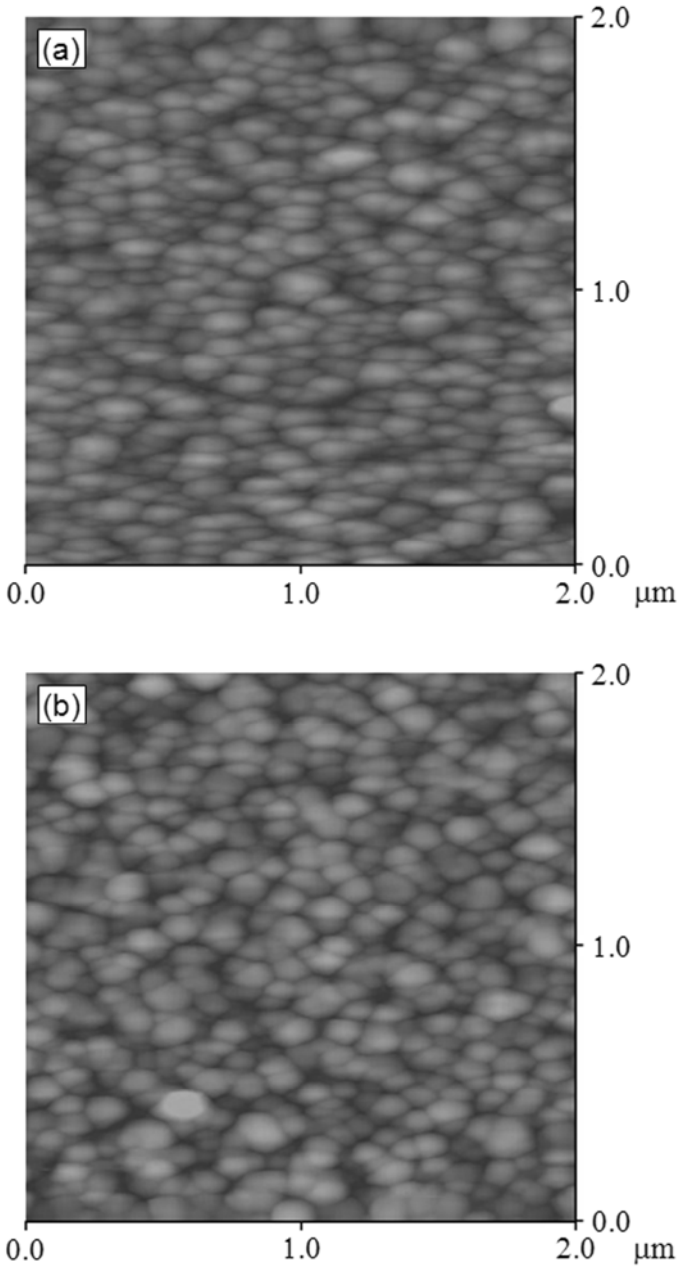

Figure 4.7. AFM images of films C1 (a) and C4 (b), pyrolyzed at 200 °C and 350 °C, respectively. The grains of film C4 possess a more faceted shape indicative of a *c*-axis oriented wurtzite structure.

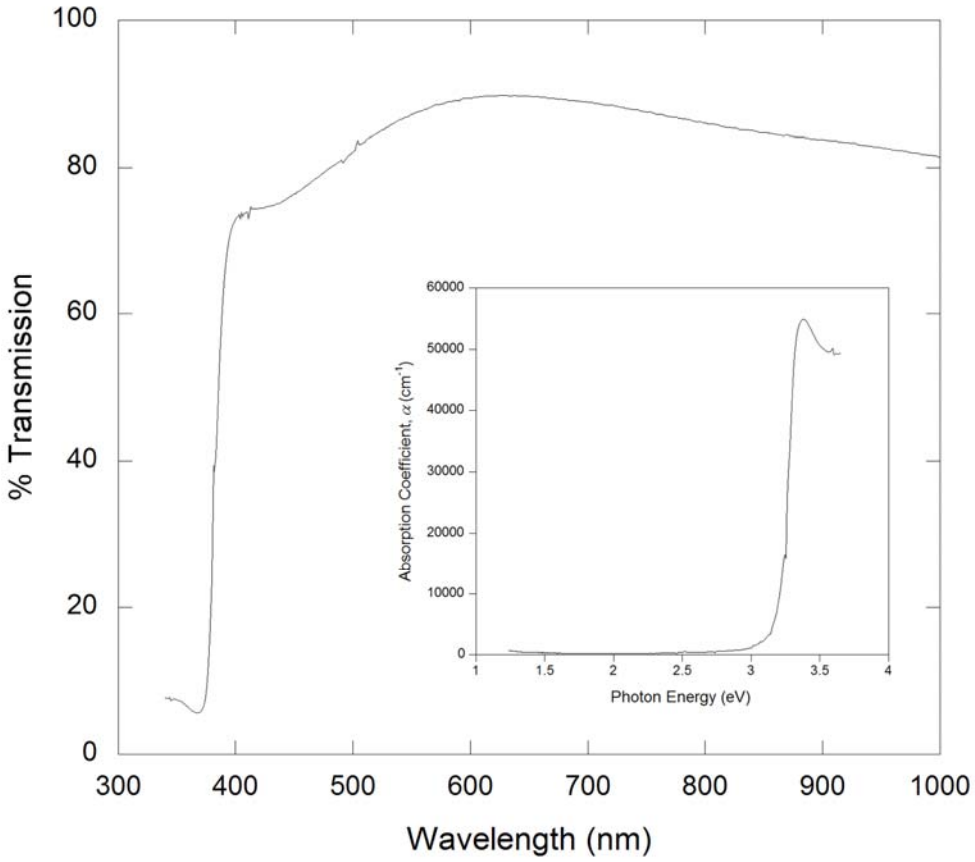

Figure 4.8. Optical transmission data of an optimized film pyrolyzed at 350 °C. The sharp excitonic peak present in the absorption spectra (inset) is an indicator of high structural quality.

can be attributed to absorption by free excitons. The presence of this excitonic peak is indicative of a high degree of structural quality [32].

Shown in Figure 4.9(a) is the effect of pyrolysis temperature on the film thickness and refractive index of film set C. As the pyrolysis temperature was raised,

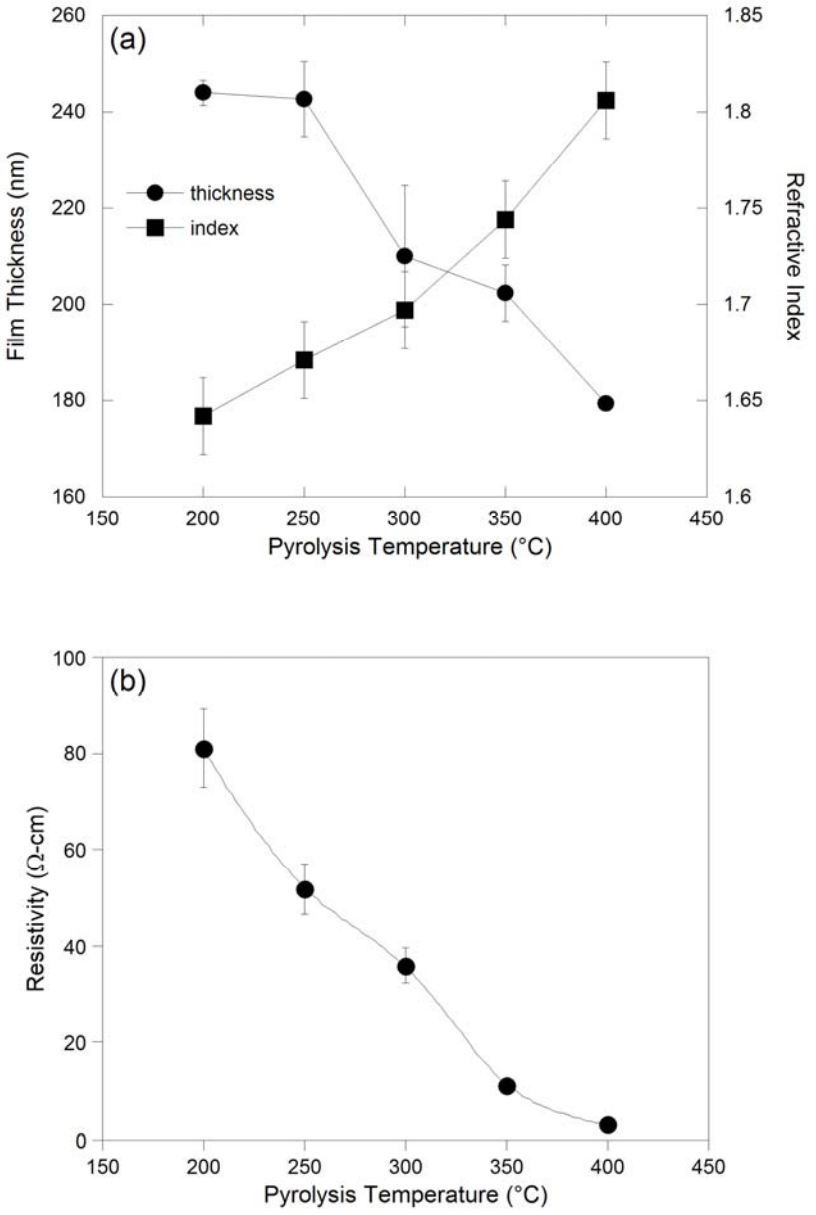

Figure 4.9. The opposing trends in film thickness and refractive index with respect to pyrolysis temperature are shown in (a). In (b), the electrical resistivity is seen to monotonically decrease as the pyrolysis temperature is increased.

thickness was found to decrease from 244 ± 2.6 nm (film C1) to 179.3 ± 1.5 nm (film C5). This trend was accompanied by a corresponding increase in the effective refractive index, *n*, from 1.64 (film C1) to 1.8 (film C5). An analysis of these trends suggests that the films are becoming denser as the pyrolysis temperature is increased. As stated earlier, undesirably high pyrolysis temperatures can be detrimental to preferred orientation due to the occurrence of abrupt organic evaporation. However, it is this organic vaporization at higher pyrolysis temperatures that leads to a denser ZnO film. A delicate balance exists between preferred orientation and thin film density optimization. The peak effective refractive index of 1.75 found for film C5 is higher than that reported for chemically derived films in a previous study ($n = 1.5$) [33]. However, all measured effective refractive indices in this study were lower than values reported for single crystal ZnO ($n = 2.02$) [34], and ZnO films prepared by PLD ($n = 1.95$) [35] or sputtering ($n = 1.9$) [36]. Not accounting for surface roughness certainly lowers the effective refractive index, however density optimization for these chemically derived films still must occur.

A plot of the electrical resistivity versus pyrolysis temperature is shown in Figure 4.9(b). An increase in the pyrolysis temperature resulted in a monotonic decrease in electrical resistivity by more than an order of magnitude, from 81 Ω-cm (film C1) to 3 Ω-cm (film C5). These values compare well with previous studies on undoped ZnO films, where resistivity was seen to range from ~1 Ω-cm [18] to 28.2 Ω-cm [24] for 300 nm and 190 nm thick films, respectively. It has been stated that a high degree of preferred orientation leads to a lower resistivity due to both a reduction in scattering events at grain boundaries and the shorter charge carrier path length

encountered by electrons traveling in the *c*-plane [37, 38]. This may be true if thin film density is held relatively constant. However, the density differences discussed above suggest that the electrical transport characteristics of ZnO thin films may be defined more by density than preferred orientation. This would be consistent with previous studies on ZnO and aluminum-doped ZnO films where the authors attributed resistivity variances to the possible effects of differing annealing procedures and not preferred orientation [39].

4.4. Conclusions

The work presented here serves to outline an optimized DMF-MEA-based sol-gel process in the fabrication of highly *c*-axis oriented ZnO thin films. Employing zinc acetate as the solute, solution chemistry was varied with respect to water and MEA concentration so as to maximize (002) preferred orientation. A solution composition of 5% water (by volume) and a 1:1 molar ratio of Zn to MEA yielded optimum preferred orientation. With solution chemistry optimized, the process parameter of pyrolysis was explored. Maximum preferred orientation was seen to exist at a drying temperature of 350 °C. Undesirably low or high pyrolysis temperatures yielded films with more random orientations. AFM imaging was performed to ascertain average grain size and film morphology. While a variance in either MEA or water content did not significantly affect grain size, high MEA or water content appeared to induce more bimodal microstructures. The film with optimum preferred orientation had an average grain size of 83.0 ± 2.4 nm. The optical transmission spectrum of this film showed a

fundamental absorption edge around 370 nm. Absorption coefficient measurements revealed the presence of a sharp excitonic peak at 3.38 eV, an indicator of high structural quality.

The effect of pyrolysis temperature on film thickness, resistivity, and refractive index was examined. By increasing the pyrolysis temperature from 200 °C to 400 °C, film thickness was seen to decrease, while refractive index was found to increase. These trends were likely indicative of an increase in thin film density, whereby higher pyrolysis temperatures were more efficient at evaporating solution organics. Van der Pauw measurements showed electrical resistivity to monotonically decrease as the pyrolysis temperature was raised, an indication that density is more critical factor on thin film electrical properties than preferred orientation.

Acknowledgements

The authors would like to thank Professor Michael Lerner in the Department of Chemistry at Oregon State University for fruitful discussions on the topic of sol-gel science and Professor John Simonsen for assistance in film characterization. Funding from the Army Research Laboratory and the Oregon Nanoscience and Microtechnologies Institute is gratefully acknowledged.

References

[1] H.L. Hartnagel, A.L. Dawar, A.K. Jain, C. Jagadish, Semiconducting Transparent Thin Films, Institute of Physics, New York, 1995.
[2] U. Ozgur, Y.I. Alivov, C. Liu, A. Teke, M.A. Reshchikov, S. Dogan, V. Avrutin, S.-J. Cho, H. Morkoc, J. Appl. Phys. 98 (2005) 041301.
[3] C.R. Gorla, N.W. Emanetoglu, S. Liang, W.E. Mayo, Y. Lu, M. Wrabeck, H. Shen, J. Appl. Phys. 85/5 (1999) 2595.
[4] S. Aygun, D. Cann, J. Phys. Chem. B 109 (2005) 7878.
[5] K.-K. Baek, H.L. Tuller, Sensors and Actuators B 13-14 (1993) 238.
[6] S. Mridha, D. Basak, Semicond. Sci. Technol. 21 (2006) 928.
[7] S. Aygun, D. Cann, Sensors and Actuators B 106 (2005) 837.
[8] S. Kwon, S. Aygun, D.P. Cann, Sensor Letters 3/3 (2005) 1.
[9] K.-K. Baek, H.L. Tuller, Solid State Ionics 75 (1995) 179.
[10] M. Suchea, S. Christoulakis, K. Moschovis, N. Katsarakis, G. Kiriakidis, Thin Solid Films 515 (2006) 551.
[11] S. Masuda, K. Kitamura, Y. Okumura, S. Miyatake, H. Tabata, T. Kawai, J. Appl. Phys. 93/3 (2003) 1624.
[12] R.L. Hoffman, B.J. Norris, J.F. Wager, Appl. Phys. Lett. 82/5 (2003) 733.
[13] D. Basak, G. Amin, B. Mallik, G.K. Paul, S.K. Sen, J. Cryst. Growth 256 (2003) 73.
[14] M. Kawasaki, A. Ohtomo, I. Ohkubo, H. Koinuma, Z.K. Tang, Y. P., G.K.L. Wong, B.P. Zhang, Y. Segawa, Mater. Sci. Eng., B 56 (1998) 239.
[15] G. Yi, M. Sayer, Ceramic Bulletin 70 (1991) 1173.
[16] H. Kozuka (Ed.), Sol-Gel Processing, Springer, New York, 2005.
[17] N. Bel Hadj Tahar, R. Bel Hadj Tahar, A. Ben Salah, A. Savall, J. Am. Ceram. Soc. 91/3 (2008) 846.
[18] D. Bao, H. Gu, A. Kuang, Thin Solid Films 312 (1998) 37.
[19] N.R.S. Farley, C.R. Staddon, L. Zhao, K.W. Edmonds, B.L. Gallagher, D.H. Gregory, J. Mater. Chem. 14 (2004) 1087.
[20] Y. Kokubun, H. Kimura, S. Nakagomi, Jpn. J. Appl. Phys., Part 1 42 (2003) L904.
[21] M. Ohyama, H. Kozuka, T. Yoko, Thin Solid Films 306 (1997) 78.
[22] C.J. Brinker, G.W. Scherer, Sol-Gel Science: The Physics and Chemistry of Sol-Gel Processing, Academic Press, Inc., New York, 1990.
[23] ASTM, Annual Book of ASTM Standards 03.01 (2005).
[24] Y. Natsume, H. Sakata, Thin Solid Films 372 (2000) 30.
[25] D.H. Zhang, D.E. Brodie, Thin Solid Films 261 (1995) 334.
[26] X. Jiang, C.L. Jia, R.J. Hong, J. Cryst. Growth 289 (2006) 464.
[27] S. Goto, N. Fujimura, T. Nishihara, T. Ito, J. Cryst. Growth 115 (1991) 816.
[28] M. Ohyama, H. Kozuka, T. Yoko, S. Sakka, J. Ceram. Soc. Jpn. 104/4 (1996) 296.

[29] L. Znaidi, G.J.A.A. Soler Illia, S. Benyahia, C. Sanchez, A.V. Kanaev, Thin Solid Films 428 (2003) 257.
[30] P. Sagar, P.K. Shishodia, R.M. Mehra, Appl. Surf. Sci. 253 (2007) 5419.
[31] L. Znaidi, G.J.A.A. Soler Illia, R. Le Guennic, C. Sanchez, A.V. Kanaev, J. Sol-Gel Sci. Technol. 26 (2003) 817.
[32] J.F. Muth, R.M. Kolbas, A.K. Sharma, S. Oktyabrsky, J. Narayan, J. Appl. Phys. 85/11 (1999) 7884.
[33] S. Bandyopadhyay, G.K. Paul, S.K. Sen, Sol. Energy Mater. Sol. Cells 71 (2002) 103.
[34] V. Srikant, D.R. Clarke, J. Appl. Phys. 83/10 (1998) 5447.
[35] F.K. Shan, Y.S. Yu, Thin Solid Films 435/174-178 (2003).
[36] S.J. Kang, Y.H. Joung, Appl. Surf. Sci. 253 (2007) 7330.
[37] V. Musat, B. Teixeira, E. Fortunato, R.C.C. Monteiro, P. Vilarinho, Surf. Coat. Technol. 180-181 (2004) 659.
[38] Z.Q. Xu, H. Deng, Y. Li, Q.H. Guo, Y.R. Li, Mater. Res. Bull. 41 (2006) 354.
[39] R. Bel Hadj Tahar, N. Bel Hadj Tahar, J. Am. Ceram. Soc. 88/7 (2005) 1725.

Chapter 5. Thin film Chemical Sensors Based on *p*-CuO/*n*-ZnO Heterocontacts

Christopher S. Dandeneau, Yu-Hong Jeon, Christopher T. Shelton, David P. Cann, and Brady J. Gibbons

Materials Science Program, School of Mechanical, Industrial, and Manufacturing Engineering, Oregon State University, Corvallis, OR, 97331, USA

Thomas K. Plant

School of Electrical Engineering and Computer Science, Oregon State University, Corvallis, OR, 97331, USA

Paper submitted to *Thin Solid Films*

Abstract

Previous work on bulk ceramic heterocontacts (*n*-ZnO/*p*-CuO) has indicated significant sensitivity to the presence of specific adsorbed chemical species. Here, these results are extended to thin film heterostructures fabricated via chemical solution methods. It is expected that thin film sensor architectures will possess significant advantages over their bulk counterparts. In this study, the desired properties of porosity and crystallinity have been optimized with respect to pyrolysis temperature for each ZnO and CuO sol-gel process. The results of microscopy and x-ray diffraction (XRD) indicated that an optimal balance of these two properties is

achieved at a pyrolysis temperature of 250 °C. The CuO films were seen to possess a level of porosity significantly higher than that seen in the ZnO films, making them an ideal candidate for the top layer in a planar thin film heterostructure. Results of current-voltage measurements conducted in 4000 ppm hydrogen have confirmed that the inherent porosity of the CuO films led to an enhanced sensor response in CuO on ZnO heterostructures. Lastly, the fabrication and structural characterization of a mixed solution type heterostructure has been detailed. Atomic force microscopy and XRD data indicated the presence of ZnO pillars dispersed among a matrix of CuO.

5.1 Introduction

One of the most pressing needs in sensor technology is the availability of an inexpensive, robust, and reliable sensor that is able to detect and quantify the presence of a specific gas (the analyte) among common interferents. This lack of selectivity is an inherent limitation in most sensor designs and often necessitates the use of catalytic surface treatments (for preferential analyte diffusion), strict temperature control, or pre-filtering of the gas stream. The research presented here aims to address these issues through the fabrication of planar thin film heterostructures possessing instrinsic selectivity characteristics. The work of Yanagida [1] has shown that bulk *p*-CuO/*n*-ZnO heterocontact sensors possess inherent selectivity properties.

Zinc oxide (ZnO) is a II-VI intrinsic *n*-type semiconductor possessing both a large band gap (3.3 eV) [2] and a high exciton binding energy (60 meV) [3]. The presence of electrons as the majority charge carriers in ZnO arises from an innate

deficiency in oxygen traced to the presence of either zinc interstitials or oxygen vacancies [4]. Copper oxide (CuO), due to an excess of oxygen, is a *p*-type semiconductor with a band gap of ≈ 1.4 eV [5]. The difference in charge carrier along with the immisciblity of these two materials has spurred the creation of novel device designs in the arena of gas detection.

Previous work on bulk *p*-CuO/*n*-ZnO heterocontacts has shown the electrical properties of the structural interface to be extremely sensitive to the presence of adsorbed gas [6-8]. The functionality of these devices is based on reactions that occur between a chemical species and charge carriers at the heterocontact interface. The governing reactions for a *p*-CuO/*n*-ZnO heterocontact in the detection of H_2 are shown below. Reactions between adsorbed oxygen on the *n*-ZnO (5.1) and H_2 on the *p*-CuO (5.2) lead to the evolution of water and a subsequent reduction in the potential barrier to charge migration across the interface. This reduction is quantified through appropriate dc current-voltage (*I*-*V*) testing. While this structure is sensitive to any reducing gas, selectivity, as shown in previous studies, can be achieved through varying the applied bias or measuring frequency [1, 9].

$$[n\text{-ZnO}]: O_2 + 2e^- \rightarrow 2O^- \tag{5.1}$$

$$[p\text{-CuO}]: 2H_2 + 4h^+ \rightarrow 4H^+ \tag{5.2}$$

$$[\text{interface}]: 4H^+ + 2O^- \rightarrow 2H_2O \tag{5.3}$$

While bulk heterocontacts have shown desirable selectivity and sensitivity characteristics, the detection capabilities of these structures suffer from a few innate drawbacks. First, the analyte must traverse a large, circuitous diffusion path to reach

the heterocontact interface. Second, the connectivity, or contact area, between the *p*-CuO and *n*-ZnO is low, which minimizes the effective interfacial area of the device. To overcome these issues, planar thin film heterostructures have been fabricated through chemical solution deposition (sol-gel) techniques. The sol-gel process affords the ability to manipulate the microstructures of deposited films through the adjustment of specific process parameters. Of key interest in this study are the properties of porosity and crystallinity, both of which are proposed to enhance sensor response. A high degree of porosity (along with the inherently reduced dimensions of the thin films) allows for fast diffusion of the analyte to the heterostructure interface, while the attainment of long range order results in increased charge mobility, and thus faster response times. While there exists previous work on planar thin film gas sensors [10, 11], this study is unique in that the optimization of porosity and crystallinity in the component oxide films has been emphasized. It will be shown that adequate control has been demonstrated over the aforementioned thin film properties so as to proceed with the incorporation of each film into a *pn*-heterostructure. These heterostructures have been fabricated and the optimized film properties, especially the porosity, are seen to have a pronounced effect on the gas sensing characteristics of the structure. Lastly, the fabrication and initial characterization of a heterostructure formed via mixed solution sol-gel chemistry will be detailed.

5.2. Experimental Detail

The substrates used for this study were <100> silicon supplied by Sumco Corp. (USA). The sol-gel procedure for fabricating the ZnO films is shown in Figure 5.1. For this process, zinc acetate dihydrate, $Zn(CH_3COO)_2 \cdot 2H_2O$ (Alfa Aesar, 98.0 – 101.0%) and 2-methoxyethanol (MOE: Alfa Aesar, 99%) were used as the solute and solvent, respectively. Monoethanolamine (MEA : Alfa Aesar, 99+%) was added as a stabilizing agent, with the molar ratio of zinc acetate to MEA kept constant at 1.0; the solution was 0.6 M. This process is similar to previous studies performed on ZnO [12]. In maximizing the porosity and crystallinity of the ZnO films, attention was focused

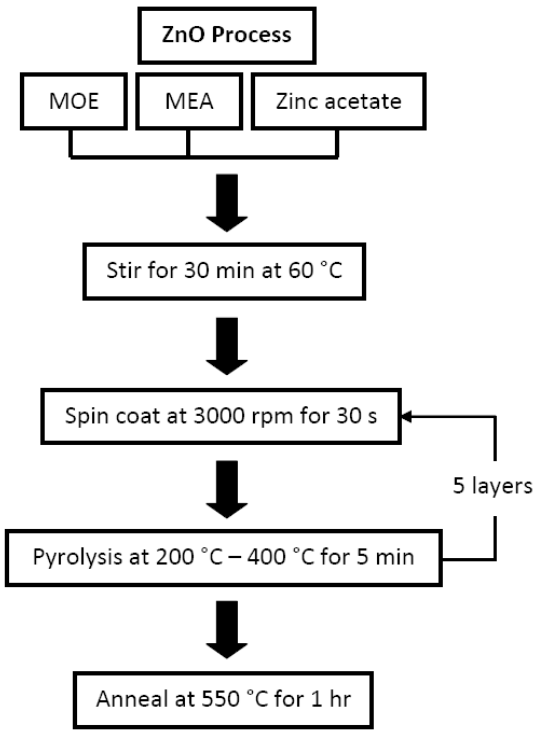

Figure 5.1. The sol-gel process used for fabricating the ZnO films.

on the pyrolysis step for reasons to be discussed in the next section. As such, all process parameters were held constant with the exception of pyrolysis temperature so as to examine its effects on porosity and crystallinity. Pyrolysis was performed in the temperature range of 200 °C – 400 °C in 50 °C increments for 5 minutes/layer. The per-layer thickness of the ZnO films, as measured through profilometry (Tencor AlphaStep 500), was approximately 30 nm.

For the CuO depositions, a technique modeled after studies done by Oral *et al*. was used [13]. A diagram of this procedure is shown in Figure 5.2. This process involves the dissolution of copper (II) acetate monohydrate, $Cu(CH_3COO)_2 \cdot H_2O$ (Alfa

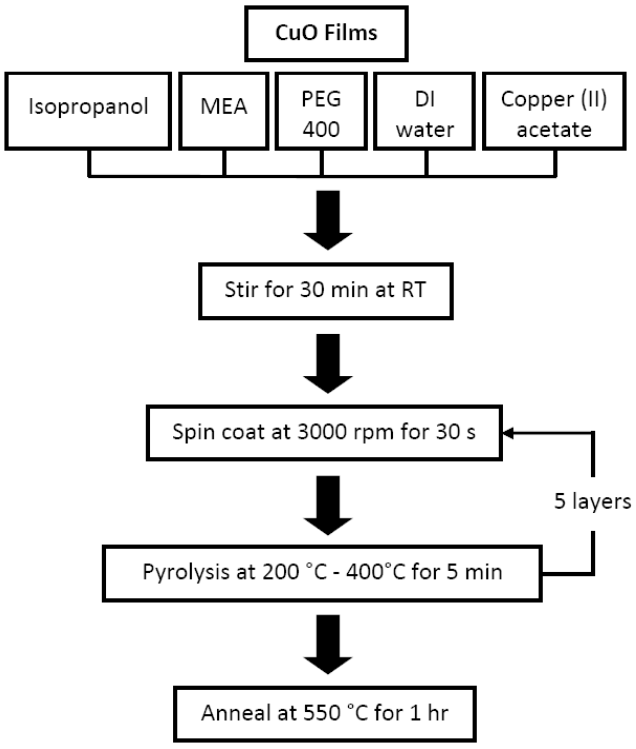

Figure 5.2. A diagram of the CuO sol-gel process used in this study.

Aesar 98.0 – 102.0%) in isopropanol (Mallinckrodt, 99.5%). MEA was also added as a stabilizer and polyethylene glycol (PEG-400: Alfa Aesar) was used so as to optimize solution viscosity. De-ionized (DI) water was introduced into the CuO solutions to facilitate hydrolysis. MEA and PEG-400 content was held constant at a concentration of 5% by volume, while DI water was used at a 2% by volume concentration. The molarity of the solution was kept constant at 0.25 M. As will be made clear, optimization of the CuO films was focused on an examination of the effect of pyrolysis temperature on the crystallinity of the films. Pyrolysis parameters were identical to the ZnO process. The per-layer thickness of the CuO films was found to be approximately 20 nm.

All depositions were performed via spin-coating using 3 mL syringes fitted with 0.2 μm filters (Fisherbrand). Substrates were cleaned with isopropanol prior to deposition. Each oxide film was comprised of 5 layers, spun at 3000 rpm for 30 s. Pyrolysis occurred on a hot plate, while annealing took place at 550 °C in a furnace open to air after which the films were allowed to cool to room temperature. Following the optimization of each ZnO and CuO process, two types of heterostructures were made; ZnO on CuO (ZnO/CuO) and CuO on ZnO (CuO/ZnO). This allows for any porosity differences in the top oxide film to be reflected in the *I-V* sensor tests. A schematic of a CuO/ZnO structure is shown in Figure 5.3. Patterning of the films was achieved through lithography and etching procedures. For the ZnO/CuO structures, the top ZnO film was found to etch readily in a 100:1 ratio of hydrochloric acid (EMD Chemicals Inc., 36.5 – 38.0%) to DI water. For the CuO/ZnO films, suitable masking of the base ZnO film was achieved prior to the CuO deposition. It should be noted that

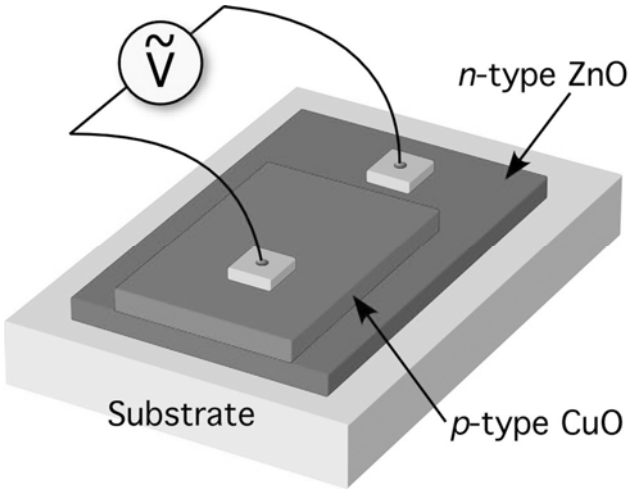

Figure 5.3. A schematic of a CuO/ZnO thin film heterostructure

the schematic depicted in Figure 5.3 is not the most ideal geometry for the heterostructure sensor; certainly electric field distributions will be non-optimal. However the results presented indicate that this is currently not a hindrance to sensor operation.

The structure and overall crystallinity in the films were characterized through θ-2θ scans obtained on a Bruker D8 Discover X-ray diffractometer (XRD) with Cu K_α radiation. Surface morphology and porosity levels were monitored through scanning electron microscopy (SEM) and contact mode atomic force microscopy (AFM). The electron microscopy was performed on a FEI Quanta 200 environmental SEM operated in a 5 kV – 10kV voltage range. AFM images were attained on a Digital Instruments Nanoscope IIIa equipped with silicon nitride tips (Veeco).

The *I*-*V* measurements were performed in a NorECs Probostat high temperature conductivity cell. A schematic of the experimental setup is shown in

Figure 5.4. First, the heterostructures were affixed to alumina plates using electrically conductive silver epoxy (Duralco 124). The component oxide films were then connected via Pt wire electrodes. The sensor tests were performed in dry air (N_2:O_2 = 4:1) and hydrogen (4000 ppm) environments in a tube furnace at 200 °C. The flow rate and concentration of both gases were controlled by mass flow controllers (Omega, FMA 5506/5512) with the fixed total flow rate of 200 sccm. The heterostructures were heated to the measuring temperature and allowed to equilibrate for 30 min. The *I-V* measurements were taken using a high voltage source measure unit (Keithley 237). The applied bias range was from -6 V to +6 V at a step size of 1 V. The delay time was given as 1 second after applying voltages, upon which the current was measured.

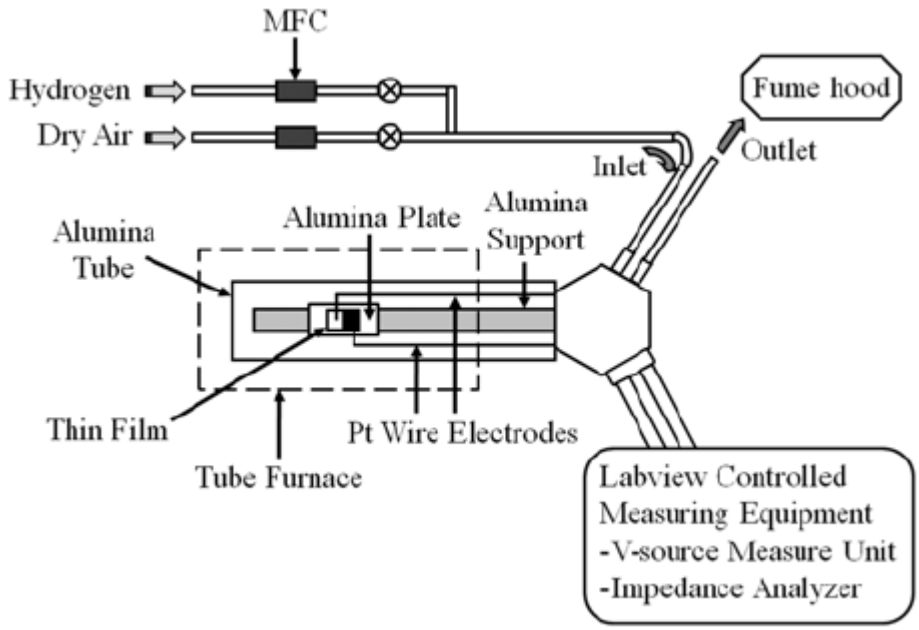

Figure 5.4. The experimental setup used for *I-V* characterization of the heterostructures.

5.3. Results and Discussion

5.3.1. ZnO Film Optimization

ZnO crystallizes into the hexagonal wurtzite structure characterized by strong (0002) peak intensities at $2\theta = 34.4°$. As stated in the introduction, desirable degrees of crystallinity and preferred orientation lead to an increase in charge mobility, and thus should lead to an enhanced sensor response. This is explained by the fact that charge carriers in a more crystalline film undergo a reduction in grain boundary scattering events [14]. Shown in Figure 5.5(a) are the XRD scans of the ZnO films. Utilizing 50 °C increments, an optimal pyrolysis temperature range of 250 °C – 300 °C was found. Subsequent pyrolysis experiments at 225 °C and 275 °C also yielded high degrees of preferred orientation. A comparison in the ratio of (0002) peak intensity to that of the $(10\bar{1}1)$ intensity for each XRD scan is shown in Figure 5.5(b). The $(10\bar{1}1)$ peak ideally has the greatest intensity in bulk, polycrystalline ZnO samples. Full-width at half-maximum (FWHM) data for the (0002) peak are plotted against pyrolysis temperature in the inset of Figure 5.5(b). Pyrolysis temperatures of 250 °C and 275 °C were seen to yield higher (0002): $(10\bar{1}1)$ peak ratio values. Of these two samples, the film pyrolyzed at 250 °C possessed a minimum in (0002) FWHM.

The effect of pyrolysis temperature on preferred orientation has been explored in previous studies [12, 15]. Ohyama *et al.* found that an undesirably high pyrolysis temperature may lead to abrupt solvent evaporation and thermal decomposition of the

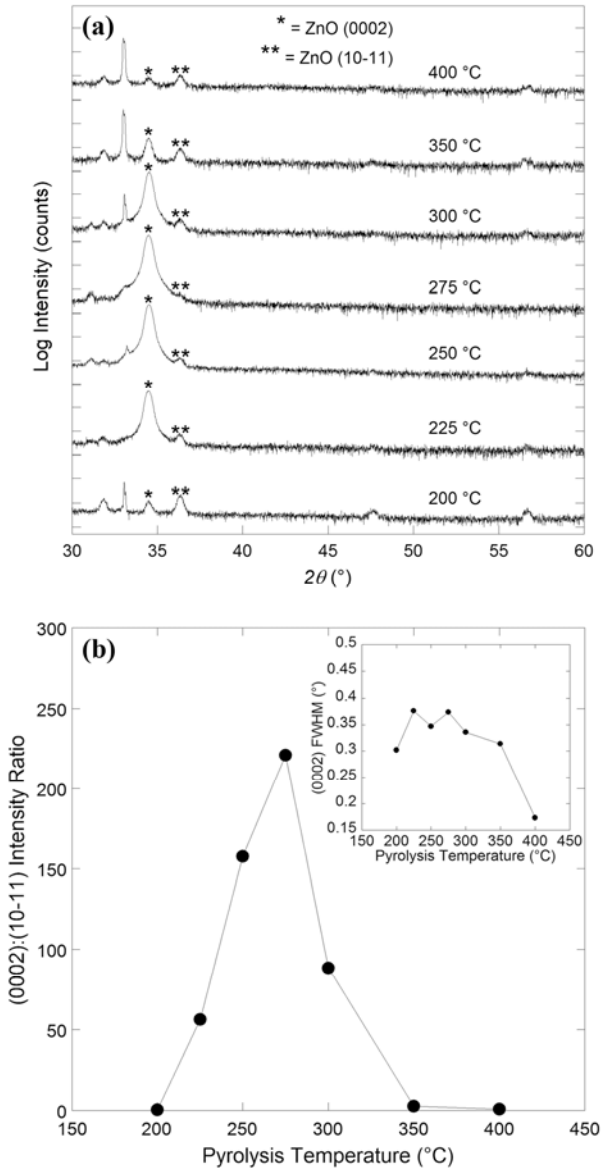

Figure 5.5. XRD scans (a) of the ZnO films (offset for clarity) showing the effect of pyrolysis temperature on the preferred orientation and (0002) peak intensity at $2\theta =$ 34.4. The graph in (b) is a comparison of the (0002): $(10\bar{1}1)$ peak intensity ratios at different pyrolysis temperatures; a line has been added to guide the eye. The (0002) FWHM values are plotted against pyrolysis temperature in the inset.

zinc acetate. The effect of this scenario on film structure can be seen by examining the fundamentals of the sol-gel process. The formation of a highly crystalline ceramic thin film depends on a dried gel consisting of atoms arranged in a manner very close to that of the final crystalline ceramic phase [16]. A subsequent annealing treatment then provides the atoms with enough thermal energy to properly arrange into the final crystalline product. Abrupt organic evaporation and zinc acetate decomposition serves to perturb this ideal scenario and as such, a more random film with a low degree of crystallinity is attained when the pyrolysis temperature is too high. Alternatively, an undesirably low pyrolysis temperature can lead to insufficient thermal energy imparted into the constituent atoms. Compared to an optimized pyrolysis step, this gel will possess atoms further removed from ideal positions. The resulting effect is that, for a given annealing treatment, the crystallization of a film with an insufficient pyrolysis temperature will lag behind that of an optimized film. Another effect of an undesirably low pyrolysis temperature is an incomplete burnout of solution organics. In this scenario, abrupt evaporation and thermal decomposition of the zinc acetate occur during the annealing phase which again yields a more randomly oriented structure and causes film crystallization to lag behind its optimized counterpart. However, incomplete organic evaporation, if held to an acceptable degree, actually enhances thin film porosity, a finding which is addressed below.

The effect of drying temperature on the porosity of the ZnO films was also examined. The SEM scans shown in Figure 5.6 reflect the porosity difference at

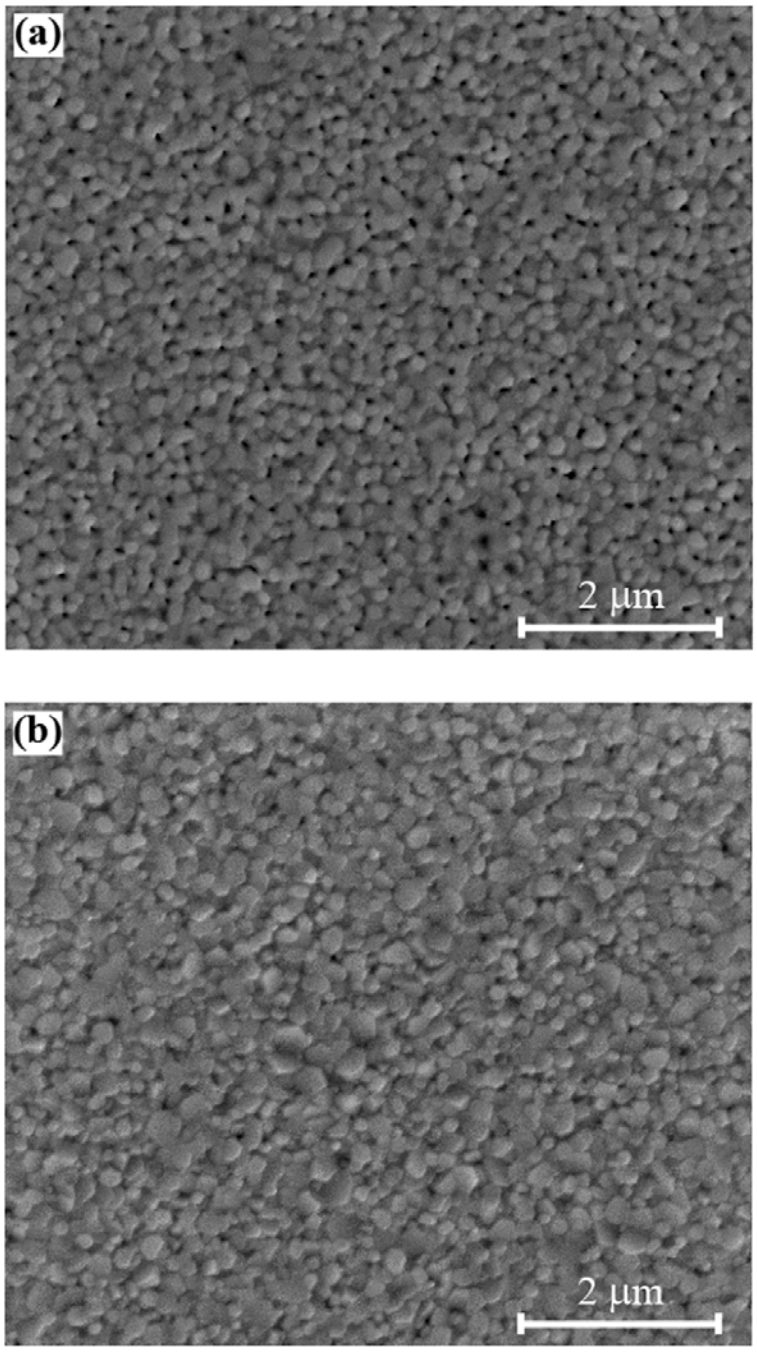

Figure 5.6. Two ZnO films pyrolyzed at (a) 250 °C and (b) 300°C. The lower pyrolysis temperature leads to an imcomplete burnout of the organics, resulting in a significantly more porous microstructure.

pyrolysis temperatures of 250 °C and 300 °C. The ZnO film dried at 250 °C (Figure 5.6(a)) displayed a clear increase in porosity over the film dried at 300 °C (Figure 5.6 (b)). This difference is due to an incomplete burnout of the liquid organics during pyrolysis. While this effect hindered the densification of the thin film, it was not so severe as to impede crystallization, as evidenced in the XRD data of Figure 5.5(a). It should be noted that no cross-sectional analysis was performed in this study. Thus, the possibility exists that the observed porosity seen here may not extend through the thickness of the film. However, assuming that the kinetics of analyte diffusion are enhanced as the porosity is increased, the *I-V* testing of the heterostructures may serve to verify a porosity level that extends throughout the dimensions of the film. Shown in Figure 5.7 are AFM images of a typical ZnO film taken at scan sizes of 3 μm (Figure 5.7(a)) and 1 μm (Figure 5.7(b)). These micrographs show a faceted microstructure that may be indicative of ZnO with (000*l*) orientation perpendicular to the substrate. Since pyrolysis at 250 °C produced ZnO samples with an optimal balance of crystallinity and porosity, this process parameter was chosen for films incorporated into the heterostructure.

5.3.2. CuO Film Optimization

As noted above, optimization of the CuO films was focused on the effect of pyrolysis temperature on crystallinity. The XRD data for the CuO films are shown in Figure 5.8, with FWHM measurements given in parentheses. In analyzing these scans,

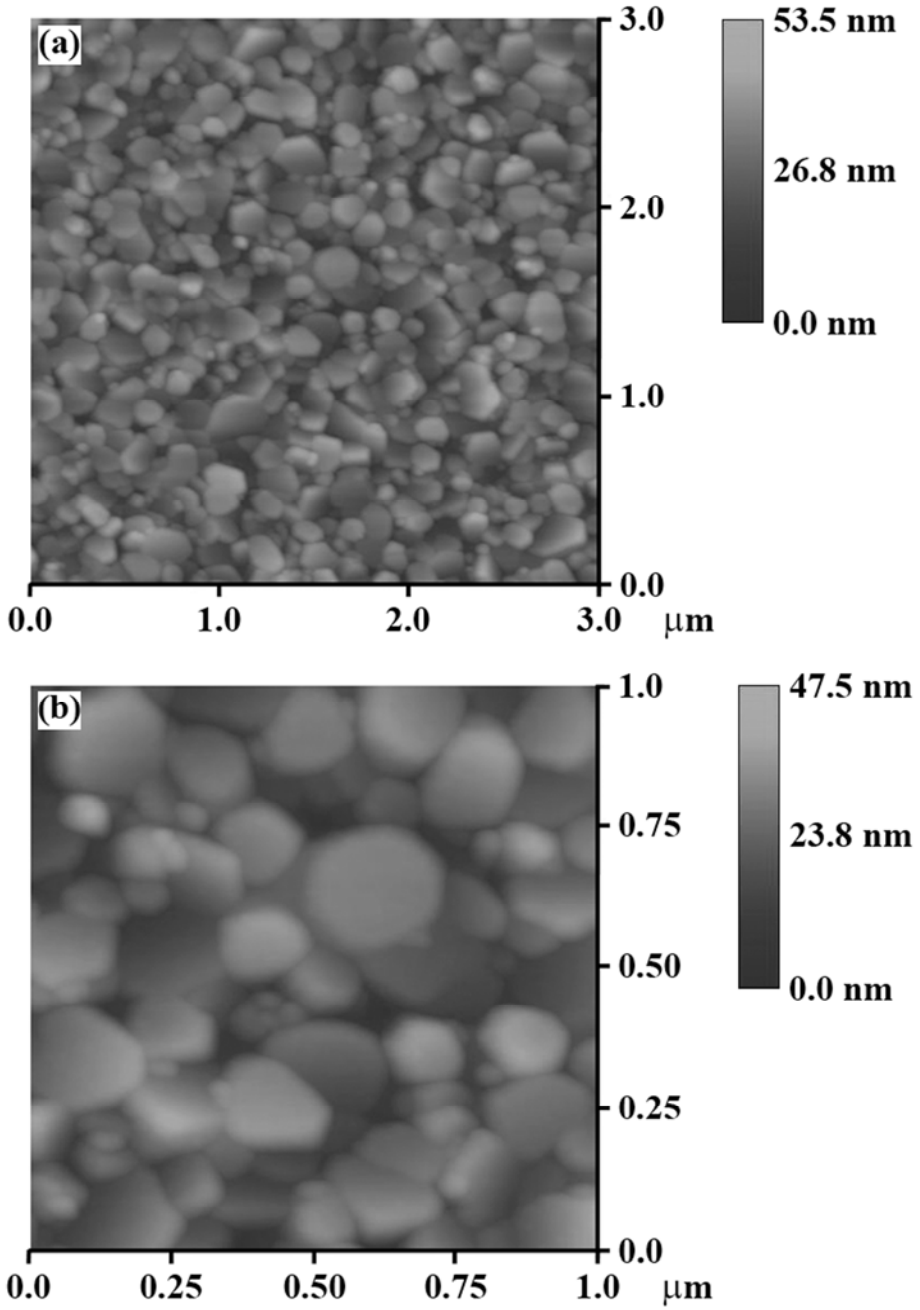

Figure 5.7. AFM images of a typical ZnO film taken at scan sizes of 3 μm (a) and 1 μm (b). Note the faceted microstructure, perhaps indicative of ZnO with (000*l*) orientation perpendicular to the substrate.

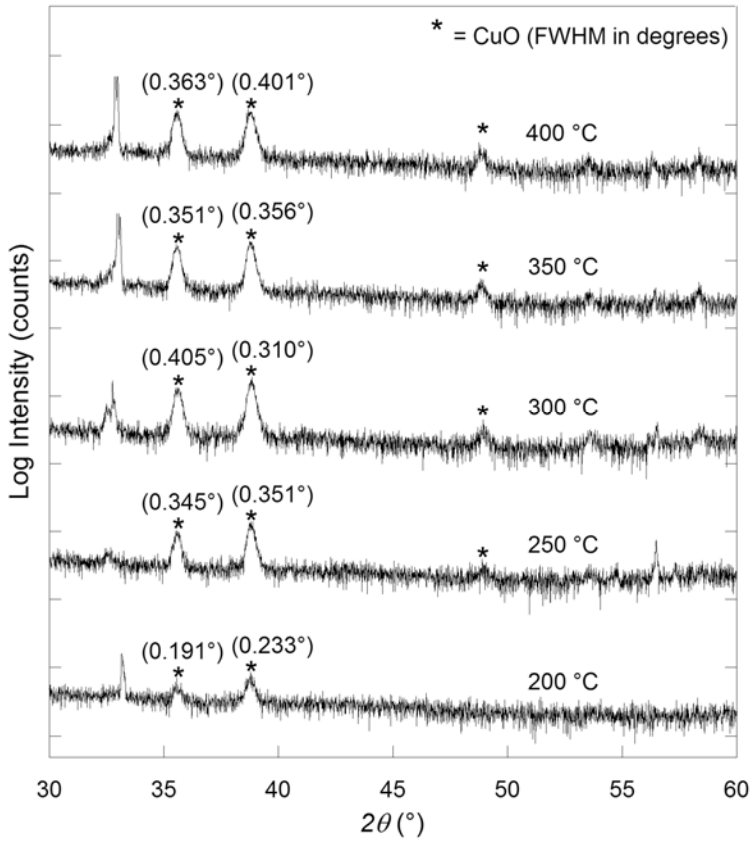

Figure 5.8. The XRD scans of the CuO films pyrolyzed at different temperatures. Each scan is offset for clarity, with asterisks denoting tenorite peaks and FWHM data shown in parentheses.

two key objectives were desired. Of initial concern was the attainment of single phase tenorite with no cuprite (Cu_2O) phase present. The second desired result was to maximize the tenorite peak intensities. While the XRD scans of Figure 5.8 show no evidence of cuprite, a higher degree of crystallinity was attained in the CuO films pyrolyzed above 200 °C. This is apparent by the appearance of the $(20\overline{2})$ peak at 48.7°

above 200 °C. In the XRD spectra of a polycrystalline CuO sample, the reflections of highest intensity are found at 35.5° and 38.7°. Above 200 °C, minimum FWHM values for these peaks are found at 250 °C and 300 °C respectively.

The SEM and AFM images of a film pyrolyzed at 250 °C are shown in Figure 5.9. When comparing the SEM scan of Figure 5.9(a) with that of the ZnO film pyrolyzed at 250 °C in Figure 5.6(a), a significantly higher level of porosity was apparent. Due to the relative ease of porosity formation in the CuO films, only the effects of drying temperature on CuO crystallinity were explored. These microscopy results also point to the ideality of CuO as the top film layer in a *pn*-heterostructure. Keeping in mind the trends in porosity seen in the ZnO samples as well as the comparable crystallinity of the CuO films pyrolyzed above 200 °C, a drying temperature of 250 °C was chosen as the process parameter for films used in the heterostructures.

5.3.3. Heterostructure Characterization and Testing

Upon optimization of the component oxide films, planar thin film heterostructures were fabricated. Figure 5.10 shows XRD and SEM data for a representative 10 layer ZnO/CuO sample. Strong (000*l*) ZnO orientation is seen in Figure 5.10(a) along with the desired tenorite peaks. The porosity difference between the bottom CuO layer and top ZnO layer are evident in Figure 5.10(b). SEM measurements of the “step” in the top ZnO layer of Figure 5.10(b) confirm the 30 nm

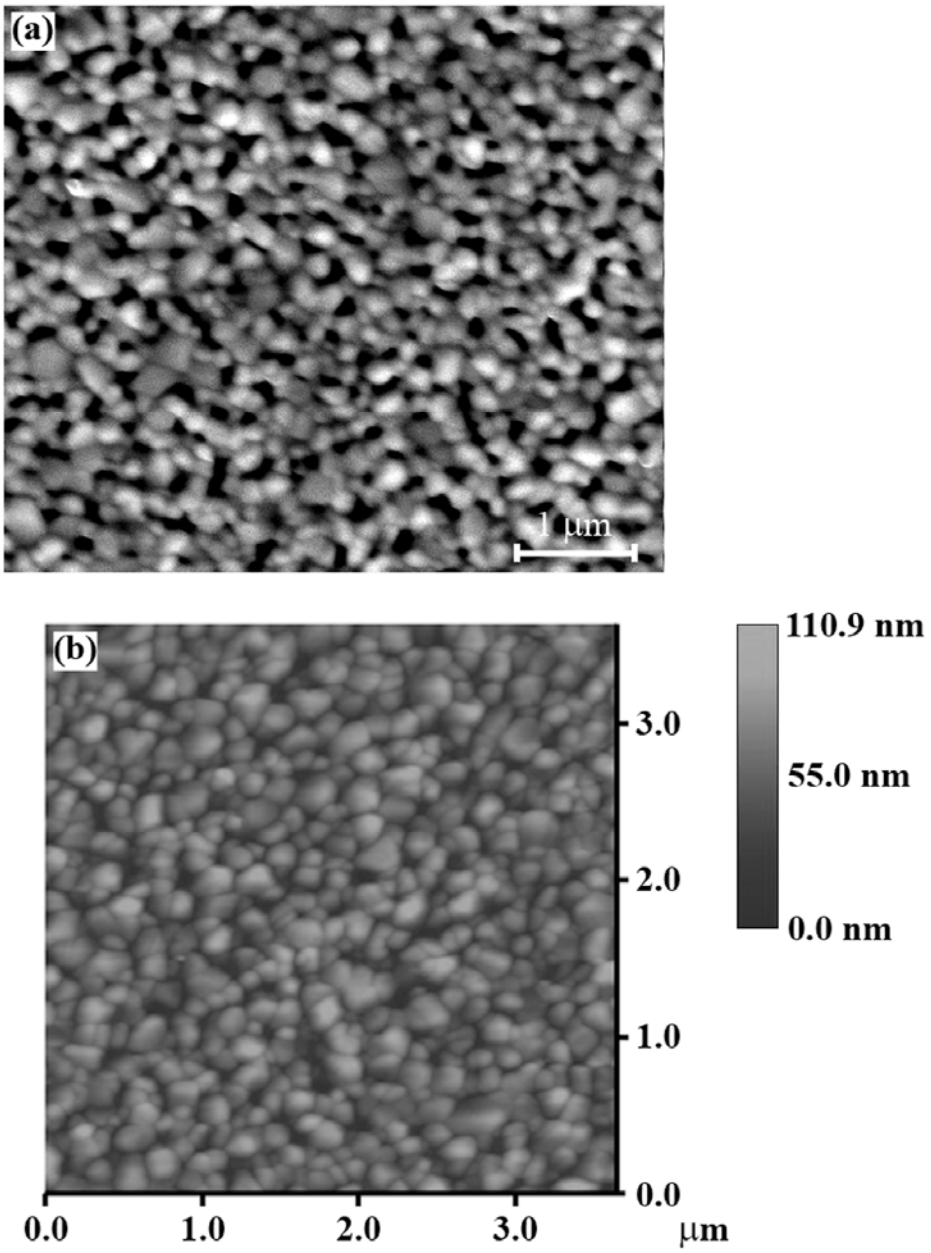

Figure 5.9. SEM (a) and AFM (b) images of a CuO film pyrolyzed at 250 °C. The inherently high level of porosity seen in the CuO films points to its ideality as the top oxide film in a *pn*-heterostructure.

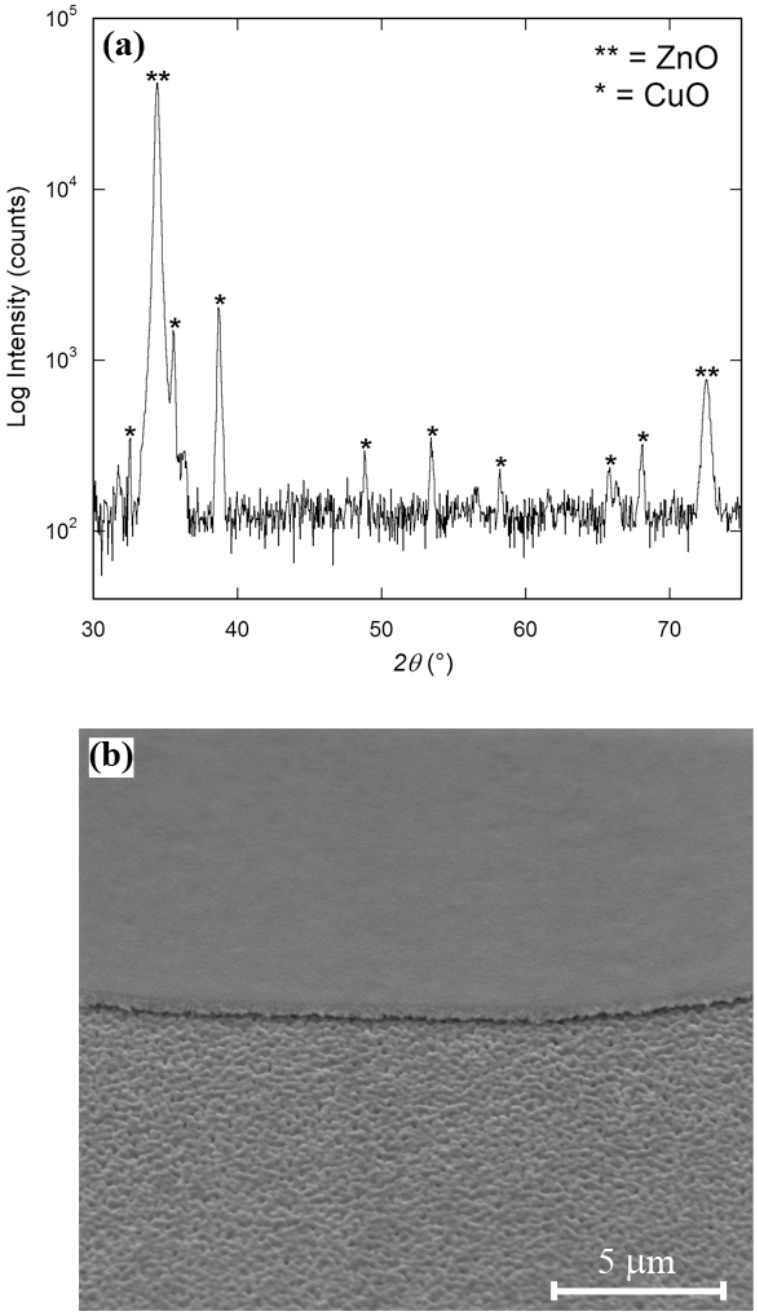

Figure 5.10. The XRD data (a) show a (000*l*) oriented ZnO film along with the tenorite phase. The porosity difference between the bottom CuO layer and top ZnO layer is evident in the SEM scan shown in (b).

per-layer ZnO film thickness attained through profilometry measurements.

Current-voltage measurements on the two types of heterostructures (CuO/ZnO and ZnO/CuO) are shown in Figure 5.11. Sensing effects in 4000 ppm hydrogen are demonstrated in both cases, however as expected the structure with a top CuO layer shows enhanced sensing capability. This was due to the aforementioned porosity difference between CuO compared to ZnO. The effects shown are similar to those found in bulk systems [6, 7]. It must be stressed that these initial tests are on non-

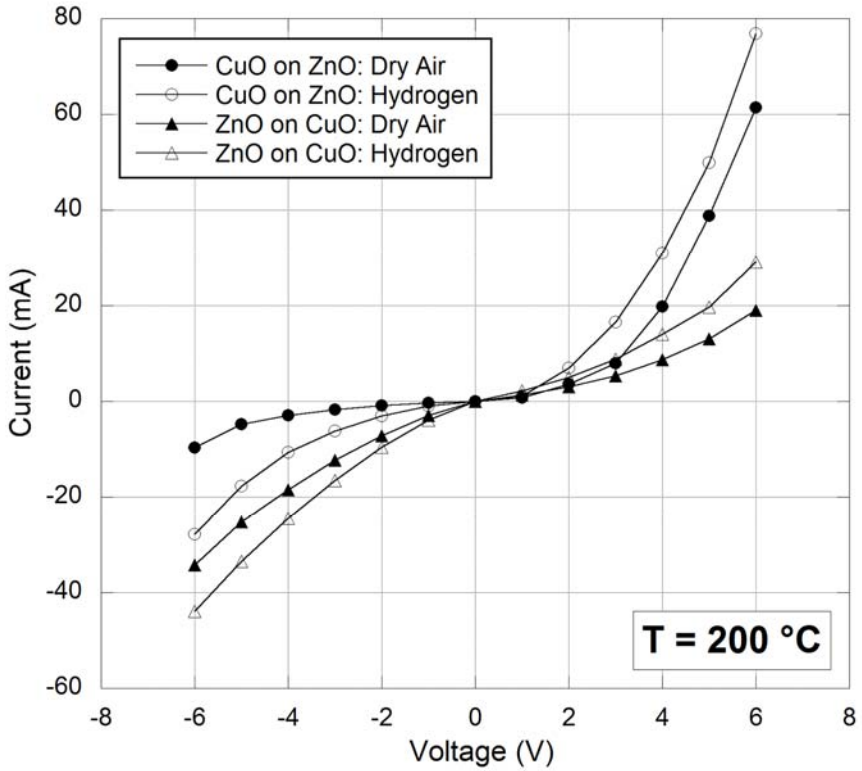

Figure 5.11. The *I-V* measurements of CuO/ZnO and ZnO/CuO heterostructures in dry air and 4000 ppm hydrogen. The high level of porosity in the top CuO layer of the CuO/ZnO structure leads to an increase in device sensitivity.

optimized electrode geometries, thus significant improvement is expected in both the sensitivity and rectifying behavior of the devices. Work is currently underway to fabricate heterostructures on platinum-coated silicon substrates. The addition of a bottom platinum electrode along with a patterned interdigital top electrode is expected to generate ideal electric field lines for maximum sensor response.

5.3.4. Mixed Solution Films

The phase equilibria between ZnO and CuO exhibits no intermediate phases and limited solubility. This allows for the creation of thin film microstructures that increase the degree of connectivity (and thus the interfacial area) between the ZnO and CuO. Structures have been fabricated that involve a combination of the aforementioned ZnO and CuO precursor solutions into one mixture. A pyrolysis temperature of 250 °C was used and the spin-coating/annealing parameters were identical to the values specified in the individual ZnO and CuO processes. The belief is that an optimization of pyrolysis and annealing treatments will yield a structure consisting of both CuO and ZnO grains. This configuration would ideally result in enhanced sensor response due to both the high degree of component oxide connectivity and the almost negligible diffusion paths encountered by the analyte. The diffusion path is effectively the thickness of the film. Shown in Figure 5.12(a) is an XRD scan of a mixed solution structure. Clearly evident in this data was the presence of strong ZnO (000*l*) peak intensity along with the desired tenorite phase. Morphologies obtained from AFM imaging, shown in Figure 5.12(b), also indicated

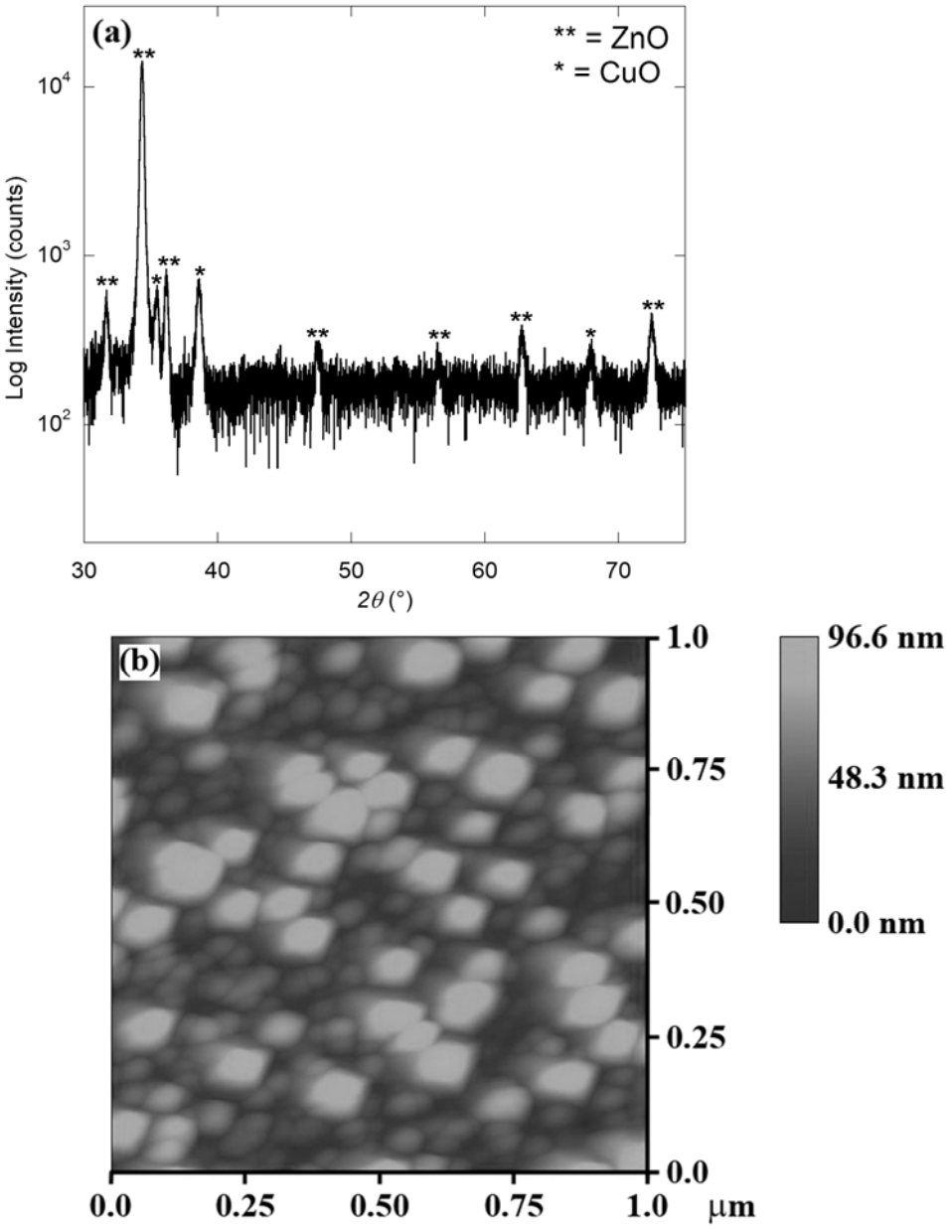

Figure 5.12. An XRD scan (a) of a mixed solution structure shows the presence of ZnO preferred orientation along with the tenorite phase. The AFM image in (b) indicates the possible appearance of ZnO amidst a matrix of CuO.

the possible presence of ZnO surrounded by a CuO matrix. This image may also be compared to the individual films (Figures 5.7(a) and 5.9(b)) where pronounced similarities can be seen. Further verification via elemental spectroscopy is ongoing. Testing this structure will involve patterning of interdigital electrodes on the film surface.

5.4. Conclusions

Thin films of ZnO and CuO have been fabricated and optimized with respect to pyrolysis temperature. It was found that the ZnO films produced from a MOE-based solution method exhibited the best combination of porosity and crystallinity at a pyrolysis temperature of 250 °C. Thin films of CuO also pyrolyzed at 250 °C exhibited a significant degree of porosity and the desired tenorite structure. These films were then incorporated into a planar thin film heterostructure in two configurations, ZnO on CuO and CuO on ZnO. Sensor response data via *I-V* measurements were found to be enhanced when CuO was employed as the top film layer. This was due to its inherent high porosity that facilitated faster diffusion of the analyte to the heterostructure interface. It was noted that while the component oxide films have been optimized, the electrode geometry has not undergone a similar procedure. It is the belief that with a suitable electrode configuration, the response of the sensor as whole will be greatly enhanced. Lastly, preliminary XRD data and AFM imaging was given on a mixed solution thin film structure that is proposed to

significantly enhance the response of the *p*-CuO/*n*-ZnO sensor to reducing environments.

Acknowledgements

The authors wish to acknowledge funding from the Army Research Laboratory and the Oregon Nanoscience and Microtechnologies Institute.

References

[1] Y. Nakamura, A. Ando, T. Tsurutani, O. Okada, M. Miyayama, K. Koumoto, H. Yanagida, Chem. Lett. (1986) 413.
[2] H.L. Hartnagel, A.L. Dawar, A.K. Jain, C. Jagadish, Semiconducting Transparent Thin Films, Institute of Physics, New York, 1995.
[3] M. Kawasaki, A. Ohtomo, I. Ohkubo, H. Koinuma, Z.K. Tang, Y. P., G.K.L. Wong, B.P. Zhang, Y. Segawa, Mater. Sci. Eng., B 56 (1998) 239.
[4] U. Ozgur, Y.I. Alivov, C. Liu, A. Teke, M.A. Reshchikov, S. Dogan, V. Avrutin, S.-J. Cho, H. Morkoc, J. Appl. Phys. 98 (2005) 041301.
[5] G. Eranna, B.C. Joshi, D.P. Runthala, R.P. Gupta, Crit. Rev. Solid State Mater. Sci. 29 (2004) 111.
[6] S. Aygun, D. Cann, J. Phys. Chem. B 109 (2005) 7878.
[7] S. Aygun, D. Cann, Sens. Actuators, B, Chem. 106 (2005) 837.
[8] S. Kwon, S. Aygun, D.P. Cann, Sens. Lett. 3/3 (2005) 1.
[9] M. Miyayama, K. Hikita, G. Uozumi, H. Yanagida, Sens. Actuators, B, Chem. 24-25 (1995) 383.
[10] S. Mridha, D. Basak, Semicond. Sci. Technol. 21 (2006) 928.
[11] K.-K. Baek, H.L. Tuller, Solid State Ionics 75 (1995) 179.
[12] M. Ohyama, H. Kozuka, T. Yoko, S. Sakka, J. Ceram. Soc. Jpn. 104/4 (1996) 296.
[13] A.Y. Oral, E. Mensur, M.H. Aslan, E. Basaran, Mater. Chem. Phys. 83 (2004) 140.
[14] Z.Q. Xu, H. Deng, Y. Li, Q.H. Guo, Y.R. Li, Mater. Res. Bull. 41 (2006) 354.
[15] M. Ohyama, H. Kozuka, T. Yoko, Thin Solid Films 306 (1997) 78.
[16] G. Yi, M. Sayer, Ceram. Bull. 70 (1991) 1173.

Chapter 6. Thin film *n*-ZnO/*p*-CuO heterostructures fabricated via mixed solution method

6.1 Introduction

One of the most critical parameters in gas sensor design is device selectivity; the ability of a sensor to detect and quantify the presence of a gaseous species (the analyte) among common interferents. The lack of selectivity inherent in many metal oxide gas sensors (e.g. ZnO, SnO_2) has spurred the use of external measures such as temperature control [1], filters [2], and the use of catalysts for preferential analyte diffusion [3, 4]. In 1986, Nakamura *et al*. found that bulk *p*-CuO/*n*-ZnO heterocontacts exhibited intrinsic selectivity characteristics [5]. The reaction proposed for this structure in the detection of carbon monoxide (CO) can be written as [6]:

$$[n\text{-ZnO}]: O_2 + 2e^- \rightarrow 2O^- \quad (6.1)$$

$$[p\text{-CuO}]: 2CO + 2h^+ \rightarrow 2CO^+ \quad (6.2)$$

$$[\text{interface}]: 2CO^+ + 2O^- \rightarrow 2CO_2 \quad (6.3)$$

A reaction between adsorbed oxygen on the *n*-ZnO (6.1) and CO on the *p*-CuO (6.2) leads to the evolution of carbon dioxide (6. 3) and a subsequent reduction in the potential barrier to charge carrier movement across the device interface. This reduction can be quantified through appropriate dc current-voltage (*I*-*V*) testing of the heterostructure [7, 8]. Analyte selectivity for *p*-CuO/*n*-ZnO heterocontacts has been attained via impedence spectroscopy through a variance in the applied bias or measuring frequency [9-11].

While bulk *p*-CuO/*n*-ZnO heterocontacts have demonstrated desirable sensitivity and selectivity characteristics, these structures possess innate disadvantages. First, the analyte must often traverse a circuitous diffusion path to reach the heterostructure interface. This serves to limit sensitivity and response time. Second, the contact area, or connectivity between the CuO and ZnO is low, which minimizes the effective interfacial area of the device. With these drawbacks in mind, studies have shifted to focus on thin film geometries to increase analyte diffusion kinetics and sensor interfacial area. Work performed by Baek and Tuller utilized sputtered CuO on bulk polycrystalline ZnO substrates, with the resulting structures displaying enhanced *I-V* characteristics under reduced oxygen partial pressures [12]. Research has also been successful in fabricating sol-gel derived thin film *p*-CuO/*n*-ZnO heterostructures [13, 14]. A schematic of this structure type is shown in Figure 6.1.

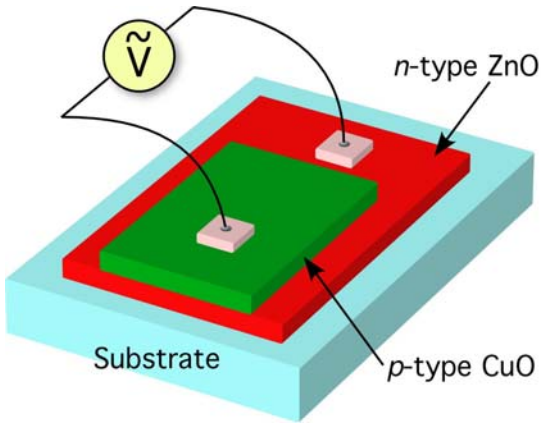

Figure 6.1. A schematic representation of a planar thin film p-CuO/n-ZnO heterostructure.

The synthesis of thin films via sol-gel processing is particularly appealing due to the low cost of necessary equipment, the high homogeneity of synthesized films, and the potential for large area coverage [15]. In addition, with this method it is relatively straightforward to modify the process such that unique microstructures are achieved. In this particular case the immiscibility of CuO and ZnO allows for the creation of innovative sensor designs that further increase the degree of connectivity, and thus should quicken response times. Here, ZnO and CuO precursors have been combined into one solution so as to fabricate a novel microstructure consisting of individual metal oxide grains. The resulting device (schematically represented in Fig. 6.2) possesses a high degree of connectivity and an almost negligible diffusion path for the analyte. The morphology and structure of these sensors have been

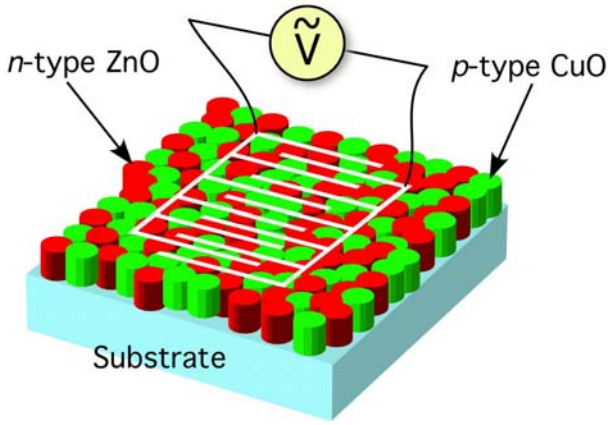

Figure 6.2. A schematic illustration of the novel sensor design fabricated in this work. A high degree of ZnO/CuO connectivity is present and analyte diffusion paths are negligible.

characterized via x-ray diffraction (XRD), atomic force microscopy (AFM), and scanning electron microscopy (SEM). Elemental analysis to confirm phase separation has also been performed.

6.2. Experimental

The substrates used in this work were <100> silicon supplied by the Sumco Corporation (USA). For the ZnO precursor solutions, 2-methoxyethanol (MOE: Alfa Aesar, 99%) and zinc acetate dihydrate ($Zn(CH_3COO)_2 \cdot 2H_2O$: Alfa Aesar, 98.0 – 101.0%) were employed as solvent and solute, respectively. Monoethanolamine (MEA: Alfa Aesar, 99+%) was added as a stabilizing agent, with the molar ratio of MEA to zinc atoms held constant at 1.0; solutions were 0.6 M. This ZnO process is similar to fabrication methods found in previous studies [16, 17].

For the CuO solutions, a process modeled after work done by Oral *et al*. was used [18]. Copper (II) acetate monohydrate ($Cu(CH_3COO)_2 \cdot 2H_2O$: Alfa Aesar, 98.0 – 102.0%) was dissolved in isopropanol (Alfa Aesar, 99.5%) with MEA added as a stabilizer. Polyethylene glycol (PEG-400: Alfa Aesar) was employed to optimize solution viscosity and de-ionized (DI) water was introduced so as to facilitate hydrolysis. The content of PEG-400 and MEA was kept constant at a 5% by volume concentration, while the DI water was used at concentration of 2% by volume. The molarity of the CuO precursors was 0.25 M.

Upon successfully fabricating homogeneous CuO and ZnO precursors, the solutions were combined so as to keep a 1:1 molar ratio of Cu:Zn atoms. This mixed

solution was then stirred for 10 min at room temperature. Film depositions consisted of 5 layers and were performed via spin-coating using 3 mL syringes equipped with 0.2 μm filters (Fisherbrand). The silicon substrates were cleaned with isopropanol prior to deposition. Pyrolysis was performed on a hot plate in the temperature range of 200 °C – 400 °C in 50 °C increments. Annealing was done at 550 °C in a furnace open to air, after which the films were allowed to cool to room temperature. At this point, film structure was examined so as to determine the optimal pyrolysis temperature. This optimized pyrolysis temperature was then held constant and the effects of annealing temperature on grain growth and phase separation was explored. Three 5-layer film sets were employed in which the annealing temperature was varied in the range of 700 °C – 900 °C in 100 °C increments. An additional film set comprised of three 15-layer films was annealed at 800 °C. One film from each set was annealed for 1, 5, and 10 hours in order to examine crystal structure and ZnO/CuO connectivity.

Film structure was characterized through θ-2θ scans performed on a Bruker D8 Discover XRD with Cu K_α radiation. Film morphology of the mixed solution films was examined through SEM and contact mode AFM. AFM scans were done on a Digital Instruments Nanoscope IIIa equipped with silicon nitride tips (Veeco). SEM images were obtained on a FEI Quanta 200 in the voltage range of 10 – 15 kV. Elemental composition was characterized using Energy Dispersive Spectroscopy (EDS) performed with a Moran System SIX setup at 15 kV.

6.3. Results and Discussion

6.3.1. XRD data

For polycrystalline CuO, the reflections of highest intensity are found at 35.5° and 38.7° in 2θ. In thin film ZnO, preferred *c*-axis orientation leads to a strong reflection at 34.4°. As the films in this study are deposited on single crystal silicon, a (004) half-order reflection at ~33.5° may also be found in some scans. Shown in Figure 6.3 is the XRD data for the films pyrolyzed at 200 °C – 400 °C. Strong CuO and ZnO peak intensities are seen at drying temperatures above 200 °C. A maximization of ZnO (002) preferred orientation appears to exist in the range of 300 °C – 350 °C. The CuO peak intensity at 38.7° appears to be highest above 250 °C. Since definitive evidence of CuO and ZnO structure are shown throughout the pyrolysis range, a drying temperature of 300 °C was chosen for the annealing experiments.

The XRD scans for the 700 °C annealing run are shown in Figure 6.4. The relative intensities of the CuO and ZnO peaks remains virtually unchanged throughout the range of annealing times. This indicates an absence of CuO or ZnO vaporization or reaction at this annealing temperature; a critical concern given the relatively large surface-to-volume ratio inherent in thin film geometries.

The XRD data for the films annealed at 800 °C are shown in Figure 6.5. A slight degradation is seen in the (002) ZnO peak intensity, while the CuO reflection at 38.7° remains relatively constant. The ZnO peak found at 36.2°, known to be of

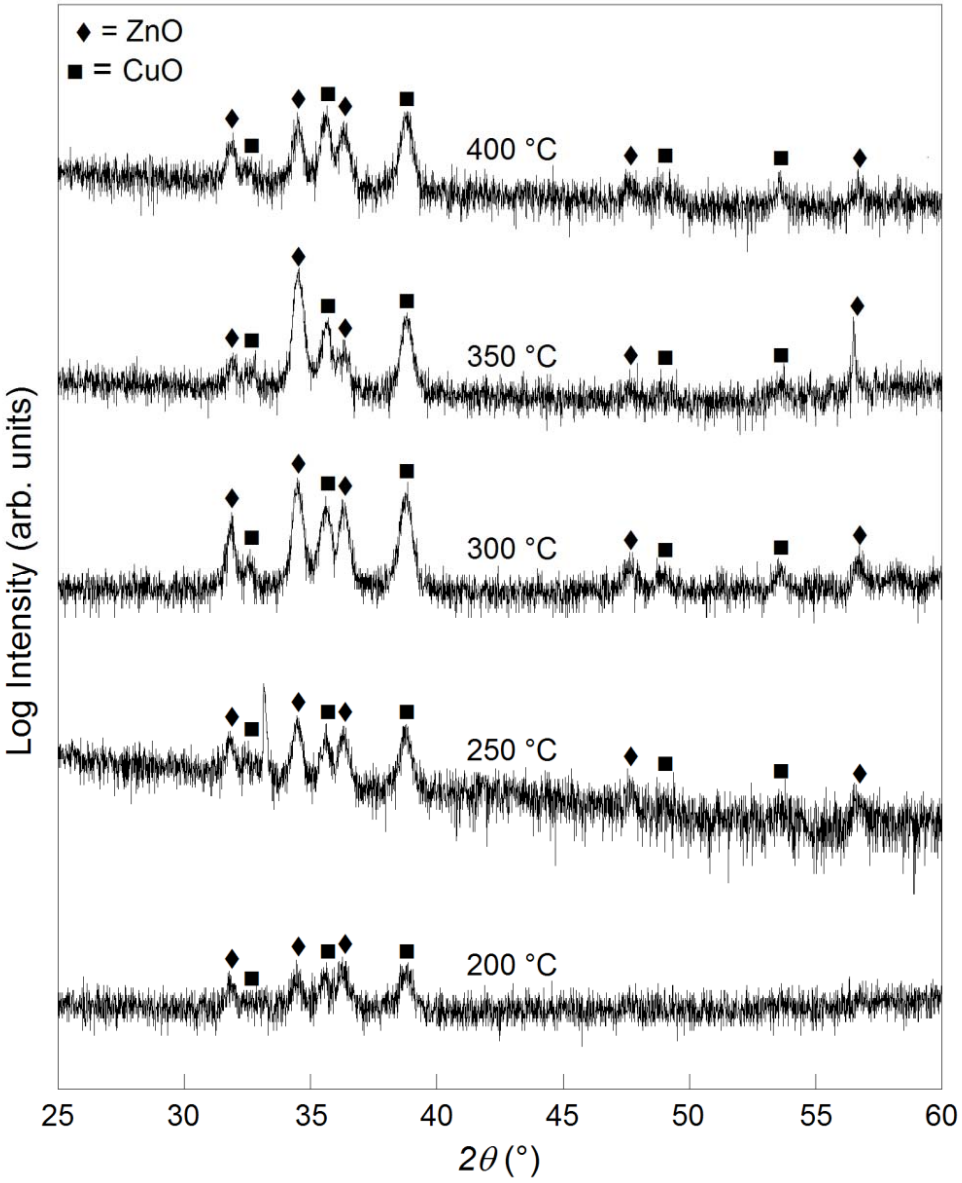

Figure 6.3. The XRD spectra of the films pyrolyzed at 200 °C – 400 °C. Strong CuO and ZnO intensities are seen above 200 °C.

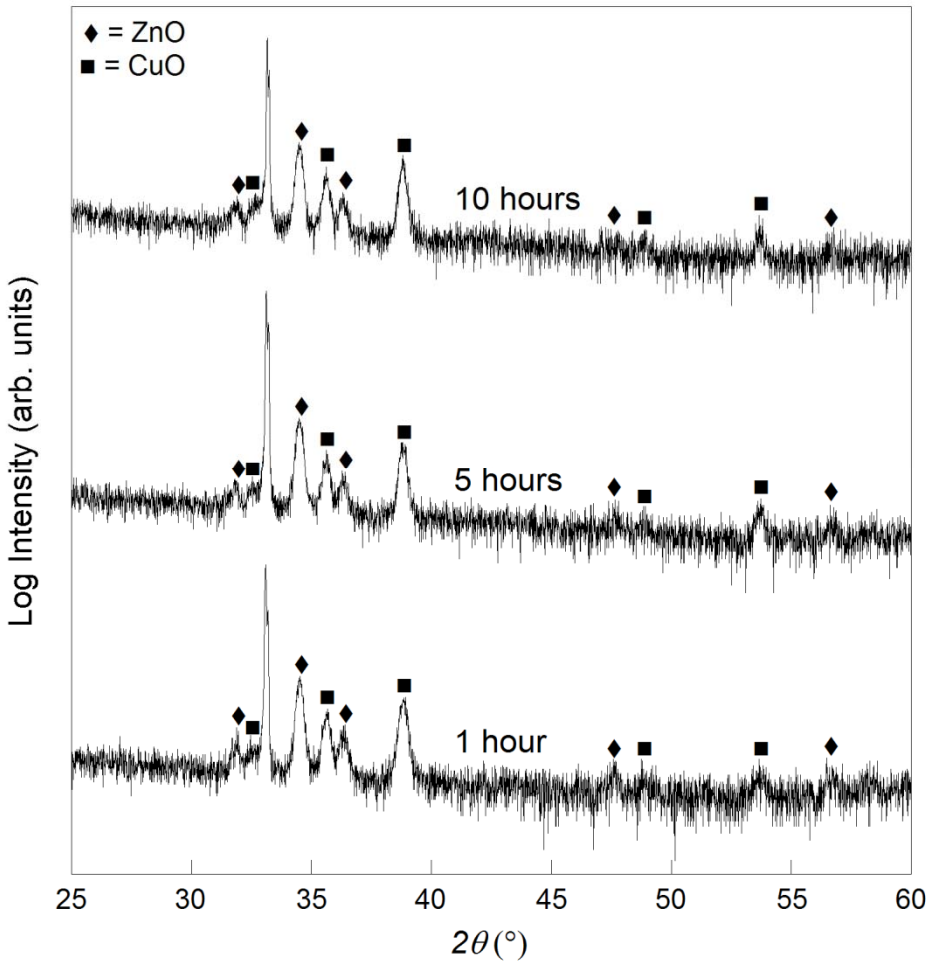

Figure 6.4. The XRD spectra for the films annealed at 700 °C. The relative intensities of the CuO and ZnO peaks remains virtually unchanged throughout the range of annealing times.

highest intensity in bulk polycrystalline samples, also undergoes a slight reduction in magnitude. The formation of a reaction phase not seen at 700 °C is found throughout the annealing times used. While these reflections have not yet been definitively characterized, possible candidates include silicon dioxide (SiO_2) and zinc silicate

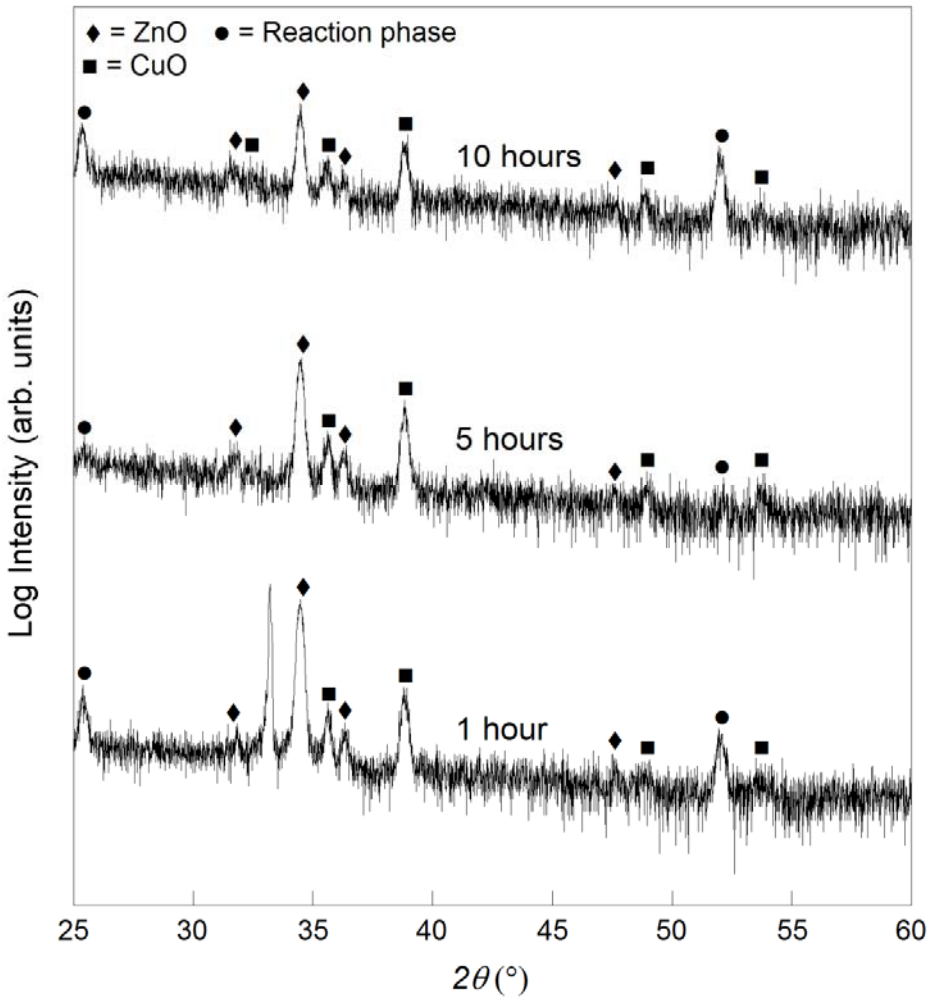

Figure 6.5. The mixed solution film set annealed at 800 °C. A slight degradation in ZnO peak intensities may signal either ZnO volatilization or the formation of a reaction phase.

(Zn_2SiO_4). At 800 °C, it is possible that ZnO either begins to volatilize or form a reaction phase as the annealing time is increased. If this is indeed the case, the obvious concern would be the reduced ZnO/CuO connectivity resulting from this scenario.

This in turn could lead to a gas sensor possessing a lower sensitivity when compared to mixed solution films annealed at lower temperatures.

Shown in Figure 6.6 are the XRD scans of the films annealed at 900 °C. Above an annealing time of 1 hour, ZnO peaks effectively vanish. While the CuO reflection at 38.7° is rather weak, it persists throughout the annealing treatment. It appears that a

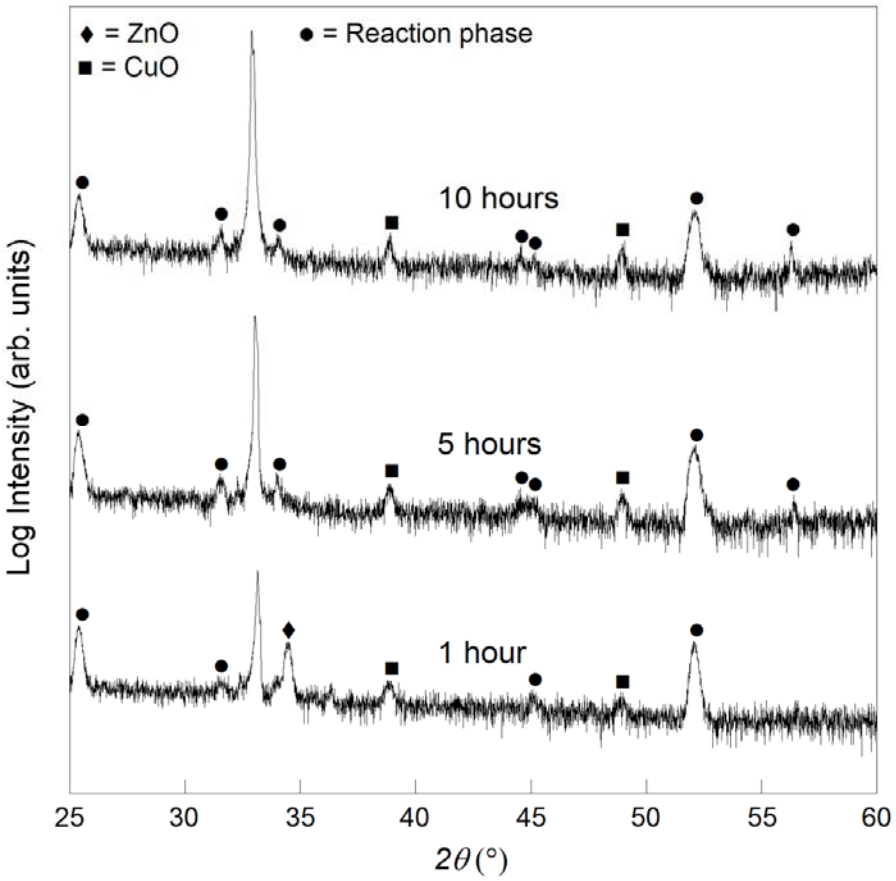

Figure 6.6. The XRD data for the mixed solution films annealed at 900 °C. Above 1 hour, ZnO peaks effectively vanish as a result of volatilization or reaction phase formation.

900 °C annealing temperature leads to either rapid ZnO volatization or enhanced reaction phase formation. A fine balance appears to exist between inducing phase separation and drastically reducing ZnO/CuO film connectivity.

The XRD scans for the 15-layer films annealed at 800 °C are shown in Figure 6.7. Strong CuO and ZnO reflections are seen throughout the spectra, with the film

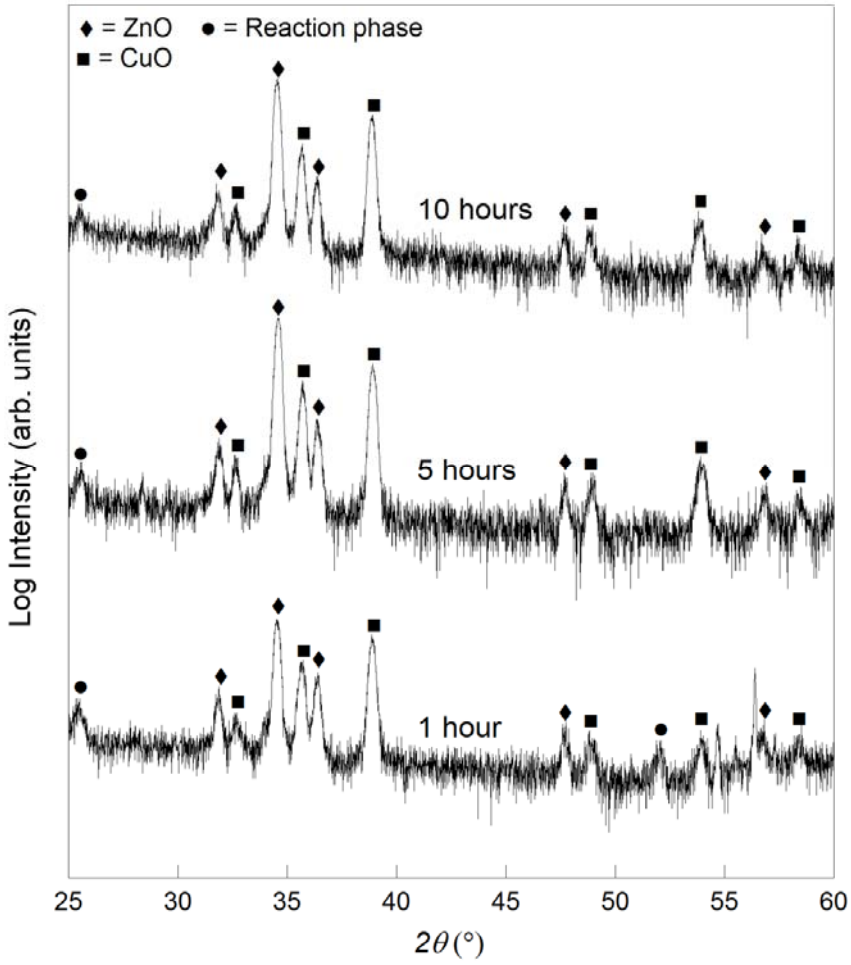

Figure 6.7. The XRD data for the 15-layer films annealed at 800 °C. The peak intensities show a slight maximum at 5 hours with little degradation up to 10 hours.

annealed at 5 hours displaying a slight maximum in peak intensities. Little degradation is seen at 10 hours, likely due to the lower surface-to-volume ratio inherent in these thicker films.

6.3.2. AFM data

Upon suitable characterization of film crystal structure, the morphologies of the annealed films were examined. The goal was to observe the effects of temperature on grain growth and the degree of connectivity between the ZnO and CuO. Shown in Figure 6.8 are the AFM scans of the 700 °C annealing series. While grain size has not been quantified, significant growth is not evident. There does however appear to be a coherent network of CuO and ZnO grains across this sample set (given the phase separation seen in XRD characterization), making this annealing temperature a possible process parameter for the fabrication of an effective gas sensor.

The onset of grain growth is evident in the AFM scans of the 800 °C films, shown in Figure 6.9. Note the significantly larger grain size in Figure 6.9(c) when compared to Figure 6.8(c). In addition, the 800 °C annealing temperature appears to induce a reduction in ZnO/CuO connectivity. The resulting microstructure (specifically at 5 and 10 hours) is comprised of larger, more separated ZnO and CuO grains. This indicates that annealing times longer than 1 hour at 800 °C may not be ideal for increasing the sensitivity of gas sensors based on mixed solution process methods.

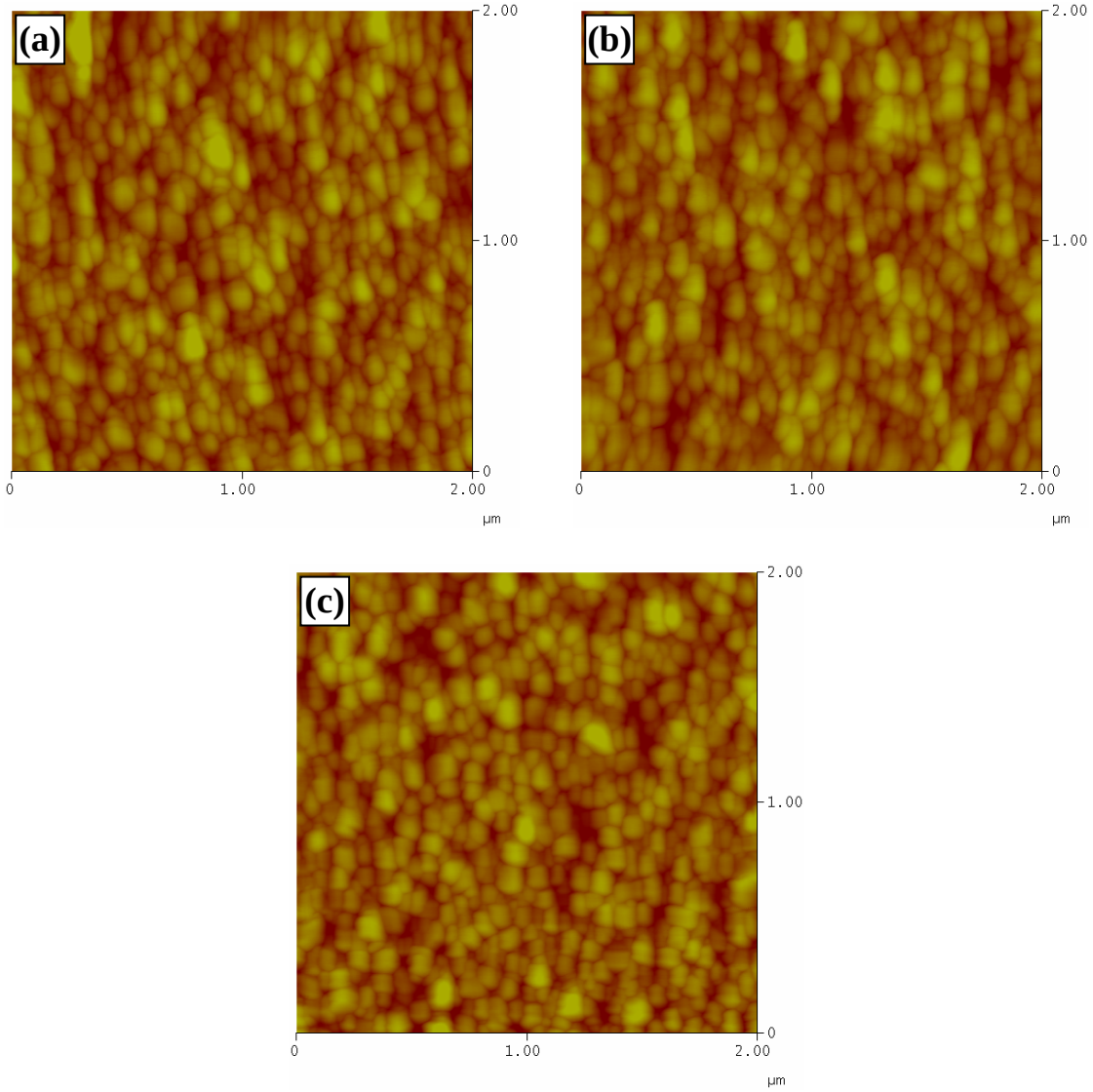

Figure 6.8. The AFM scans for the films annealed at 700 °C for times of (a) 1 hour, (b) 5 hours, and (c) 10 hours. Significant grain growth is not observed, but a high degree of ZnO/CuO connectivity points to the ideality of this process parameter for gas sensor fabrication.

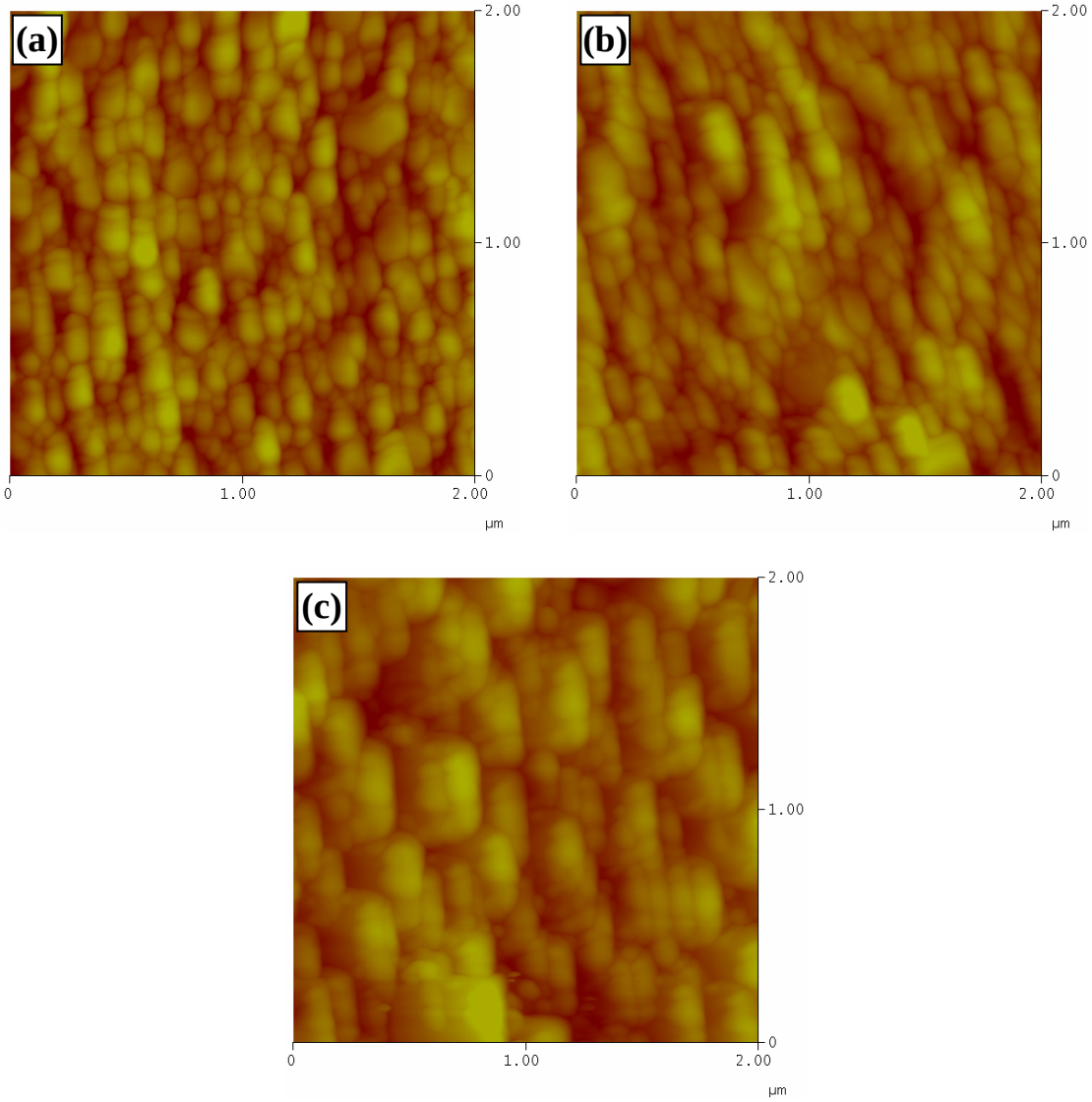

Figure 6.9. The mixed solution films annealed at 800 °C for (a) 1 hour, (b) 5 hours, and (c) 10 hours. At 10 hours, a significant increase in grain diameter is observed over the film annealed at 1 hour.

Shown in Figure 6.10 are the AFM scans of the 900 °C annealing treatment. Large spherical grains are seen in Figure 6.10(a) which effectively disappear after 10 hours (Figure 6.10(b)). In correlating these trends with the XRD data above, it appears that rapid volatilization or reaction phase formation has taken place. As a heterostructure gas sensor is driven by interfacial phenomena, 900 °C appears to be much too high of an annealing temperature in device fabrication. To confirm the visual observations apparent in the AFM data, EDS and SEM data will now be presented.

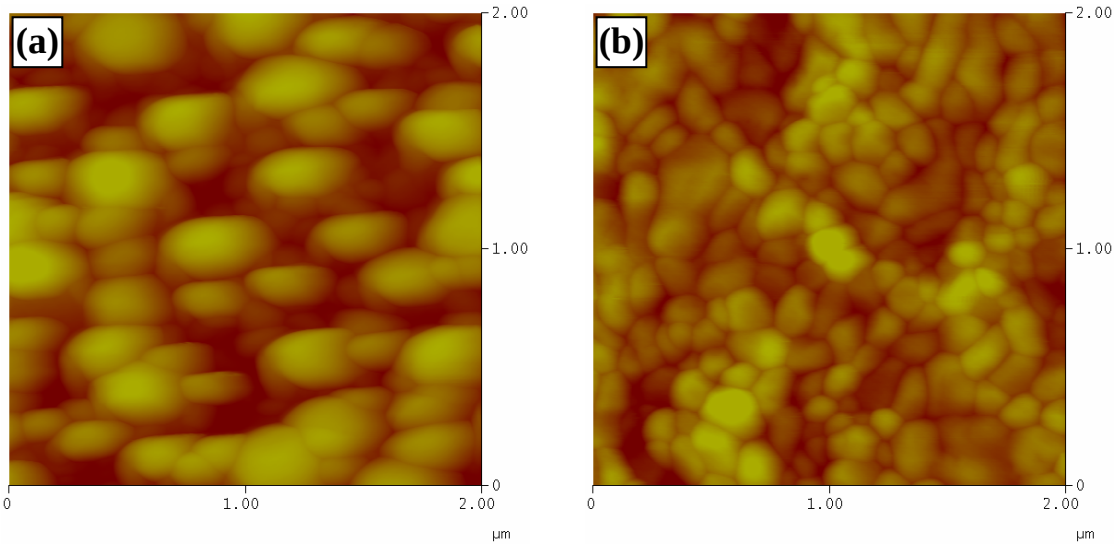

Figure 6.10. AFM scans for mixed solution films annealed at 900 °C for (a) 1 hour and (b) 10 hours. The absence of large grains in (b) points to either ZnO/CuO vaporization or the formation of a reaction phase.

6.3.3. EDS and SEM Results

To confirm the existence of separated CuO and ZnO grains, the mixed solution film annealed at 900 °C for 1 hour was imaged via SEM. EDS analysis was also performed. The SEM image is shown in Figure 6.11. Note the high degree of what appears to be segregated grains of CuO and ZnO. A separate region of this same film

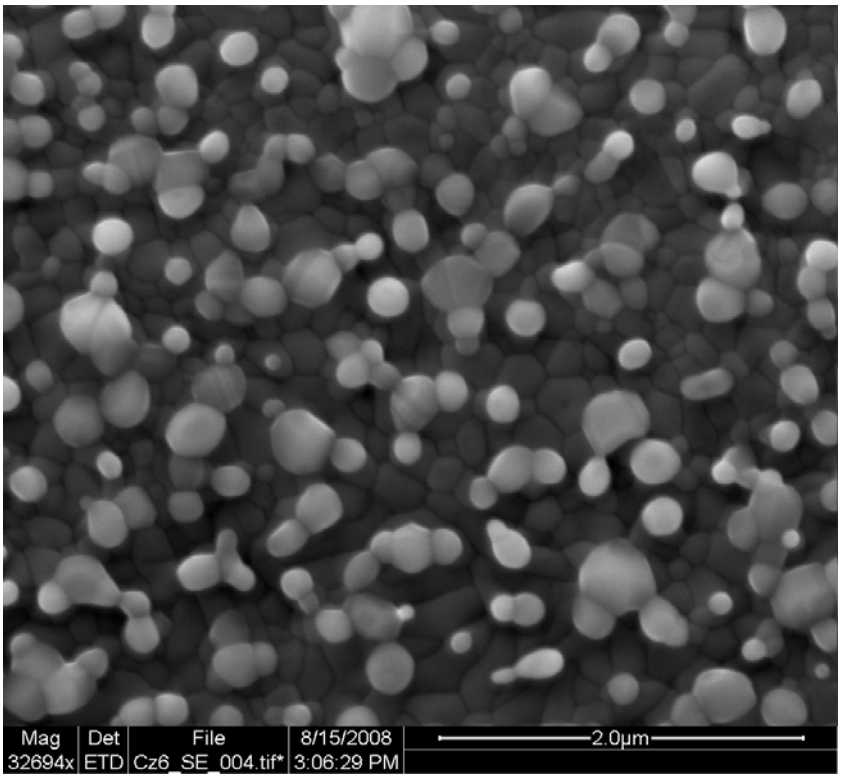

Figure 6.11. An SEM image of a mixed solution film annealed at 900 °C for 1 hour. Spherical CuO and ZnO grains appear to have segregated due to the high thermal energy imparted during the anneal.

was imaged so as to perform EDS analysis. The elemental profile is displayed in Figure 6.12. Silicon is denoted in red, CuO-rich regions in yellow and ZnO-rich regions are in blue. These images support the assumption that CuO and ZnO have separated into spherical grains. However, the morphology of this structure would not be best suited for gas sensing due to the low overall ZnO/CuO interfacial area.

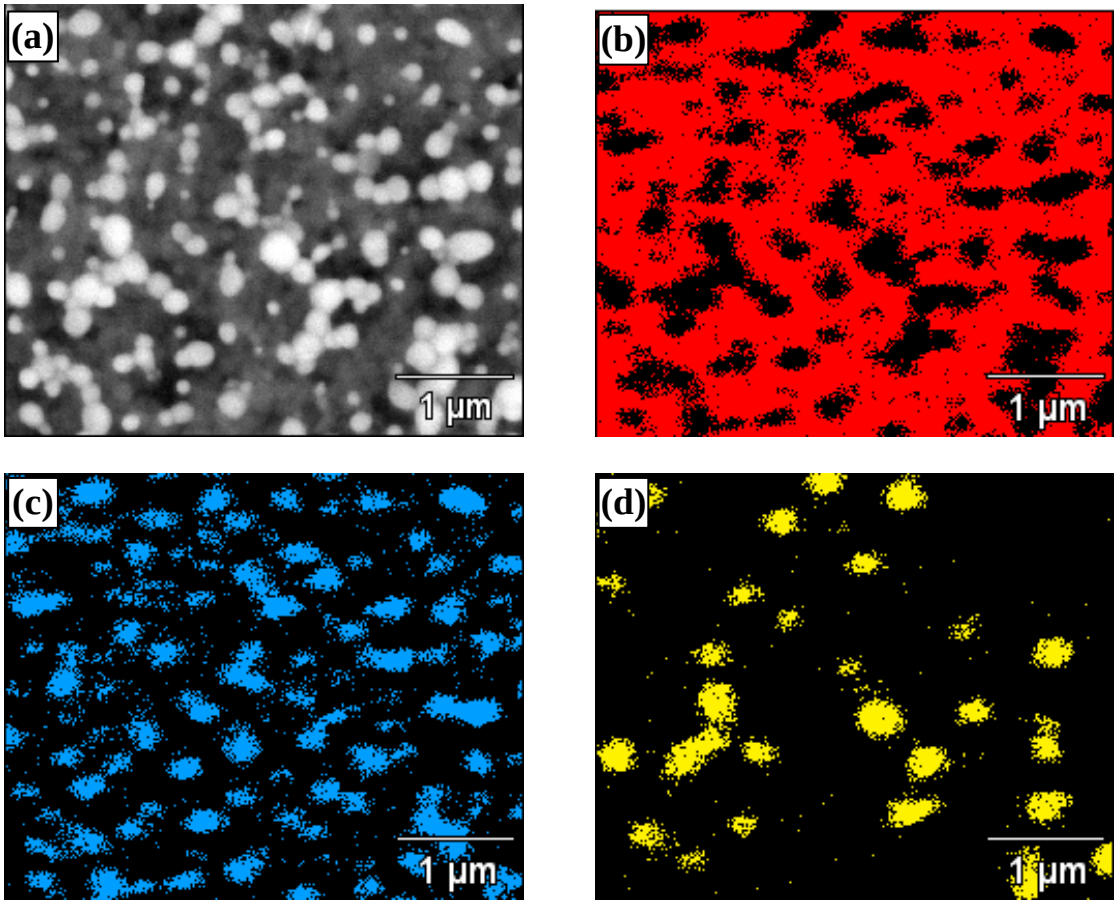

Figure 6.12. EDS profile of a mixed solution film annealed at 900 °C. The raw image is shown in (a). The elemental profile indicates regions rich in (b) silicon, (c) ZnO, and (d) CuO.

An interesting morphology in the film annealed at 900 °C is shown in Figure 6.13(a). Straight, raised regions of material are observed, indicative of de-wetting and agglomeration along preferred crystallographic directions of the underlying silicon substrate. As displayed in Figure 6.13(b), there is an absence of material present in the vicinity directly adjacent to these raised regions. The likely scenario to explain the observed microstructures is as follows. Upon heating to 900 °C, ZnO and CuO have sufficient mobility so as to separate into individual CuO and ZnO grains as seen in Figure 6.11. Specific regions of the underlying silicon substrate allow the separated grains to reach a lower energy state by bonding to that location. As more material migrates to these regions, the surrounding area becomes depleted of ZnO and CuO. The elemental makeup of one of these raised regions was examined to confirm this scenario. The results are shown in Fig 6.14. These data indicate that the agglomerated regions are comprised of ZnO and CuO.

To quantify film thickness, the cross section of a film annealed at 800 °C for 5 hours was examined. The SEM images are shown in Figure 6.15. As indicated in the backscatter electron micrograph of Figure 6.15(a), this film appears to possess a high level of porosity that extends through its entire thickness. At higher magnification (Figure 6.15(b)), the film thickness is observed to be approximately 600 nm. It should be noted that, due to density changes, film thickness may vary with an increase or decrease in annealing temperature. While the degree of connectivity may not be ideal, the high level of porosity should allow for enhanced analyte permeation into the many CuO/ZnO interfaces.

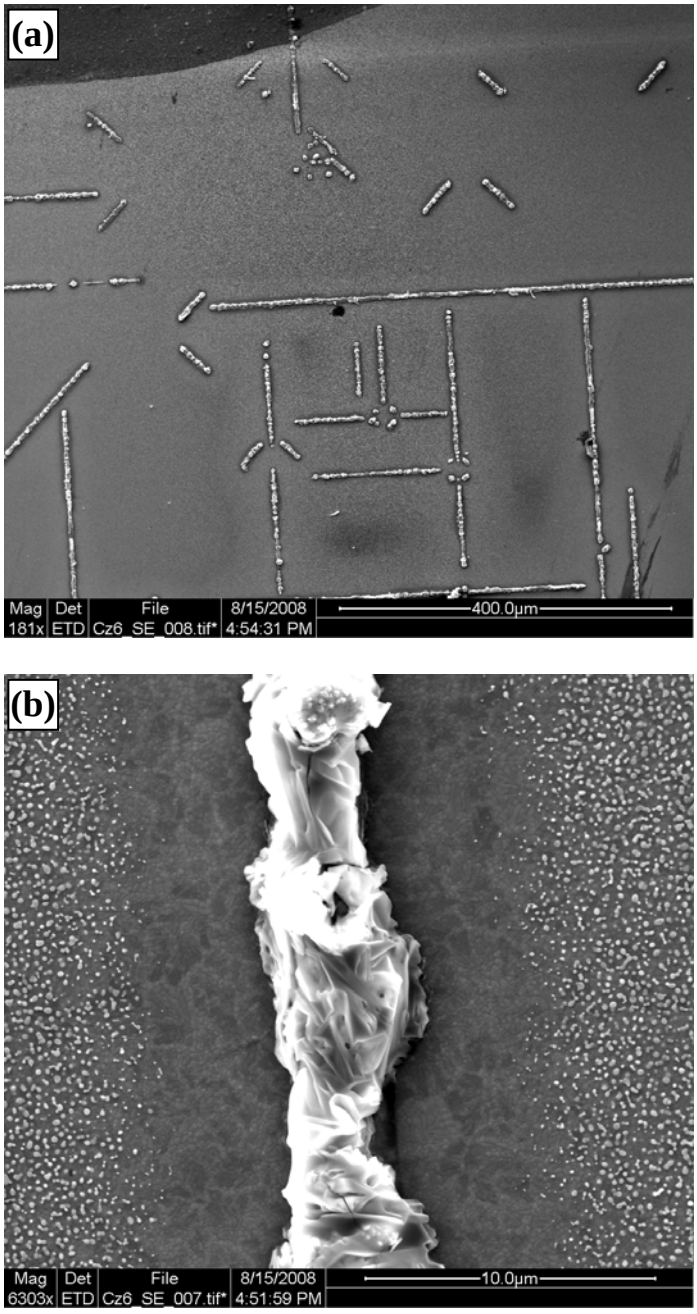

Figure 6.13. The SEM image in (a) shows the narrow raised regions of material on the surface of the film annealed at 900 °C for 1 hour. At higher magnification (b), these raised areas appear to be site for preferential material migration.

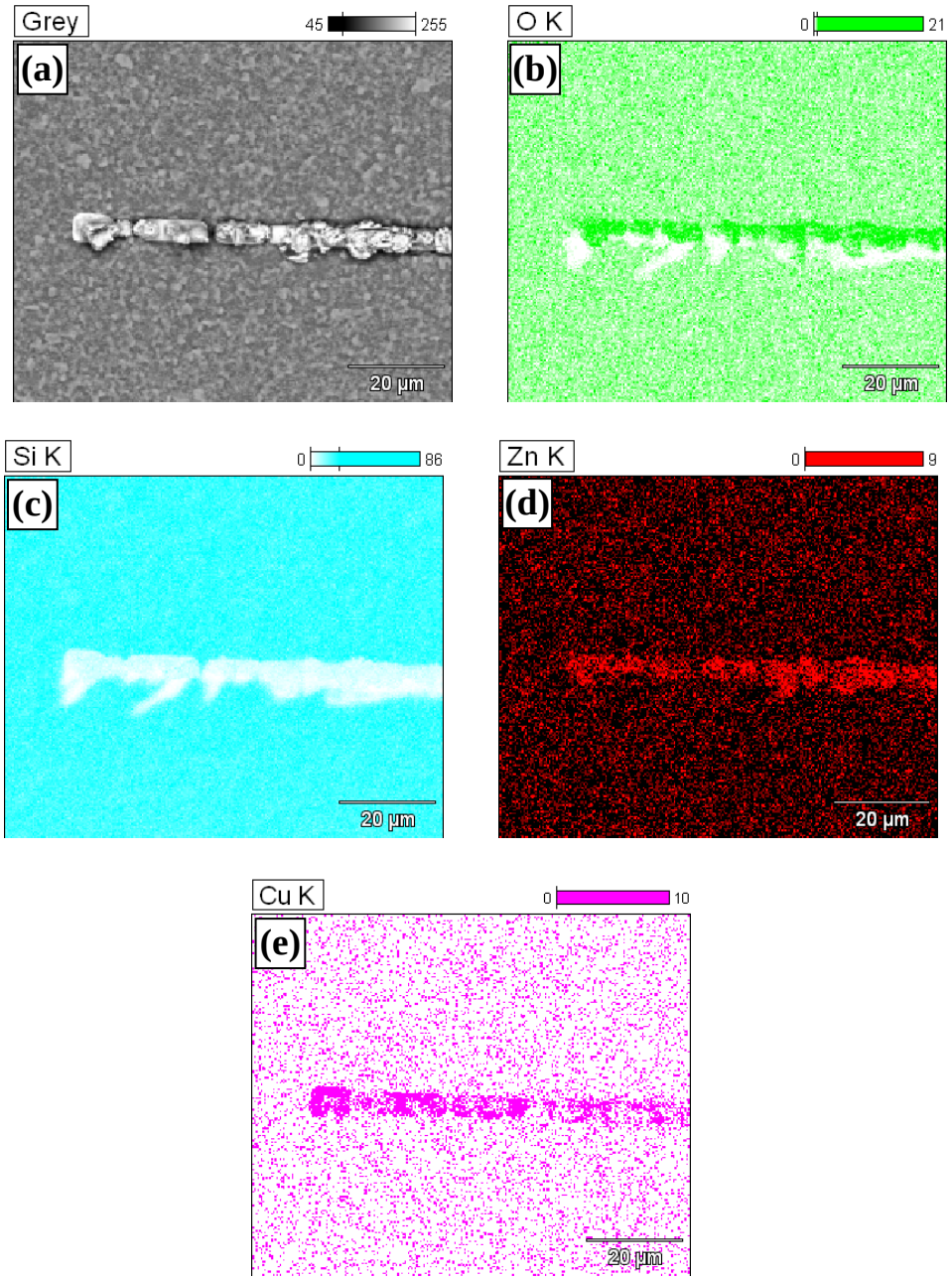

Figure 6.14. EDS analysis of a raised material region (a) on the mixed solution film annealed at 900 °C for 1 hour. Units are of intensity are indicated in counts. Shown are (b) oxygen, (c) silicon, (d) zinc, and (e) copper. The raised region is seen to be rich in CuO and ZnO, while deficient in silicon.

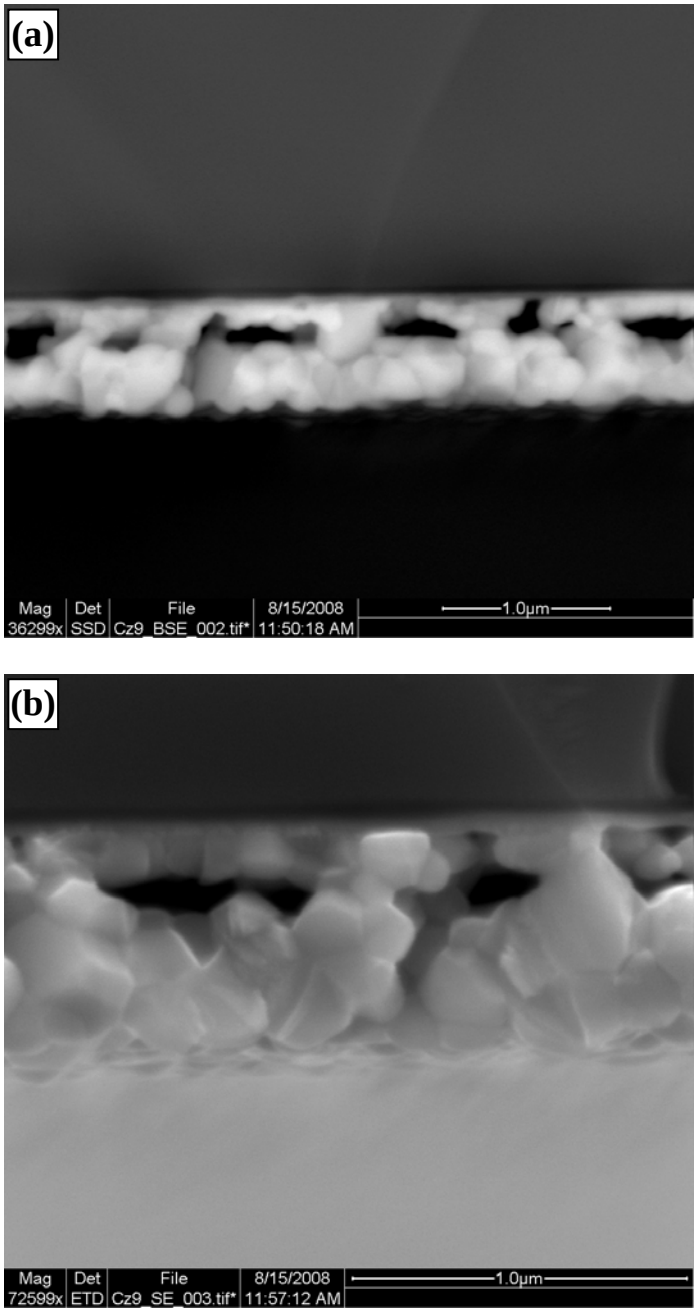

Figure 6.15. Cross-sectional SEM images of a mixed solution film annealed at 800 °C for 5 hours. The film appears to be porous throughout, with a thickness of approximately 600 nm.

SEM images of a 15-layer film annealed at 800 °C for 1 hour are shown in Figure 6.16. Connectivity is clearly demonstrated along with a high degree of porosity. This combination is advantageous for gas detection, as the analyte may easily reach the large interfacial area that exists within the structure.

6.4. Conclusions

This work represents an examination of a novel mixed solution method for fabricating highly connective ZnO/CuO heterostructures for use in gas detection. MOE-based ZnO precursors were combined with CuO solutions and deposited on single crystal silicon substrates. An optimal balance between ZnO and CuO peak intensity was seen at a pyrolysis temperature of 300 °C. With this parameter held constant, 5-layer mixed solution films were annealed in the temperature range of 700 °C – 900 °C in 100 °C increments. Annealing times of 1, 5, and 10 hours were used for one sample in each temperature set. An examination of the XRD data showed the relative intensities of CuO and ZnO to remain fairly constant throughout the 700 °C annealing treatment. At 800 °C, the intensity of the ZnO reflections began to slowly degrade. This indicated possible ZnO volatilization or reaction phase formation as a result of the high annealing temperature and large surface-to-volume ratio inherent in the thin films. At 900 °C, the presence of ZnO began to vanish at times above 1 hour. CuO, while still present throughout the annealing cycle, showed weak XRD reflections. Examination of the 15-layer films annealed at 800 °C for 1 hour showed strong CuO and ZnO peak intensities with minimal degradation up to 10 hours.

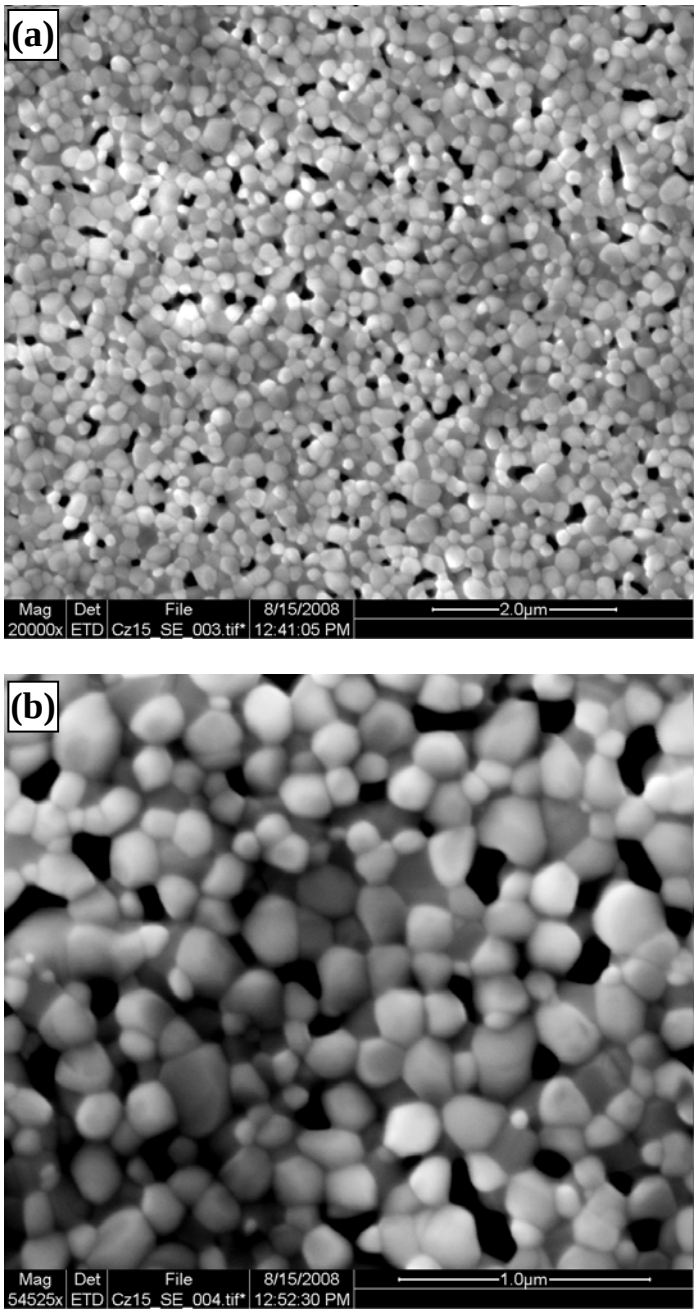

Figure 6.16. SEM images of a 15-layer film annealed at 800 °C for 1 hour. An optimal combination of ZnO/CuO connectivity and porosity is seen in this structure.

AFM data showed minimal grain growth for the 700 °C annealing treatment and enhanced grain growth at 800 °C. For the 900 °C annealing cycle, large grains were seen after 1 hour, but higher heating times led to rapid volatilization or enhanced reaction phase formation. SEM images of the film annealed at 900 °C for 1 hour showed segregated CuO and ZnO grains of spherical shape. Linear, raised material regions were dispersed among these separated grains. EDS analysis confirmed the existence of individual CuO and ZnO grains. The agglomerated regions of material were also found to be composed of ZnO and CuO, an indicator of film de-wetting and migration. Cross-sectional SEM images of a film annealed at 800 °C for 5 hours showed a high level of porosity to exist. Film thickness was observed to be approximately 600 nm. For use in gas sensing designs, films annealed at 700 °C and 800 °C are believed to be ideal candidates. A 700 °C heating temperature yielded what is assumed to be a high level of ZnO/CuO connectivity. While the overall interfacial area of the film annealed at 800 °C may not be ideal, the enhanced porosity has the potential for enhanced analyte diffusion to the ZnO/CuO junctions. Films fabricated at a 900 °C annealing temperature were not seen as favorable gas sensor structures due to their highly separated nature and relative absence of ZnO.

References

[1] R. Lalauze, N.D. Bui, C. Pijolat, in: T. Seiyama, K. Fueki, J. Shiokawa, S. Suzuki (Eds.), Proceedings of the International Meeting on Chemical Sensors, Elsevier, Japan, 1983, p. 47.
[2] L.A. Harris, A titanium dioxide hydrogen detector, J. Electrochem. Soc. 127/12 (1980) 2657.

[3] S.R. Morrison, Selectivity in semiconductor gas sensors, Sensors and Actuators 12 (1987) 425.
[4] S. Saito, M. Miyayama, K. Koumoto, H. Yanagida, Gas sensing characteristics of porous ZnO and Pt/ZnO ceramics, J. Am. Ceram. Soc. 68/1 (1985) 40.
[5] Y. Nakamura, A. Ando, T. Tsurutani, O. Okada, M. Miyayama, K. Koumoto, H. Yanagida, Gas sensitivity of CuO/ZnO hetero-contact, Chem. Lett. (1986) 413.
[6] Y. Nakamura, H. Yoshioka, M. Miyayama, H. Yanagida, T. Tsurutani, Y. Nakamura, Selective CO gas sensing mechanism with CuO/ZnO heterocontact, J. Electrochem. Soc. 137/3 (1990) 940.
[7] S. Aygun, D. Cann, Response Kinetics of Doped CuO/ZnO Heterocontacts, J. Phys. Chem. B 109 (2005) 7878.
[8] S.-J. Jung, H. Yanagida, The characterization of a CuO/ZnO heterocontact-type gas sensor having selectivity for CO gas, Sensors and Actuators B 37 (1996) 55.
[9] K. Hikita, M. Miyayama, H. Yanagida, New gas-sensing method for detecting carbon monoxide by use of complex impedence of a CuO/ZnO heterocontact under a dc bias voltage, J. Am. Ceram. Soc. 77/7 (1994) 1961.
[10] K. Hikita, M. Miyayama, H. Yanagida, New approach to selective semiconductor gas sensors using a dc-biased pn heterocontact, J. Am. Ceram. Soc. 78/4 (1995) 865.
[11] M. Miyayama, K. Hikita, G. Uozumi, H. Yanagida, A.C. impedence analysis of gas-sensing property in CuO/ZnO heterocontacts, Sensors and Actuators B 24-25 (1995) 383.
[12] K.-K. Baek, H.L. Tuller, Atmosphere Sensitive CuO/ZnO Junctions, Solid State Ionics 75 (1995) 179.
[13] C.S. Dandeneau, Y.-H. Jeon, C.T. Shelton, T.K. Plant, D.P. Cann, B.J. Gibbons, Thin film chemical sensors based on *p*-CuO/*n*-ZnO heterocontacts, *Paper submitted to Thin Solid Films* (2008).
[14] S. Mridha, D. Basak, Investigation of a p-CuO/n-ZnO thin film heterojunction for H_2 gas sensor application, Semicond. Sci. Technol. 21 (2006) 928.
[15] G. Yi, M. Sayer, Sol-Gel Processing of Complex Oxide Films, Ceramic Bulletin 70 (1991) 1173.
[16] Y. Kokubun, H. Kimura, S. Nakagomi, Preparation of ZnO thin films on sapphire substrates by sol-gel method, Jpn. J. Appl. Phys., Part 1 42 (2003) L904.
[17] M. Ohyama, H. Kozuka, T. Yoko, S. Sakka, Preparation of ZnO films with preferential orientation by sol-gel method, J. Ceram. Soc. Jpn. 104/4 (1996) 296.
[18] A.Y. Oral, E. Mensur, M.H. Aslan, E. Basaran, The preparation of copper (II) oxide thin films and the study of their microstructures and optical properties, Mater. Chem. Phys. 83 (2004) 140.

Chapter 7. Conclusions

7.1. ZnO and CuO Process Optimization

Adequate control over microstructural variables has been achieved through a variance in sol-gel process parameters. Highly *c*-axis oriented ZnO films were produced by both methoxyethanol (MOE) and dimethylformamide (DMF)-based processes. The degradation of preferred orientation at low drying temperatures was attributed to insufficient thermal energy being imparted into the constituent atoms. At high temperatures abrupt organic burnout and thermal decomposition also leads to a reduction in ZnO *c*-axis orientation. For the MOE-based films optimal preferred orientation was seen at a pyrolysis temperature of 250 °C. As the drying temperature was raised to 300 °C porosity, as observed by SEM imaging, was seen to decrease. This trend was attributed to a more incomplete burnout of liquid organics at 250 °C.

For the DMF-based films, the effects of solution chemistry and drying temperature on ZnO preferred orientation was examined. Optimal solution chemistry was seen to exist at a precursor composition of 5% water and a 1:1 molar ratio of Zn to MEA. A pyrolysis temperature of 350 °C was seen to yield the highest degree of ZnO *c*-axis orientation for this process. AFM imaging showed the existence of bimodal microstructures at high water or MEA contents. Optical absorption coefficient measurements revealed the presence of a sharp excitonic peak at 3.38 eV, an indication of high structural quality. As the pyrolysis temperature was increased from 200 °C to 400 °C the refractive index was seen to increase, while the film thickness

decreased. These opposing trends were likely the result of a density increase, whereby higher pyrolysis temperatures led to more efficient evaporation of solution organics. Van der Pauw measurements showed a monotonic decrease in electrical resistivity as the pyrolysis temperature was raised. This indicated that density is a more critical factor on thin film electrical properties than preferred orientation.

A sol-gel process based on isopropanol was used to fabricate CuO thin films. A pyrolysis temperature of 250 °C was seen to yield the desired tenorite phase with no cuprite present. SEM imaging of these films showed the CuO to possess a level of porosity much higher than that seen in ZnO films.

7.2. Planar Thin Film *p*-CuO/*n*-ZnO heterostructures

Planar thin film heterostructures were fabricated using the CuO and MOE-based ZnO sol-gel processes. These structures were tested for their gas-sensing capabilities in two configurations; ZnO on CuO (ZnO/CuO) and CuO on ZnO (CuO/ZnO). At an operating temperature of 200 °C, the CuO/ZnO devices showed enhanced sensitivity to 4000 ppm H_2 over the ZnO/CuO structures. This enhancement in sensitivity was due to the more porous top CuO layer which facilitated easier diffusion of the hydrogen to the heterostructure interface.

7.3. Mixed Solution Films

The immiscibility of CuO and ZnO allows for the creation of innovative sensor designs that increase the degree of connectivity between phases. As such, CuO and MOE-based ZnO precursors were combined into one solution so as to explore the effects of annealing temperature and time on phase separation and thin film morphology. A 1:1 molar ratio of Cu:Zn atoms was held constant in these solutions and the pyrolysis was varied from 200 °C – 400 °C in 100 °C increments. Annealing was performed at 700 °C – 900 °C in 100 °C increments for times of 1, 5, and 10 hours for films pyrolyzed at 300 °C. The existence of ZnO and CuO is seen in the XRD data up to an annealing treatment of 900 °C for 1 hour. Samples annealed at 900 °C for 5 and 10 hours showed an absence of ZnO while CuO was still present. It is believed that, at these temperatures and times, ZnO either volatilizes or forms a reaction phase. SEM data points to the following scenario: At 700 °C, the ZnO and CuO exist in a coherent networked structure. As the annealing temperature is raised to 800 °C, increased phase separation and growth leads to the formation of a more porous film consisting of ZnO and CuO grains. At 900 °C, complete separation of the ZnO and CuO occurs in the form of segregated spherical grains. Optimal degrees of connectivity and thus a more effective gas sensor are assumed to exist at annealing temperatures between 700 °C – 800 °C.

7.4. Future Work

7.4.1. Heterostructures with DMF-based ZnO

As stated above, the ZnO films incorporated into the planar thin film heterostructures were fabricated using a MOE-based method. The reasoning for this was due to the wealth of previous research in fabricating ZnO using this solvent. The high boiling point of DMF presents a unique opportunity to increase film density due to its continual existence at higher drying temperatures. This may serve to increase sensor sensitivity due to the higher number of charge carriers available in the presence of a reducing gas.

7.4.2. Planar Heterostructure Electrode Configuration

The thin film heterostructures fabricated in this work were tested using non-optimized electrode geometries. This contributed to the poor rectification behavior observed in the *I-V* data. Work is underway to deposit the bottom oxide layer on silicon coated with layer of platinum. This bottom electrode combined with a meandering electrode on the top oxide layer is expected to optimize the electric field lines so as to maximize sensor response. This ideal electrode configuration may also serve to increase device sensitivity due to a more efficient transport of charge carriers across the heterostructure interface.

7.4.3. Mixed Solution Film Testing

Testing of the mixed solution films will occur using silver interdigitated electrodes on the film surface. The electrical response in ambient hydrogen will examined for various electrode finger spacings and sizes. The expectation is that an ideal degree of ZnO/CuO connectivity will be reflected in the *I*-*V* data by an enhancement in sensitivity characteristics. Optimal sensor response is expected to occur for films annealed in the 700 °C – 800 °C temperature range due to the more cohesive film morphology displayed in the SEM images.